Signal processing and machine learning for TDR-based distributed sensing

Original Citation:
Signal processing and machine learning for TDR-based distributed sensing / Scarpetta, Marco. - ELETTRONICO. - (2022). [10.60576/poliba/iris/scarpetta-marco_phd2022]

Published version
DOI:10.60576/poliba/iris/scarpetta-marco_phd2022

Publisher: Politecnico di Bari

Politecnico
di Bari

LIBERATORIA PER L'ARCHIVIAZIONE DELLA TESI DI DOTTORATO

Al Magnifico Rettore
del Politecnico di Bari

Il sottoscritto Marco Scarpetta nato ad Acquaviva delle Fonti (BA) il 07/06/1993

residente a Gioia del Colle (BA) in via Marchesana 604 e-mail marco.scarpetta@poliba.it

iscritto al 3° anno di Corso di Dottorato di Ricerca in Ingegneria Elettrica e dell'Informazione ciclo XXXV

ed essendo stato ammesso a sostenere l'esame finale con la prevista discussione della tesi dal titolo:

Signal processing and machine learning for TDR-based distributed sensing

DICHIARA

1) di essere consapevole che, ai sensi del D.P.R. n. 445 del 28.12.2000, le dichiarazioni mendaci, la falsità negli atti e l'uso di atti falsi sono puniti ai sensi del codice penale e delle Leggi speciali in materia, e che nel caso ricorressero dette ipotesi, decade fin dall'inizio e senza necessità di nessuna formalità dai benefici conseguenti al provvedimento emanato sulla base di tali dichiarazioni;
2) di essere iscritto al Corso di Dottorato di ricerca in Ingegneria Elettrica e dell'Informazione ciclo XXXV, corso attivato ai sensi del "*Regolamento dei Corsi di Dottorato di ricerca del Politecnico di Bari*", emanato con D.R. n.286 del 01.07.2013;
3) di essere pienamente a conoscenza delle disposizioni contenute nel predetto Regolamento in merito alla procedura di deposito, pubblicazione e autoarchiviazione della tesi di dottorato nell'Archivio Istituzionale ad accesso aperto alla letteratura scientifica;
4) di essere consapevole che attraverso l'autoarchiviazione delle tesi nell'Archivio Istituzionale ad accesso aperto alla letteratura scientifica del Politecnico di Bari (IRIS-POLIBA), l'Ateneo archivierà e renderà consultabile in rete (nel rispetto della Policy di Ateneo di cui al D.R. 642 del 13.11.2015) il testo completo della tesi di dottorato, fatta salva la possibilità di sottoscrizione di apposite licenze per le relative condizioni di utilizzo (di cui al sito http://www.creativecommons.it/Licenze), e fatte salve, altresì, le eventuali esigenze di "embargo", legate a strette considerazioni sulla tutelabilità e sfruttamento industriale/commerciale dei contenuti della tesi, da rappresentarsi mediante compilazione e sottoscrizione del modulo in calce (Richiesta di embargo);
5) che la tesi da depositare in IRIS-POLIBA, in formato digitale (PDF/A) sarà del tutto identica a quelle **consegnate**/inviate/da inviarsi ai componenti della commissione per l'esame finale e a qualsiasi altra copia depositata presso gli Uffici del Politecnico di Bari in forma cartacea o digitale, ovvero a quella da discutere in sede di esame finale, a quella da depositare, a cura dell'Ateneo, presso le Biblioteche Nazionali Centrali di Roma e Firenze e presso tutti gli Uffici competenti per legge al momento del deposito stesso, e che di conseguenza va esclusa qualsiasi responsabilità del Politecnico di Bari per quanto riguarda eventuali errori, imprecisioni o omissioni nei contenuti della tesi;
6) che il contenuto e l'organizzazione della tesi è opera originale realizzata dal sottoscritto e non compromette in alcun modo i diritti di terzi, ivi compresi quelli relativi alla sicurezza dei dati personali; che pertanto il Politecnico di Bari ed i suoi funzionari sono in ogni caso esenti da responsabilità di qualsivoglia natura: civile, amministrativa e penale e saranno dal sottoscritto tenuti indenni da qualsiasi richiesta o rivendicazione da parte di terzi;
7) che il contenuto della tesi non infrange in alcun modo il diritto d'Autore né gli obblighi connessi alla salvaguardia di diritti morali od economici di altri autori o di altri aventi diritto, sia per testi, immagini, foto, tabelle, o altre parti di cui la tesi è composta.

Bari, 19/12/2022

Firma Marco Scarpetta

Il sottoscritto, con l'autoarchiviazione della propria tesi di dottorato nell'Archivio Istituzionale ad accesso aperto del Politecnico di Bari (POLIBA-IRIS), pur mantenendo su di essa tutti i diritti d'autore, morali ed economici, ai sensi della normativa vigente (Legge 633/1941 e ss.mm.ii.),

CONCEDE

- al Politecnico di Bari il permesso di trasferire l'opera su qualsiasi supporto e di convertirla in qualsiasi formato al fine di una corretta conservazione nel tempo. Il Politecnico di Bari garantisce che non verrà effettuata alcuna modifica al contenuto e alla struttura dell'opera.
- al Politecnico di Bari la possibilità di riprodurre l'opera in più di una copia per fini di sicurezza, back-up e conservazione.

Bari, 19/12/2022

Firma Marco Scarpetta

POLITECNICO DI BARI

DEPARTMENT OF ELECTRICAL AND INFORMATION ENGINEERING

ELECTRICAL AND INFORMATION ENGINEERING PH.D. PROGRAM

SSD: ING-INF/07–ELECTRICAL AND ELECTRONIC MEASUREMENTS

FINAL DISSERTATION

Signal processing and machine learning for TDR-based distributed sensing

by

Marco Scarpetta

SUPERVISOR:
Prof. Nicola Giaquinto

Coordinator of Ph.D. Program:
Prof. Mario Carpentieri

COURSE NO 35, 01/11/2019 - 31/10/2022

Politecnico di Bari

Department of Electrical and Information Engineering

Electrical and Information Engineering Ph.D. Program

SSD: ING-INF/07–Electrical and Electronic Measurements

Final Dissertation

Signal processing and machine learning for TDR-based distributed sensing

by

Marco Scarpetta

Referees:

Prof. Pasquale Arpaia

Prof. Stefano Pisa

Supervisor:

Prof. Nicola Giaquinto

Coordinator of Ph.D. Program:
Prof. Mario Carpentieri

Course no 35, 01/11/2019 - 31/10/2022

Contents

Abstract

The aim of this thesis is to present innovative signal processing and machine learning approaches to improve the estimation results of time-domain reflectometry (TDR) and extend its fields of application and capabilities. Different variations of the reflectometry technique and of the relative estimation algorithms are studied. First, algorithms to realize effectively and accurately the stepped-frequency waveform reflectometry (SFWR), i.e. the reflectometric technique based on the use of sinusoidal bursts, are treated. The SFWR technique is first theoretically analyzed, highlighting the problems associated to the transient components in the reflected signals. Then, a method to minimize the effect of the transients, estimating the desired quantities with very low systematic error, is presented. The usage of deep learning for the analysis of TDR signals is then explored. In particular, a convolutional neural network is employed for the detection and characterization of multiple impedance discontinuity points in cables. Finally, a novel method for enhancing TDR detection and localization of water leaks in underground pipes is presented. In this case, TDR signals are analyzed using a novel simulation-based algorithm, which identifies a "gray-box" model of the whole electromagnetic system involved in the measurement. This model provides an approximate but much simpler representation of the system, that is nevertheless capable to reproduce the measured reflectograms with good accuracy.

List of Publications

The following publications have been co-authored during the Ph.D. program. Papers published before the beginning of the Ph.D. program and those published on proceedings of Italian National conferences are not listed here. A total of **seven** papers have been published on international journals during the Ph.D program. Paper **[12]** has been awarded with the **IEEE MeMeA 2021 Best Student Paper Award**; paper **[17]** has been awarded with the **IEEE I2MTC 2022 Student Travel Grant**.

1. L. De Palma, **M. Scarpetta**, and M. Spadavecchia, "Characterization of Heart Rate Estimation Using Piezoelectric Plethysmography in Time- and Frequency-domain," in *2020 IEEE International Symposium on Medical Measurements and Applications (MeMeA)*, Jun. 2020, pp. 1–6. DOI: `10.1109/MeMeA49120.2020.9137226`.
2. N. Giaquinto, **M. Scarpetta**, M. A. Ragolia, and P. Pappalardi, "Real-time drip infusion monitoring through a computer vision system," in *2020 IEEE International Symposium on Medical Measurements and Applications (MeMeA)*, Jun. 2020, pp. 1–5. DOI: `10.1109/MeMeA49120.2020.9137359`.
3. N. Giaquinto, **M. Scarpetta**, and M. Spadavecchia, "Algorithms for Locating and Characterizing Cable Faults via Stepped-Frequency Waveform Reflectometry," *IEEE Transactions on Instrumentation and Measurement*, vol. 69, no. 9, pp. 7271–7280, Sep. 2020. DOI: `10.1109/TIM.2020.2974110`.
4. N. Giaquinto, **M. Scarpetta**, and M. Spadavecchia, "Separation of Overlapping Reflected Signals in Stepped-Frequency Waveform Reflectometry," in *2020 IEEE International Instrumentation and Measurement Technology Conference (I2MTC)*, May 2020, pp. 1–6. DOI: `10.1109/I2MTC43012.2020.9128537`.

5. F. Adamo, F. Attivissimo, A. Di Nisio, M. A. Ragolia, and **M. Scarpetta**, "A New Processing Method to Segment Olive Trees and Detect Xylella Fastidiosa in UAVs Multispectral Images," in *2021 IEEE International Instrumentation and Measurement Technology Conference (I2MTC)*, May 2021, pp. 1–6. DOI: `10.1109/I2MTC50364.2021.9459835`.
6. N. Giaquinto, **M. Scarpetta**, M. Spadavecchia, and G. Andria, "Deep Learning-Based Computer Vision for Real-Time Intravenous Drip Infusion Monitoring," *IEEE Sensors Journal*, vol. 21, no. 13, pp. 14 148–14 154, Jul. 2021. DOI: `10.1109/JSEN.2020.3039009`.
7. M. A. Ragolia, F. Attivissimo, A. Di Nisio, A. M. L. Lanzolla, and **M. Scarpetta**, "Reducing effect of magnetic field noise on sensor position estimation in surgical EM tracking," in *2021 IEEE International Symposium on Medical Measurements and Applications (MeMeA)*, Jun. 2021, pp. 1–6. DOI: `10.1109/MeMeA52024.2021.9478723`.
8. M. A. Ragolia, F. Attivissimo, A. D. Nisio, A. M. L. Lanzolla, and **M. Scarpetta**, "A virtual platform for real-time performance analysis of electromagnetic tracking systems for surgical navigation," *ACTA IMEKO*, vol. 10, no. 4, pp. 103–110, Dec. 2021. DOI: `10.21014/acta_imeko.v10i4.1191`.
9. M. A. Ragolia, A. di Nisio, A. M. Lanzolla, G. Percoco, **M. Scarpetta**, and G. Stano, "Thermal Characterization of Electrical Resistance of 3D printed sensors," in *2021 IEEE International Instrumentation and Measurement Technology Conference (I2MTC)*, May 2021, pp. 1–6. DOI: `10.1109/I2MTC50364.2021.9459968`.
10. **M. Scarpetta**, M. Spadavecchia, F. Adamo, M. A. Ragolia, and N. Giaquinto, "Detection and Characterization of Multiple Discontinuities in Cables with Time-Domain Reflectometry and Convolutional Neural Networks," *Sensors*, vol. 21, no. 23, p. 8032, Jan. 2021. DOI: `10.3390/s21238032`.
11. **M. Scarpetta**, M. Spadavecchia, G. Andria, M. A. Ragolia, and N. Giaquinto, "Analysis of TDR Signals with Convolutional Neural Networks," in *2021 IEEE International Instrumentation and Measurement Technology Conference (I2MTC)*, May 2021, pp. 1–6. DOI: `10.1109/I2MTC50364.2021.9460009`.

12. **M. Scarpetta**, M. Spadavecchia, G. Andria, M. A. Ragolia, and N. Giaquinto, "Simultaneous Measurement of Heartbeat Intervals and Respiratory Signal using a Smartphone," in *2021 IEEE International Symposium on Medical Measurements and Applications (MeMeA)*, Jun. 2021, pp. 1–5. DOI: `10.1109/MeMeA52024.2021.9478711`.
13. L. De Palma, F. Adamo, F. Attivissimo, S. De Gioia, A. Di Nisio, A. M. L. Lanzolla, and **M. Scarpetta**, "Low-cost capacitive sensor for oil-level monitoring in aircraft," in *2022 IEEE International Instrumentation and Measurement Technology Conference (I2MTC)*, May 2022, pp. 1–4. DOI: `10.1109/I2MTC48687.2022.9806667`.
14. A. Di Nisio, N. Giaquinto, A. M. L. Lanzolla, M. A. Ragolia, **M. Scarpetta**, and S. Carrara, "Platinum Nanostructured Needle-Shaped Sensors for Ion-Detection in Biomedical Applications," *IEEE Sensors Journal*, 2022. DOI: `10.1109/JSEN.2022.3216682`.
15. E. Pittella, R. Schiavoni, G. Monti, A. Masciullo, **M. Scarpetta**, A. Cataldo, and E. Piuzzi, "Split Ring Resonator Network and Diffused Sensing Element Embedded in a Concrete Beam for Structural Health Monitoring," *Sensors*, vol. 22, no. 17, p. 6398, 2022. DOI: `10.3390/s22176398`.
16. **M. Scarpetta**, M. Spadavecchia, G. Andria, M. A. Ragolia, and N. Giaquinto, "Accurate simultaneous measurement of heartbeat and respiratory intervals using a smartphone," *Journal of Instrumentation*, vol. 17, no. 07, P07020, Jul. 2022. DOI: `10.1088/1748-0221/17/07/P07020`.
17. **M. Scarpetta**, P. Affuso, M. De Virgilio, M. Spadavecchia, G. Andria, and N. Giaquinto, "Monitoring of Seagrass Meadows Using Satellite Images and U-Net Convolutional Neural Network," in *2022 IEEE International Instrumentation and Measurement Technology Conference (I2MTC)*, May 2022, pp. 1–6. DOI: `10.1109/I2MTC48687.2022.9806535`.
18. **M. Scarpetta**, A. Cataldo, M. Spadavecchia, E. Piuzzi, A. Masciullo, and N. Giaquinto, "Accurate Detection and Localization of Water Pipe Leaks Through Model-Based TDR Inversion," *Sensors, under review*, 2022.

19. **M. Scarpetta**, M. Spadavecchia, V. I. D'Alessandro, L. De Palma, and N. Giaquinto, "A new dataset of satellite images for deep learning-based coastline measurement," in *2022 IEEE International Conference on Metrology for eXtended Reality, Artificial Intelligence, and Neural Engineering*, Oct. 2022, pp. 1–6.

List of Figures

List of Tables

List of Abbreviations

AWG arbitrary waveform generator

CNN convolutional neural network

EM electromagnetic

FDR frequency domain reflectometry

FMCW-FDR frequency-modulated continuous-wave reflectometry

FRF frequency response function

GRNN generalized regression neural network

MAPE mean absolute percentage error

MLP-NN multi-layer perceptron neural network

OLS ordinary least squares

PD-FDR phase-detection frequency domain reflectometry

R-CNN region-based convolutional neural network

ReLU rectified linear unit

RMSE root-mean-squared error

SE sensing element

SFWR stepped-frequency waveform reflectometry

SWR standing wave reflectometry

TFDR time-frequency domain reflectometry

TDR time-domain reflectometry

TL transmission line

Introduction

Reflectometry is a technique proposed in 1931 **[1]**, and used since the Forties to detect and localize defect in cables **[2]**. It is nowadays used for a number of applications in very different fields, e.g.: for measuring humidity and salinity of media and materials (like soil, concrete, etc.) **[3]–[5]**; for monitoring landslide and rock movement **[6], [7]**; for testing circuits and PCBs **[8], [9]**; for measuring the level of multi-phase liquids **[10]–[12]**; for leak detection in underground water pipes **[13], [14]**; etc. Reflectometry is also used in distributed monitoring applications. In this case, the cable is used as a sensing element in continuous measurements of physical quantities in large regions or structures. An example is the monitoring of structural elements, such as bridge steel strands **[15]** or concrete beams **[16], [17]** and bored piles **[18]** in buildings.

Different kind of signals can be used, and therefore, different kind of reflectometric methods are available. Comparisons among different methods are presented in **[19]**, in **[20]**, and in **[21]** (where the new method of impedance analysis at the cable input is suggested). The most used reflectometric methods are the following:

1. Time-domain reflectometry (TDR): it is probably the most common, and uses narrow pulses or short rise time steps;

2. Frequency domain reflectometry (FDR): it uses stepped-frequency sinusoids, and is actually a family of techniques, mainly phase-detection frequency domain reflectometry (PD-FDR), standing wave reflectometry (SWR), and frequency-modulated continuous-wave reflectometry (FMCW-FDR);

3. Time-frequency domain reflectometry: uses Gaussian chirp signals **[22]**;

4. Sequence TDR and Spread Spectrum TDR: use, respectively, baseband and passband pseudorandom signals **[23]–[25]**.

Although reflectometry is a widespread technique which has been studied and refined over years, research on this topic is still very active, with the aims of improving estimation accuracy and extending the usability of the method to new fields of application. One problem of particular focus is the TDR inversion or spatial TDR. "Spatial TDR" consists in the reconstruction of the spatial distribution of one or more parameters of the sensitive element used, based on the measured reflectograms; it is consequently a classic inverse electromagnetic problem (the direct problem is, of course, the calculation of the reflectogram given the spatial distribution of the parameters). It can be treated, in principle, with general methods of full-wave electromagnetic inversion, which are however computationally very expensive, and usually apply to problems where certain parameters are well defined.

The first fundamental characteristic of spatial TDR is theoretical and advantageous: it is an inverse problem that in principle can be satisfactorily solved by considering a simplified electromagnetic model in a single spatial dimension (equation of telegraphers). The second, however, is of a practical nature and is disadvantageous: in practical on-field applications, that is, in conditions that are not exactly controllable as those of a laboratory or a of simulation, there are many disturbing elements that are difficult or impossible to model exactly. These include worn connection cables and connectors, generators and measurement devices with behavior and characteristics that change with temperature and over time; presence of electromagnetic interference, etc. In general, extracting specific features from reflectograms recorded by a typical TDR set-up can be a relatively simple electromagnetic inversion problem when working under well-controlled conditions, and very little treatable when working on-field, for lengths of tens of meters or more.

The first significant works on spatial TDR can be considered **[26]** and **[27]**. The second one, in particular, describes in detail a well crafted numerical method of spatial TDR, applied however to simulated data only. The more recent work **[28]**, which is built upon the results of **[26]** and **[27]**, includes both a theoretical and an experimental part. The highlights of this work are the following.

1. The sensitive element examined is a classic flat-ribbon cable with three conductors, about 20 cm long, normally used to measure the average humidity of the soil in which is embedded (**Figure I.1**). This probe has carefully known electrical parameters, which are exploited for the inversion.

2. The mathematical model used "describe the physical process during the measurement in a very accurate and computable way" **[28]**. It includes, in addition to the electrical parameters of the probe, a perfectly matched TDR-device and leakage-free and uniform connection cables.

3. It is assumed that the parameters L, R, G, C of the TDR probe are independent of frequency, and that L, R are independent of the abscissa.

4. Consequently, the inversion problem is reduced to the minimization of a function whose gradient has perfectly known analytical expression.

5. The method is able to derive the capacity profile i.e., the abscissa-dependent profile of the primary parameter C, from a single reflectogram if null or known and fixed conductance is assumed in the sensing element; otherwise, it must use two reflectograms, taken from both terminations of the probe (double-sided reflection data).

These results have been exploited and developed in **[29]**, which has a quite important on-field application i.e. the measurement of water distribution in a full-scale model of the Unstrut river embankment in Germany. The TDR probe used is of the same type i.e. three-rod flat-ribbon cable. In this case, however, the conductors are covered with polyethylene insulation, specifically to make the probe usable for longer lengths. In this work there is therefore a first compromise between the accuracy of the mathematical model and the practical on-field usability: in fact, the insulation makes it more difficult to establish a relationship between the capacity and characteristics of the dielectric in which the probe is immersed, and impairs the accuracy of conductivity measurements. In this regard, the authors rightly state that "nevertheless, the advantage of lengthening

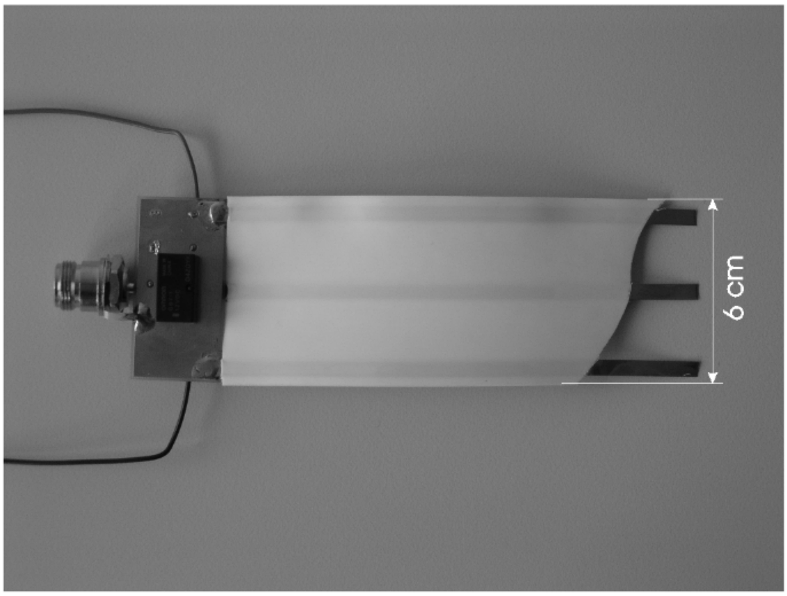

Fig. 5. Insulated flat-ribbon-cable (short section with bare conductors to visualize the geometry and the electrical connection of the cable) with a sensor switch between coaxial cable and flat-ribbon-cable.

Figure I.1: TDR probe used in **[28]** (reprinted from **[28]**).

insulated transmission lines outweighs this minor disadvantage”. In line with **[28]** and previous works, a series of simplifying assumptions are introduced:

1. The electrical characteristics of the sensing element are accurately known (“In order to predict the time domain response of the cable, the electromagnetic transmission line properties have to be measured in laboratory experiments [...]”).

2. Parameters L and R do not vary with the abscissa: “Both L and R are parameters which are assumed to be constant along the probe”.

3. The variation with frequency of R and L is considered negligible: “the influence of the resistance R [at different frequencies] can be neglected”; “no significant influence of the inductance increase at low frequencies is to be expected”.

4. Also C and G, which are considered as variable with the abscissa, are independent of frequency: “At low conductivities [...] the dispersion of C and G can be neglected for the dominant frequency range of the TDR signals used

for reconstruction (f > 10 MHz)".

5. Other considerations are made about the non-TEM modes and the electromagnetic radiation of the probe, concluding that they, under appropriate experimental conditions, can be considered negligible: "wave modes other than the transversal-electromagnetic (TEM) mode and frequency dependence of transmission line properties [due to radiation] may be neglected".

The used flat ribbon cable is studied very thoroughly both with experiments in the laboratory and with full-wave simulations, to support the assumptions made. Since it is considered that the assumption of constant G along the probe is not adequate, the profiles of both C and G are reconstructed, which requires a double reflectometry, from both the ends of the probe, as shown in **Figure I.2**. It is clear that this need greatly limits the possibility of using very long and deeply buried probes. The authors assess the performance of the method with numerical simulations, the results of which are reported in **Figure I.3**. Although quite good and suitable for the purpose of the authors, two aspects must be highlighted. First, the reflectograms are reproduced quite well by the inversion operation, but *only voltage values in the time of flight of the signal are considered*. Multiple reflections, observed in successive instants of time, are not considered. To take this into account, many simplifying hypotheses should be released, and it would be very difficult, if not impossible, to have an analytical expression of the gradient of the objective function in the optimization. Secondly, although an exact analytical approach is applied to a numerical simulation, the reconstructed profile, while satisfactory for practical purposes, cannot be considered very accurate, which shows how numerically difficult the problem of inversion is, even in relatively idealized cases.

There are many other contributions to spatial TDR, too many to be discussed in detail here, but the works above have the merit of illustrating the problem, the approximations and assumptions usually involved, and typical achieved solutions. Here we want to underline that it is possibile to address the general TDR inversion problem, despite its ill-posedness, also using a single reflectogram. For example, in **[30]**, the inversion problem is reduced to a parametric identification problem,

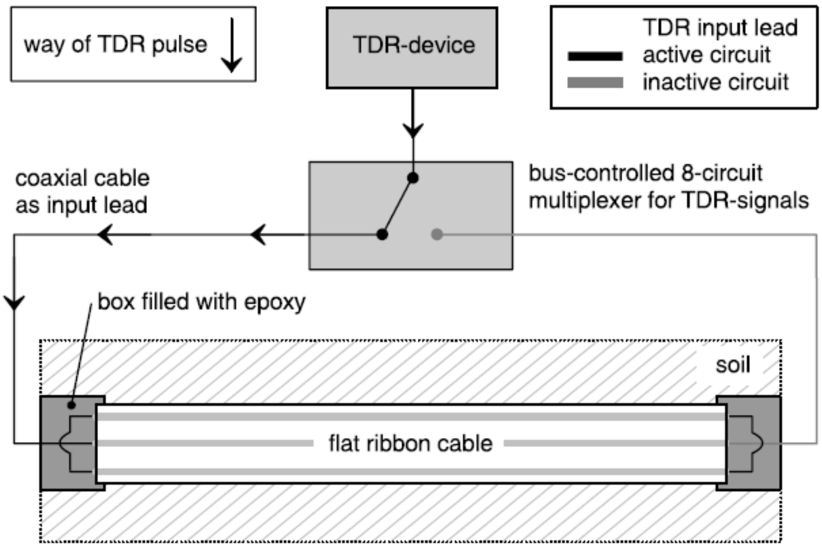

Figure I.2: TDR setup used in **[29]** (reprinted from **[29]**).

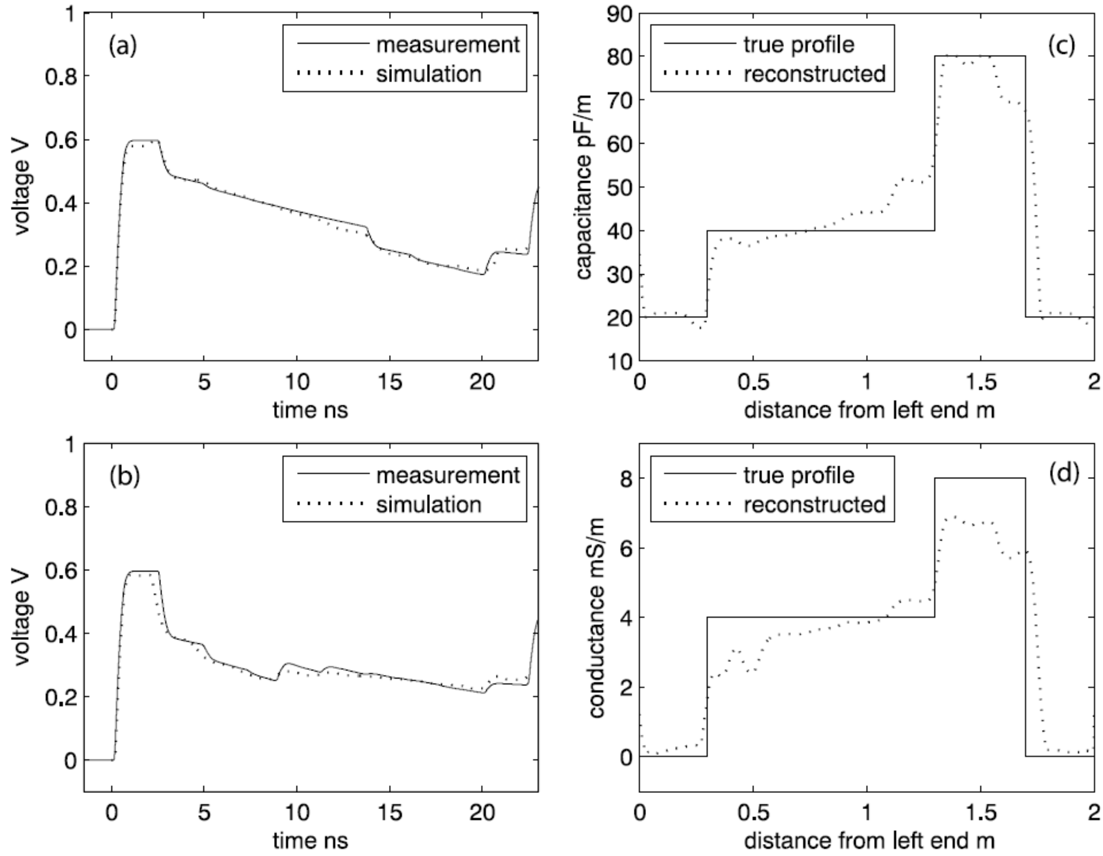

Figure I.3: Results obtained in **[29]** (reprinted from **[29]**).

introducing a four-parameter functional form for the profiles to be estimated. This simplification allows to perform the inversion using a single reflectogram, at the price of limiting the class of identifiable profiles. In **Figure I.4**, an example of reflectograms measured and reconstructed using this technique is reported. However, the technique based on fitting two reflectograms from both sides of the sensing element is far from obsolete and is used in recent works such as **[31], [32]**.

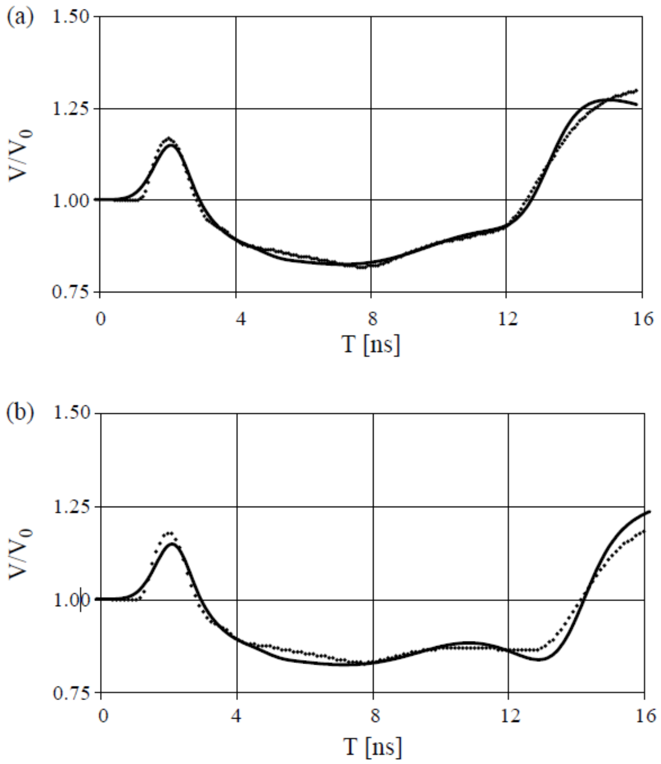

Figure I.4: Measured reflectograms (solid line) and reconstructed reflectograms (dotted line) obtained in **[30]** (reprinted from **[30]**).

An important aspect is that, many important applications of TDR require, as has been said, on-field measurements in more difficult conditions than those normally taken into account, namely with very long sensitive elements, robust and not perfectly calibrated instrumentation, and in the presence of many non-idealities and external factors that greatly affect the measures. These are actually experimental situations that are impossible to electromagnetically model in accurate way. A reflectogram such as the one in **Figure I.5**, obtained during a leakage research campaign using TDR, can only be inverted in an extremely approximate way with the techniques available in the literature, simply because of the lack of sufficient information on the electromagnetic situation. As shown in the following of this thesis, however, an almost perfect inversion is possible, i.e. reproducing the measured reflectogram with great accuracy, while having very little quantitative information on the experimental set-up, and using a single measurement. This does not lead to a complete reconstruction of the profile of capacity, conductance, or other parameters, because the method must necessarily use a very approximate model, which we can define “gray-box”; the inversion is however sufficient, with reference to the specific practical application, to locate and quantify with considerable accuracy the presence of water along the sensitive element, even when it is not “visible to the naked eye” in the reflectogram.

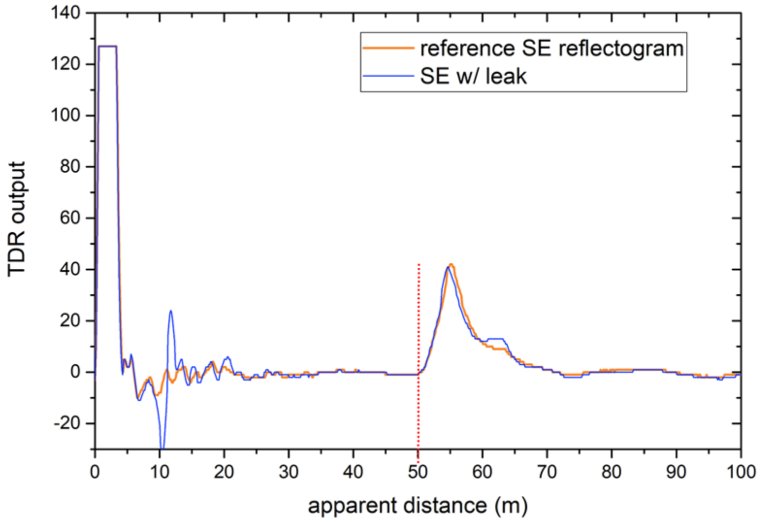

Figure I.5: Reflectogram obtained during a leakage research campaign.

Purpose of this thesis

This aim of this thesis is to present signal processing and machine learning approaches to improve the estimation results of TDR and extend the current capabilities of the reflectometry technique. **Chapter 1** presents new algorithms to realize effectively and accurately the stepped-frequency waveform reflectometry (SFWR), i.e. the reflectometric technique based on the use of sinusoidal bursts **[33], [34]**. In this Chapter, the presented algorithms are characterized for the case of monitoring the health status of connection cables, but the technique can be used in all the classical reflectometry applications. The SFWR technique is first theoretically analyzed, highlighting the problems associated to the transient components in the reflected signals. Then, a method to minimize the effect of the transients, estimating the frequency response function (FRF) of interest with very low systematic error is presented. Using the information provided by FRF, faults in cables are located and characterized accurately. Finally, a technique for separating overlapping reflected signals in SFWR is presented and integrated with the fault characterization procedure. The Chapter reports comprehensive simulated and experimental results proving the effectiveness of the method.

In **Chapter 2**, the usage of deep learning for the analysis of TDR is explored. In particular, a convolutional neural network is employed for the detection and characterization of multiple impedance discontinuity points in cables **[35], [36]**. The developed neural network has been trained using a great number of simulated signals, obtained with a transmission line simulator. Then, it is tested on both simulated and measured signals. It must be noted that, the preparation of a proper dataset for training is often the most important and critical aspect when working with neural networks. Since this preparation is a very burdensome and time-consuming task, automatic or semi-automatic procedures for dataset creation from actual data have been often employed **[37]–[40]**. In our case, a synthetic dataset composed of simulated signals proved very effective: it is easily and automatically produced and works very well with actual measured data.

A different application is analyzed in **Chapter 3**, where a novel method for enhancing TDR detection and localization of water leaks in underground pipes is presented. To this purpose, simple bi-wire sensing elements are placed near the pipe, and used to acquire TDR signals. Signals are then analyzed using a novel simulation-based algorithm, which identifies a “gray-box” model of the whole electromagnetic system composed by the TDR appliance, the mismatched connections, the wires, the surrounding soil and rocks, etc. The key idea is to give up the goal of modeling accurately the overly too complex electromagnetic system, reverting to a simpler and computationally tractable, approximate representation, that is nevertheless capable to reproduce the measured reflectograms with good accuracy. The final result is a quite accurate localization of water leaks, even with reflectograms of problematic or impossible interpretation, and even if a number of electromagnetic effects, typical of on-field measurements, remains unmodeled and/or not accurately quantified.

Chapter 1

Algorithms for locating and characterizing cable faults via stepped-frequency waveform reflectometry[1]

1.1 Introduction

Stepped-frequency waveform reflectometry (SFWR) has been introduced in **[41]**. The technique uses sinusoidal bursts, and therefore combines some advantages inherent of FDR and TDR. First, generating sinusoidal bursts (gated sinusoids) is simpler: it does not require a fast rise-time pulse generator like TDR, nor a swept sinusoidal generator like FMCW-FDR. Second, the analysis of sinusoidal bursts does not require special hardware with directional couplers to separate the reflected and the transmitted signal, like in PD-FDR, since transmitted and reflected sinusoidal bursts are already separated in the time domain. Third, a number of sinusoidal bursts can be either embedded in a single signal to obtain the complete measurement with a single acquisition, or, if more convenient, they can be generated and used once at a time with a cheap sinusoidal generator; in this case, the measurement is carried out with multiple acquisition, without any

---

[1] This Chapter is based on the papers **[33]**, **[34]**

loss of accuracy. Summing up, using sinusoidal bursts makes possible accurate frequency-domain measurements with cheap and portable hardware. Furthermore, SFWR is compared with TDR in **[41]**, using practical experiments. Results show that an accurate assessment of faults characteristics (location, reflection coefficient) is more difficult to obtain with customary impulse-based or step-based TDR, since it is heavily influenced by the distance of the fault. It is true, on the other hand, that "traditional" TDR can be improved with dedicated signal processing and system identification techniques, like those proposed in **[42]**.

In **[41]**, the effectiveness of SFWR is demonstrated using a specific signal processing technique, and under specific assumptions. As regards signal processing, the work relies on the Rihaczek time–frequency distribution, a non-parametric method that is able to obtain good results, but does not exploit additional information available on the signal. In particular, transient components in the reflected signal affect a non-parametric time-frequency analysis, while they can be modeled and compensated with a parametric approach. As regards the underlying assumptions, all measurements in **[41]** are obtained assuming a quadratic model of the propagation function, and a frequency-independent reflection coefficient. Such assumptions are quite strict, and it is obviously desirable to release them. Moreover, although the experimental results presented in **[41]** are clearly satisfactory, only the order of magnitude of the measurement errors is evaluated, by comparison with reference values (e.g. the propagation function measured with an open-ended cable). It will be shown that the performance of the estimation algorithms can be evaluated accurately using proper simulations.

The aim of the first part of this chapter is to present:

- a comprehensive theoretical framework of the SFWR technique, with a clear systematization of the basis of the method, built on a more general propagation model;
- signal estimation algorithms designed specifically to work with sinusoidal bursts reflected by a transmission line, taking into account transient components;
- measurement techniques free from assumptions about the propagation func-

tion and the reflection coefficient;

- the optimization of the above techniques for the special case of reflection coefficient independent on the frequency, examined in **[41]**;
- simulation results, using a MATLAB simulator already developed and validated by the authors **[43]**, in order to evaluate accurately the errors due to the algorithms;
- experimental results, obtained from measurements on real cables, to prove the effective applicability of proposed algorithms in real-life situations.

Therefore, estimation algorithms are introduced, different from those presented in **[41]**, and able to better extract relevant information from SFWR signals. Furthermore, the technique has been extended to work in more general situations, so that limiting hypothesis about the propagation function of the line and the reflection coefficient are no more necessary.

Even if reflectometry has many different applications, as pointed out above, the focus is here on the location and classification of faults in cables. This is to keep the focus on a specific problem, and for easy comparison with **[41]**. Of course, monitoring the health status of cables is also very important per se, to guarantee safe and correct operation of many systems and plants, especially those where a failure can cause disastrous accidents, like nuclear power plants and aircrafts.

Other measuring and diagnosis applications of the SFWR technique are, e.g. measurement of humidity of media and materials **[5], [44], [45]**, measurement of the level of a liquid **[46]**, fuel quality monitoring **[47]**, detection of leaks in pipelines **[14]**, monitoring building structures **[48]**. In such applications multiple reflective interfaces are often present, which may produce overlapping reflected signals. Overlapping can also occur between the transmitted burst and the burst reflected at the first discontinuity if it is located near the point where the signal is transmitted. In **Section 1.7**, an algorithm is presented that uses an iterative procedure to find the position of overlapping reflected sinusoidal bursts and to estimate their parameters.

1.2 Preliminary concepts

A preliminary detailed description of the basic concepts of SFWR and TDR in general is presented in this Section.

1.2.1 Signal reflection and associated FRF in a cable

A cable is a transmission line (TL) which, unless perfectly homogeneous and terminated on its characteristic impedance, has one or more impedance discontinuities, where reflections occurs. We can consider the simple situation in **Figure 1.1**, where a TL with characteristic impedance Z_0 is terminated on the load Z_L.

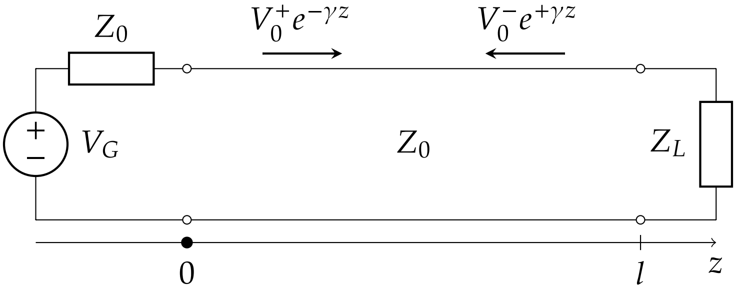

Figure 1.1: Model of a cable as a transmission line terminated on a generic load.

The propagation function of the line is:

$$\gamma(\omega) = \sqrt{[R(\omega) + j\omega L(\omega)] \cdot [G(\omega) + j\omega C(\omega)]} = \alpha(\omega) + j\beta(\omega) \tag{1.1}$$

where $R(\omega)$, $L(\omega)$, $G(\omega)$, $C(\omega)$ are respectively resistance, inductance, conductance, capacitance per unit length (primary parameters), and $\alpha(\omega)$ and $\beta(\omega)$ are the attenuation and propagation functions (secondary parameters). In common idealized models, like the low-loss TL with frequency-independent primary parameters, $\alpha(\omega)$ is a constant, and $\beta(\omega)$ is a linear function. In real-world case, $\gamma(\omega)$ is a more general function of the frequency.

The phasor of a sinusoidal signal in the TL is:

$$V(z) = V^+(z) + V^-(z) = V_0^+ e^{-\gamma z} + V_0^- e^{\gamma z} \tag{1.2}$$

where $V^+(z)$ and $V^-(z)$ are, respectively, the phasors of the transmitted and of the reflected signal. The ratio of the phasors at the beginning of the cable ($z = 0$) is the reflection coefficient at $z = 0$, which can be seen as a (complex) FRF:

$$\bar{H}(\omega) = \frac{V^-(0)}{V^+(0)} = \frac{V_0^-}{V_0^+} = \bar{\Gamma}(\omega)e^{-\gamma(\omega)2l} \tag{1.3}$$

where $\bar{\Gamma}(\omega) = (Z_L - Z_0)/(Z_L + Z_0)$ is the complex reflection coefficient at the termination of the cable, with magnitude $\Gamma(\omega)$ and phase $\varphi_\Gamma(\omega)$, l is the length of the TL. If the generator is not exactly matched with the TL, (**1.3**) is perfectly valid, but $\bar{\Gamma}(\omega)$ includes a term due to the mismatch, as demonstrated in **[42]**.

Amplitude and phase of $\bar{H}(\omega)$ are:

$$H(\omega) = \Gamma(\omega)e^{-\alpha(\omega)2l} \tag{1.4}$$

$$\varphi_H(\omega) = -\beta(\omega)2l + \varphi_\Gamma(\omega) \tag{1.5}$$

It is useful to write the phase response also in terms of the propagation time $\tau_p(\omega) = 2l/v_p(\omega)$, where $v_p(\omega) = \omega/\beta(\omega)$ is the propagation velocity:

$$\varphi_H(\omega) = -\omega\tau_p(\omega) + \varphi_\Gamma(\omega) \tag{1.6}$$

The SFWR technique is primarily designed to measure $\bar{H}(\omega)$ in a set of chosen frequencies ω_i, $i = 0, \ldots, N-1$. From $\bar{H}(\omega)$, using other available information, quantities of interest can be obtained, mainly the position l at which the reflection occurs, the propagation functions $\alpha(\omega)$, $\beta(\omega)$, and the reflection coefficient $\bar{\Gamma}(\omega)$.

1.2.2 SFWR transmitted signal, bursts duration and spacing

The SFWR transmitted signal is a sequence of sinusoidal bursts of increasing, linearly spaced frequencies $\omega_i = \omega_0 + i \cdot \Delta\omega$, $i = 0, \ldots, N-1$. The overall signal is $x_{tr}(t) = \sum_{i=0}^{N-1} x_{tr,i}(t)$, with

$$x_{tr,i}(t) = d_{tr,i}\sin(\omega_i(t - iT) + \varphi_{tr,i})\,\mathrm{rect}\left(\frac{t - iT - \frac{\tau}{2}}{\tau}\right) \tag{1.7}$$

where the amplitudes $d_{tr,i}$ are nominally equal, the phases $\varphi_{tr,i}$ are nominally zero, and rect(t) is the rectangular unit pulse. An example of such a signal is depicted in **Figure 1.2**.

The critical parameters to choose are:

- the burst duration, τ;
- the time interval between consecutive bursts, T;
- the linearly spaced frequencies ω_i.

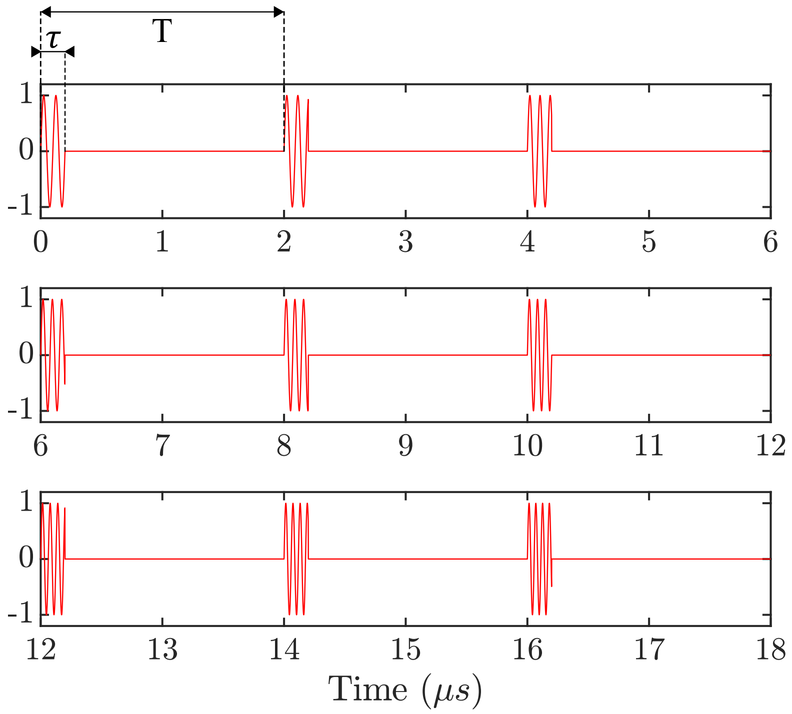

Figure 1.2: Example of SFWR transmitted signal.

Discussing the choice of the frequencies needs some specific results, that will be derived in the next Section. As regards τ and T, they must be chosen on the basis of an approximate knowledge of the propagation velocity v_p in the cable, and of the diagnostic range, i.e. the minimum and the maximum positions $[l_{min}, l_{max}]$ at which the reflection can occur. Indeed, the reflection of each burst must satisfy two constraints: *(i)* it begins after the end of the transmitted burst; *(ii)* it vanishes before the beginning of the subsequent transmitted burst.

The first constraint gives the condition:

$$\tau \leq \tau_{max} = \frac{2l_{min}}{v_p} \tag{1.8}$$

and the second constraint gives the condition:

$$T \geq T_{min} = \frac{2l_{max}}{v_p} + \tau \tag{1.9}$$

As an example of design, in the tests reported in **Section 1.5**, we have $v_p \approx 2 \times 10^8\,\mathrm{m/s}$, $[l_{min}, l_{max}] \approx [20\,\mathrm{m}, 180\,\mathrm{m}]$, and therefore, $\tau_{max} = 200\,\mathrm{ns}$. Assuming $\tau = \tau_{max}$, condition (**1.9**) gives $T_{min} = 2\,\mu\mathrm{s}$.

1.3 Measuring frequency response using SFWR

As stated above, we use time-domain and parametric estimation techniques to analyze the SFWR signal. The advantage is that they can be easily tailored to the actual FRF to be measured. The response of $\bar{H}(\omega)$ to a finite-duration sinusoidal burst, indeed, contains transient components which makes it quite different from the nearly ideal signal depicted in **Figure 1.3**.

1.3.1 Preliminary operations on the SFWR signal

First of all, the SFWR signal must be split into N segments of duration T, so that the i-th segment contains a single pair of transmitted and reflected bursts at frequency ω_i. From each segment, two sample sequences, respectively containing the transmitted and the reflected burst only, are easily generated, using the knowledge of the parameter τ (and assuming that the requirements in **Section 1.2.2** are met). The obtained sequences, denoted with x_n and y_n, are the input and the output of $\bar{H}(\omega)$: an example is shown in **Figure 1.3**. Both sequences are conventionally sampled at instants $0, T_s, 2T_s, \ldots, (N_s - 1)T_s$, where T_s is the sampling interval.

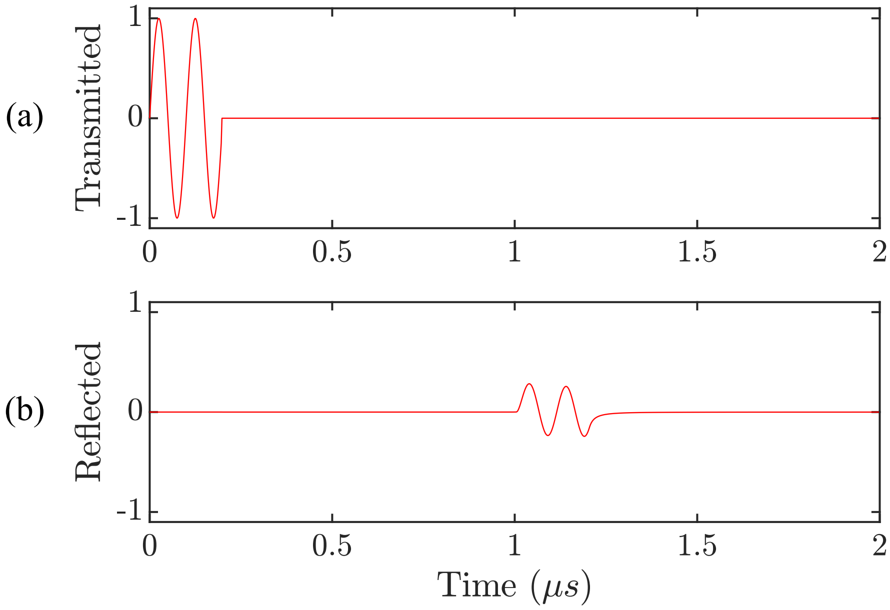

Figure 1.3: Example of signals x_n and y_n containing, respectively, the transmitted (a) and the reflected (b) burst extracted by a single segment of duration T.

1.3.2 Raw estimation of the time delay τ_d between x_n and y_n

The time delay between x_n and y_n is, by definition:

$$\tau_d(\omega_i) = -\frac{\varphi_H(\omega_i)}{\omega_i} \tag{1.10}$$

It is important to note that, in general, $\tau_d = \tau_p(\omega_i) - \varphi_\Gamma(\omega_i)/\omega_i \neq \tau_p$. A raw estimate of τ_d is easily obtained by computing the cross-correlation $r_n = \mathrm{xcorr}(y_n, x_n)$: if m is the integer lag maximizing the cross-correlation, the estimate is:

$$\tau_{d,raw}(\omega_i) = m \cdot T_s \tag{1.11}$$

1.3.3 FRF estimation via modified sinusoidal fitting

Outline of the method

The general methodology to estimate $H(\omega_i)$ and $\varphi_H(\omega_i)$ is the following, and relies on ordinary least squares (OLS) fitting.

- Compute $\tau_{d,raw} = m \cdot T_s$.
- Compute the sequence $z_n = y_{n-m}$, i.e., y_n anticipated of the time $\tau_{d,raw}$

(**Figure 1.4**).

- Determine the estimated amplitude and phase $\hat{d}_{tr,i}$, $\hat{\varphi}_{tr,i}$ of the input sequence x_n by OLS fitting.
- Determine the estimated amplitude and phase $\hat{d}_{re,i}$, $\hat{\varphi}'_{re,i}$ of the anticipated output sequence z_n by OLS fitting.
- Compute the estimated phase of the sequence y_n, given by $\hat{\varphi}_{re,i} = \hat{\varphi}'_{re,i} - \omega_i \tau_{d,raw}$
- Compute the estimated FRF amplitude and phase, $\hat{H}(\omega_i) = \hat{d}_{re,i}/\hat{d}_{tr,i}$, $\hat{\varphi}_H(\omega_i) = \hat{\varphi}_{re,i} - \hat{\varphi}_{tr,i}$

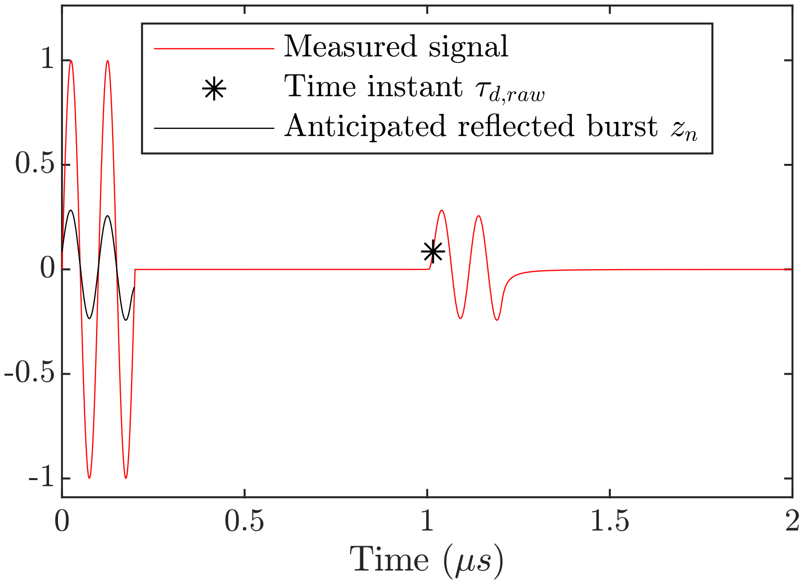

Figure 1.4: Illustration of the operation of anticipating the reflected burst of the time $\tau_{d,raw}$, obtaining the signal z_n.

The preliminary shifting of y_n of the quantity $\tau_{d,raw}$ assures that the estimated $\hat{\varphi}_{re,i}$ is not "wrapped" in the interval $[0; 2\pi[$. As a consequence, it is possible to obtain from $\hat{\varphi_H}(\omega_i)$ a correct refined estimation of the time delay using (**1.10**), i.e. $\hat{\tau}_d = -\hat{\varphi}_H(\omega_i)/\omega_i$.

To determine $\hat{d}_{tr,i}$, $\hat{\varphi}_{tr,i}$ it is sufficient a standard OLS *sinusoidal* fitting on the sequence x_n in the interval $[0; \tau[$. A sinusoidal fitting is also possible on the sequence z_n, but the results would be affected by model errors. **Figure 1.3** (b) and

Figure 1.4 (reflected burst) shows quite clearly that the sinusoidal model for the reflected burst is not very good and a modified fitting is desirable.

Modified sinusoidal fitting on z_n

Since in real-world TLs $\bar{H}(\omega)$ is almost always low-pass, we must examine the response of a low-pass filter to the finite-duration sinusoidal burst (**1.7**), anticipated of the time iT. To gain some insight in the problem, we consider the elementary first-order lowpass filter

$$\bar{H}_{LP}(j\omega) = \frac{1}{1 + j\omega\tau_c} \tag{1.12}$$

so that the response has a tractable analytic expression. This first-order filter is a simplification of the FRF of real cables and its time-domain response to sinusoidal bursts doesn't contain a delay term (like sequence z_n defined above). With the symbols $H_{LP} = |\bar{H}_{LP}(j\omega_i)|$ and $\varphi_{LP} = \angle\bar{H}_{LP}(j\omega_i)$, the response $z(t)$ to the sinusoidal burst $d_{tr,i}\sin(\omega_i t + \varphi_{tr,i})\,\mathrm{rect}\left((t - \frac{\tau}{2})/\tau\right)$ is the sum of three terms:

$$\begin{aligned} z(t) =& H_{LP} d_{tr,i} \sin(\omega_i t + \varphi_{tr,i} + \varphi_{LP})\,\mathrm{rect}\left(\frac{t - \tau/2}{\tau}\right) \\ &+ \mathrm{e}^{-t/\tau_c}\,\frac{\omega_i\omega_c}{\omega_i^2 + \omega_c^2} u(t) \\ &+ \mathrm{e}^{-\omega_c(t-\tau)}\,H_{LP} d_{tr,i} \sin(\omega_i \tau + \varphi_{tr,i} + \varphi_{LP}) u(t - \tau) \end{aligned} \tag{1.13}$$

where rect($\cdot$) is the standard rectangular function and $u(t)$ is the Heaviside step function. The first-order filter response (**1.13**) has been computed in the Laplace s-domain as:

$$z(t) = L^{-1}\left\{H_{LP}(s) \cdot L\left\{x_{tr,i}(t + iT)\right\}\right\}$$

The three terms in (**1.13**) are, respectively:

- the steady-state response of (**1.12**) to $d_{tr,i}\sin(\omega_i t + \varphi_{tr,i})$, windowed in the interval $[0;\tau[$;
- a decreasing exponential term, starting at $t = 0$;
- a decreasing exponential term, starting at $t = \tau$.

The first term is the one of interest, while the second and the third are transients that jeopardize the estimation if a simple sinusoidal fitting on the whole response is used. **Figure 1.5** shows examples of the response (**1.13**) for different values of the ratio τ_c/τ. Both the first sinusoidal term and the total response are plotted.

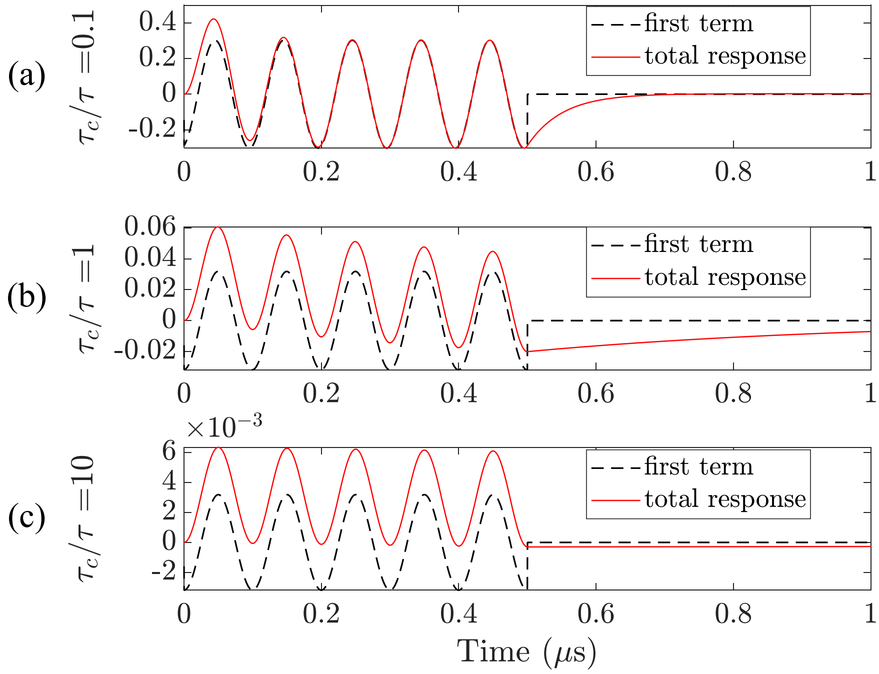

Figure 1.5: Examples of response to a sinusoidal burst of a first-order lowpass filter.

Formula (**1.13**) and **Figure 1.5** show clearly that, in order to estimate the parameters of interest H_{LP}, φ_{LP} without knowing the value of τ_c/τ, it is necessary a modified procedure, independent on the ratio τ_c/τ. This goal is achieved with two devices:

a) consider *only the second half* of the interval $[0, \tau[$, so that a possible initial spike caused by a "fast" exponential term is discarded (first case $\tau_c/\tau \ll 1$ in **Figure 1.5**);

b) fit a sinusoid *with a constant term and a linear trend*, in order to model, even if with some approximation, the possible presence of a "slow" exponential term (second and third case in **Figure 1.5**).

These two devices can be, and are both used in the estimation procedure, independently on the (unknown) τ_c/τ ratio, in order to minimize errors due to the exponential term. Device a) minimizes the problem of the initial overshoot when

$\tau_c << \tau$, and does not harm meaningfully the estimate when $\tau_c \simeq \tau$ or $\tau_c > \tau$; device b) is effective when $\tau_c \simeq \tau$ or $\tau_c > \tau$, and does not harm the estimate when $\tau_c << \tau$.

The model to fit is therefore:

$$z(t) = c + mt + d_{tr,i} \sin(\omega_i t + \varphi'_{tr,i}) \tag{1.14}$$

where the estimated terms $\hat{c}$, $\hat{m}$ are discarded, while $\hat{d}_{tr,i}$ and $\hat{\varphi}'_{tr,i}$ are used to estimate the FRF.

The performance of the approximate model (**1.14**) have been evaluated for different values of τ_c/τ, obtained by varying τ_c while keeping τ constant. The estimation has been performed on noiseless signals, since the aim is quantifying only model errors. Results are summarized in **Table 1.1** that reports, for each case, the relative magnitude estimation error $e_r(d_{tr,i}) = (\hat{d}_{tr,i} - d_{tr,i})/d_{tr,i}$, and the absolute phase estimation error $e(\varphi'_{tr,i}) = \hat{\varphi}'_{tr,i} - \varphi'_{tr,i}$. Model errors are very small, and in most practical applications will be negligible with respect to those introduced e.g. by noise.

Table 1.1: Magnitude and phase estimation errors

τ_c/τ	$e_r(d_{tr,i})$	$e_r(\varphi'_{tr,i})$ (deg)
0.01	-7.43×10^{-11}	-2.10×10^{-8}
0.1	-8.31×10^{-6}	0.0107
1	-4.19×10^{-6}	0.0598
10	-6.47×10^{-9}	8.42×10^{-4}
100	8.15×10^{-11}	8.62×10^{-6}

Model (**1.14**) has been derived and evaluated for the simple filter (**1.12**), but its effectiveness is furtherly demonstrated by other computer simulations on realistic cables and filters, reported in **Section 1.5**. In this case, the fitting has been applied to the signal in the interval $[0.5\tau; 0.95\tau]$ (specified in terms of time instants for the sequence z_n). The signal in $[0.95\tau; \tau]$ is discarded to avoid possible problems due to the imperfect estimation of $\tau_{d,raw}(\omega_i)$ which could lead to the inclusion, in the fitting interval, of regions where the burst has ended.

Since the fitting uses only the second half of the signal, it is recommended that the burst at the minimum frequency ω_0 has at least two periods, so that one period is used to reconstruct the signal amplitude and phase. A criterion for the choice of this frequency follows:

$$\omega_0 \geq \frac{4\pi}{\tau} \iff f_0 \geq \frac{2}{\tau} \tag{1.15}$$

For example, if $\tau = 200\,\mathrm{ns}$, the requirement is $f_0 \geq 10\,\mathrm{MHz}$.

1.4 Fault location and characterization from FRF

After the estimation of $H(\omega_i)$ and $\varphi_H(\omega_i)$, it is possible to perform essentially two kind of measurements:

1. the preliminary characterization of a reference cable, of known length and with known termination;
2. the fault location and characterization on a cable under test, of the same kind of the characterized reference cable.

Fault location and characterization is, in general, more precise if some information is known about the fault. We examine the case of a generic fault, for which no specific prior information is available, and that (examined also in **[41]**) of a fault with reflection coefficient constant in the frequencies ω_i of interest ($\bar{\Gamma}(\omega_i) = \bar{\Gamma}$).

In the following, the fault location l is estimated taking always into account that the propagation time $\tau_p(\omega)$ depends on the frequency. However, the estimated $\bar{H}(\omega_i)$ can be used also to identify an approximate model with a frequency-independent delay, like that in **[42]** (where $\bar{H}$ is approximated by a rational transfer function cascaded with a delay) or that in **[46]** (where simple criteria for cost-effective monitoring via TDR are compared).

1.4.1 Characterization of a reference cable

In this case, the cable length l and the reflection at the cable termination, $\bar{\Gamma}(\omega)$, are supposed to be known, and the quantity of interest is the propagation function $\Gamma(\omega) = \alpha(\omega) + j\beta(\omega)$. Relations (**1.4**) and (**1.5**) solves the problem immediately. In the common case of open-ended reference cable ($\bar{\Gamma} = 1$) we have:

$$\hat{\alpha}(\omega_i) = -\frac{\ln \hat{H}(\omega_i)}{2l} \tag{1.16}$$

$$\hat{\beta}(\omega_i) = -\frac{\hat{\varphi}_H(\omega_i)}{2l} \tag{1.17}$$

1.4.2 Location and characterization of a generic fault

In this case, $\Gamma(\omega)$ is known from a previous characterization of the cable, and the quantities of interest are the fault location l, and the reflection coefficient $\bar{\Gamma}(\omega)$ at the frequencies ω_i. Equations (**1.4**) and (**1.5**), written for the N frequencies ω_i, are a system of $2N$ equations with the $2N + 1$ unknowns l, $\Gamma(\omega_i)$, $\varphi_\Gamma(\omega_i)$. Therefore, a unique solution can be obtained only with further information, e.g. a constraint on the values of $\bar{\Gamma}(\omega_i)$. Such a case is examined in the next subsection.

With no further information, it is only possible, under the reasonable assumption of bounded $\varphi_\Gamma(\omega)$, to measure:

- l, with a bounded systematic error,
- $\Gamma(\omega_i)$, with a systematic error determined by that on l.

The measurement of l is based on the approximation $\tau_p \approx \tau_d$, i.e.:

$$\varphi_H(\omega) = -\omega\tau_d(\omega) = -\omega\tau_p(\omega) + \varphi_\Gamma(\omega) \approx -\omega\tau_p(\omega) \tag{1.18}$$

The estimation of l is, consequently, from (**1.5**):

$$\hat{l} = -\frac{\hat{\varphi}_H(\omega)}{2\hat{\beta}(\omega)} \tag{1.19}$$

The approximation $\tau_p \approx \tau_d$ introduces a systematic error, given by, in relative terms:

$$e_r = \frac{\hat{l} - l}{l} = \frac{\tau_d - \tau_p}{\tau_p} = -\frac{\varphi_\Gamma(\omega)}{\omega_i \tau_p(\omega)} = -\varphi_\Gamma(\omega)\frac{v_p(\omega)}{2l\omega} \tag{1.20}$$

Assuming $|\varphi_\Gamma(\omega)| \leq \varphi_{\Gamma,max}$ and $v_p(\omega_i) \leq v_{p,max}$, a bounded systematic error $|e_r| \leq U_r$ is achieved, under the condition

$$\omega \geq \varphi_{\Gamma,max}\frac{v_{p,max}}{2l \cdot U_r} \tag{1.21}$$

From this inequality, a criterion to choose the maximum frequency $\omega_{max} = \omega_{N-1}$ arises. Actually, equation (**1.21**) only suggests that at least one frequency must satisfy the bound, but, in practice, there is no advantage if more frequencies do, since l is computed using the maximum frequency only.

For example, if $U_r = 1\%$, $l = 180\,\mathrm{m}$, $\max|\varphi_\Gamma(\omega)| = 2\pi$, and $v_p \approx 2 \times 10^8\,\mathrm{m/s}$, the highest frequency should be at least $f_{N-1} = \omega_{N-1}/2\pi \approx 55\,\mathrm{MHz}$. With respect to the method for estimating l used in **[41]** (time-range domain transform), (**1.19**) does not require many measurements at different frequencies, but only one measurement at the highest possible frequency. Both methods assume $\tau_d \approx \tau_p$, and are therefore prone to the same systematic error.

As regards the estimation of the reflection coefficient, relation (**1.4**) gives:

$$\hat{\Gamma}(\omega_i) = \hat{H}(\omega_i)\,\mathrm{e}^{2\hat{\alpha}(\omega_i)\hat{l}} \tag{1.22}$$

Phase $\varphi_\Gamma(\omega_i)$ cannot be estimated using (**1.5**), because the approximation $\tau_p(\omega_{N-1}) \approx \tau_d(\omega_{N-1})$ implies, using (**1.5**), $\varphi_\Gamma(\omega_{N-1}) = 0$, which is justified only in (**1.18**).

1.4.3 Location and characterization of a fault with reflection coefficient independent on the frequency

In this case, since $\bar{\Gamma}$ is independent on the frequency, all the information given by $\bar{H}(\omega)$ is easily exploited, by solving the OLS problem:

$$\begin{bmatrix} \ln \hat{H}(\omega_0) \\ \ln \hat{H}(\omega_1) \\ \vdots \\ \ln \hat{H}(\omega_{N-1}) \\ \hat{\varphi}_H(\omega_0) \\ \hat{\varphi}_H(\omega_1) \\ \vdots \\ \hat{\varphi}_H(\omega_{N-1}) \end{bmatrix} = \begin{bmatrix} 1 & 0 & -2\hat{\alpha}(\omega_0) \\ 1 & 0 & -2\hat{\alpha}(\omega_1) \\ \vdots & \vdots & \vdots \\ 1 & 0 & -2\hat{\alpha}(\omega_{N-1}) \\ 0 & 1 & -2\hat{\beta}(\omega_0) \\ 0 & 1 & -2\hat{\beta}(\omega_1) \\ \vdots & \vdots & \vdots \\ 0 & 1 & -2\hat{\beta}(\omega_{N-1}) \end{bmatrix} \cdot \begin{bmatrix} \ln \Gamma \\ \varphi_\Gamma \\ l \end{bmatrix} \tag{1.23}$$

This way of characterizing the fault is similar to that described by equation (13) in **[41]**, but does not need a quadratic model for the coefficients $\alpha(\omega)$ and $\beta(\omega)$. This is, of course, only a special case of particular interest: other constraints on $\bar{\Gamma}(\omega)$ may make (**1.4**) and (**1.5**) a system of equations with a unique solution.

1.5 Test results on simulated cables

The aim of this Section is to evaluate, in typical cases, systematic errors of the proposed algorithms for SFWR. To this purpose, a set of tests have been performed on simulated cables, with exactly known parameters, and with noiseless SFWR signals. Errors associated to an imperfect knowledge of the cable or of the load parameters, and to the noise, are therefore eliminated.

Cables have been simulated using LineLab software **[43]**, a MATLAB-based simulator of quasi-TEM transmission lines. It can simulate transmission lines with arbitrary dispersion models, and arbitrary profiles of the frequency-dependent primary parameters R, C, G, L. All simulations have been carried out mimicking an RG58-CU coaxial cable. A dispersive model for the cable primary parameters have been used **[49]**, with geometrical and electrical parameters as shown in **Figure 1.6**. The nominal characteristic impedance of the cable is $Z_0 = 50\,\Omega$, and this is also the exact internal impedance of the generator in the simulations. The actual characteristic impedance of the cable is slightly different and frequency-dependent, as for any real cable. For example, at the frequency $f = 1\,\text{MHz}$, the true impedance is $|Z_0| \approx 49.5\,\Omega$, $\angle Z_0 \approx -0.12\,\text{rad}$.

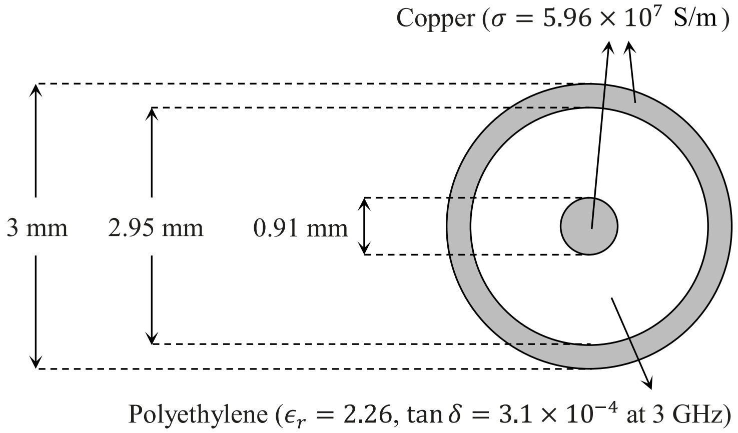

Figure 1.6: Cross section and electrical parameters of the simulated cable.

Both series and shunt faults have been simulated like in **[41]**. The series impedance (**Figure 1.7** a) may represent a defective point in the cable conductors (e.g. a junction), while the shunt impedance (**Figure 1.7** b) may represent a damage in the dielectric of the coaxial cable. The reflection coefficient of the series and shunt faults are, respectively:

$$\bar{\Gamma}_S = \frac{Z_S}{Z_S + 2Z_0} \tag{1.24}$$

$$\bar{\Gamma}_P = -\frac{Z_0}{Z_0 + 2Z_P} \tag{1.25}$$

where Z_S is the series impedance and Z_P is the shunt impedance.

Finally, in all the experiments the parameters of the SFWR signal are $\tau = 200\,\text{ns}$,

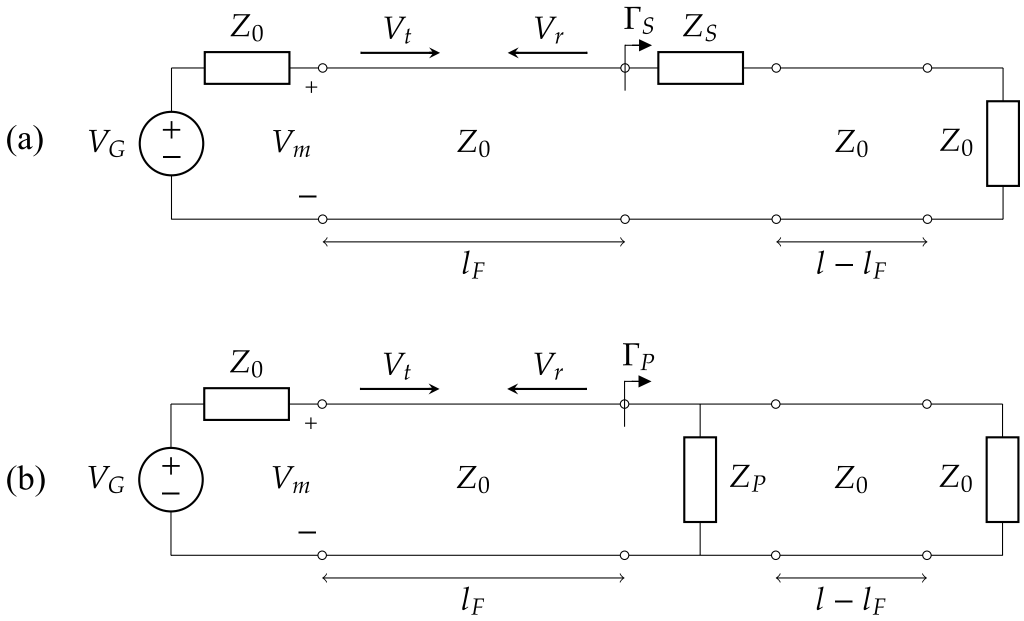

Figure 1.7: Simulated cables with series (a) and shunt (b) fault.

$T = 2\,\mu\text{s}$, $f_0 = 10\,\text{MHz}$, $N = 101$ frequencies, $\Delta f = 500\,\text{kHz}$, $f_{N-1} = 60\,\text{MHz}$. They have been chosen according to the criteria stated in **Section 1.2.2**, **1.3.3** and **1.4.2**.

1.5.1 Characterization of a reference cable

In this simulation, the cable is 50 m long, without faults and with open termination ($l = 50\,\text{m}$, $\Gamma = 1$). Functions $\hat{\alpha}(\omega_i)$ and $\hat{\beta}(\omega_i)$ have been obtained in the 101 test frequencies using (**1.16**), (**1.17**). Results are in **Figure 1.8**. The maximum relative error is 0.10% for the estimated $\hat{\alpha}(\omega)$, and 0.02% for the estimated $\hat{\beta}(\omega)$.

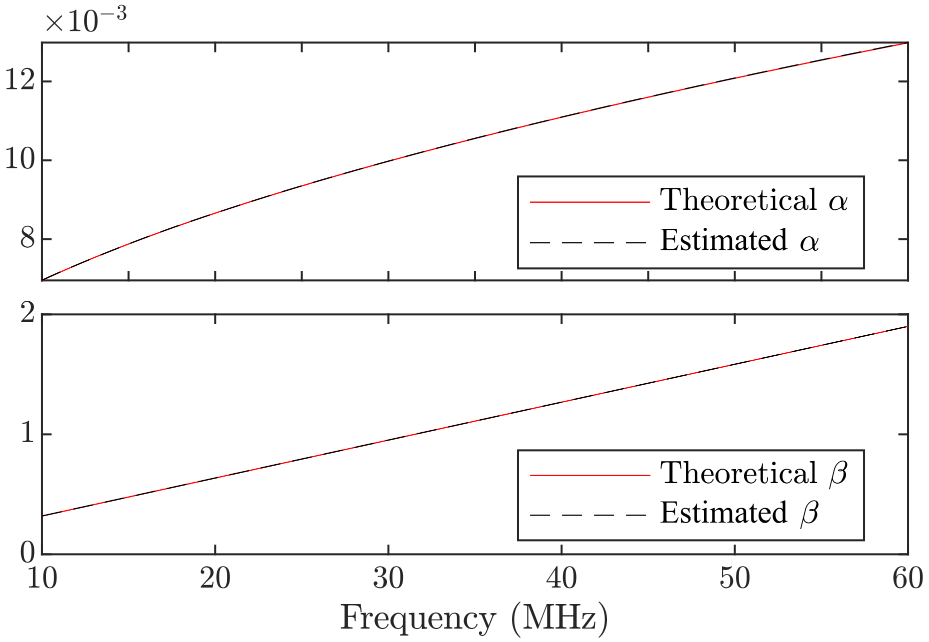

Figure 1.8: Theoretical and estimated $\alpha(\omega_i)$ and $\beta(\omega_i)$ in the simulated reference cable.

1.5.2 Fault location and characterization on a cable under test, with a generic reflection coefficient

In this simulation, the cable is 100 m long, and has a series capacitive fault at $l_F = 55\,\text{m}$ from the beginning of the line. The reflection coefficient at the fault is:

$$\bar{\Gamma}_S = \frac{Z_S}{Z_S + 2Z_0} = \frac{1}{1 + j\omega 2 Z_0 C_F} \tag{1.26}$$

where $C_F = 100\,\text{pF}$ is the fault capacitance. The fault position has been estimated using (**1.19**) for each ω_i, obtaining the results reported in **Figure 1.9**.

In accordance with (**1.20**), there is a systematic error decreasing at higher frequencies. At the highest frequency $f_{max} = 60\,\text{MHz}$ the estimate is $\hat{l} = 55.31\,\text{m}$, with a relative error $e_r \approx 0.6\%$, as foreseen by (**1.20**).

The estimation of the magnitude $\Gamma(\omega)$ of the reflection coefficient is shown in **Figure 1.10**. The maximum relative error over the theoretical value is 1.73%.

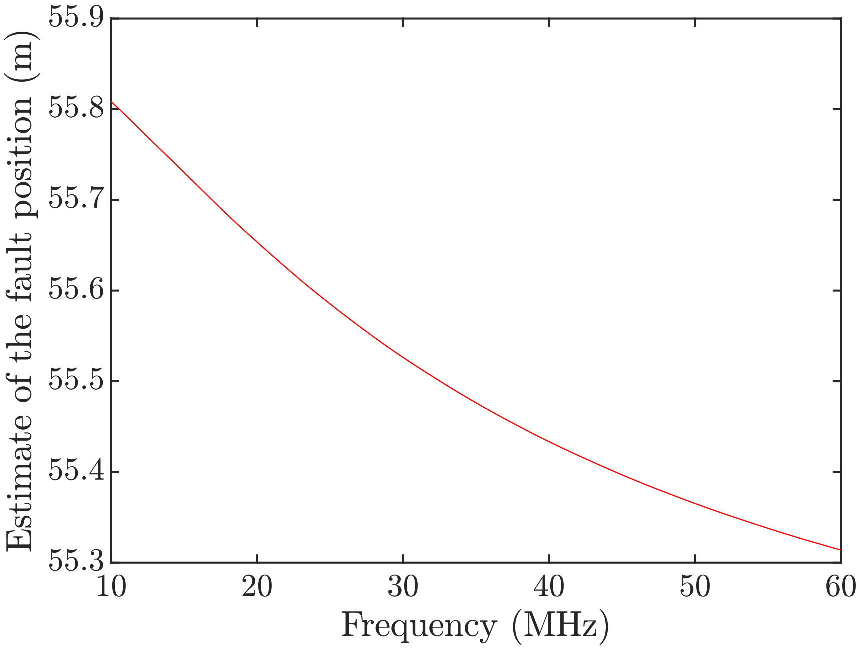

Figure 1.9: Estimate at various frequencies of the position of a series capacitive fault (true $l_F = 55\,\mathrm{m}$). The smaller systematic error is achieved at the maximum frequency.

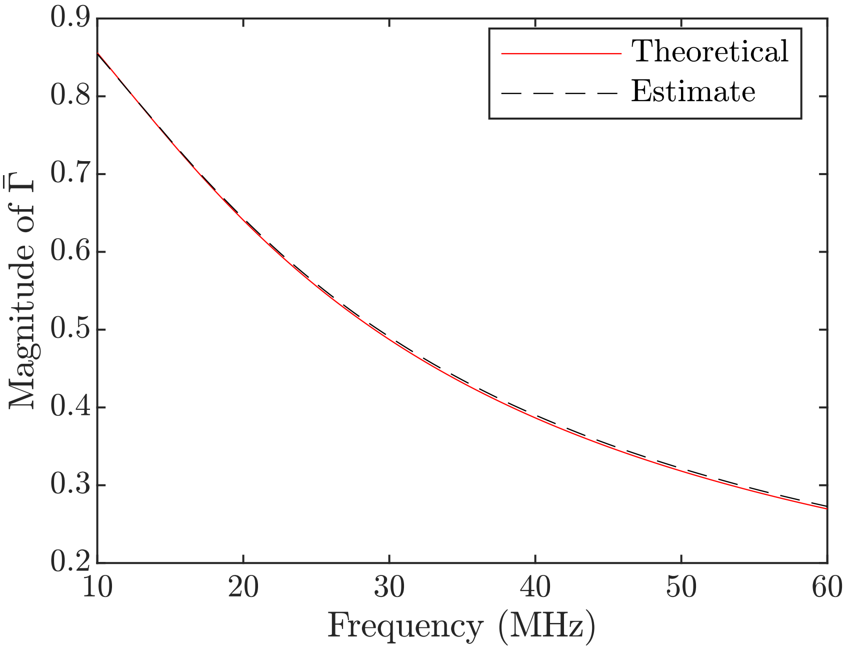

Figure 1.10: Estimate of the magnitude of the reflection coefficient $\Gamma(\omega)$.

1.5.3 Fault location and characterization on a cable under test, with a frequency-independent reflection coefficient

Reflection due to a mismatched load

For this case, a 100 m long cable terminated on a resistive load Z_L have been simulated. For a resistive load, $\bar{\Gamma}(\omega)$ is independent on the frequency and it is possible to perform the simultaneous measurement of l and $\bar{\Gamma}$ as described in **Section 1.4.3**. Seven values of Z_L have been simulated, including short circuit, open circuit, and $Z_L = 50\,\Omega \approx Z_0$. In this limit case, the reflection coefficient is not exactly zero because the simulated cable has a "real" behavior, and Z_0 is not exactly $50\,\Omega$.

Table 1.2 reports the estimations of l, while **Table 1.3** the estimations of $\bar{\Gamma}$. Estimation errors are in general very low. Meaningful errors are observed only for the phase φ_Γ, when the load is near or equal to the characteristic impedance. For $Z_L = 50\,\Omega$ estimation errors get slightly larger (the error on φ_Γ is not meaningful since $\Gamma \approx 0$), but the algorithms still achieve acceptable results.

Table 1.2: Estimated cable lengths

Z_L (Ω)	l (m)	$e_r(l)$ (%)
0	99.98	-0.0175
10	99.98	-0.0196
30	99.97	-0.0320
50	99.31	-0.693
100	100.0	-1.28×10^{-4}
300	99.99	-0.00606
∞	99.99	-0.00750

Table 1.3: Estimated reflection coefficient

Z_L (Ω)	Γ	$e(\Gamma)$	ϕ_Γ (°)	$e_r(\phi_\Gamma)$ (°)
0	0.9999	-1.36×10^{-4}	180.0	-0.00437
10	0.6506	-1.09×10^{-4}	179.5	-0.218
30	0.2233	-1.21×10^{-4}	177.7	-1.00
50	0.02748	-1.21×10^{-3}	23.50	13.0
100	0.3582	5.10×10^{-6}	1.299	0.569
300	0.7279	-6.48×10^{-5}	0.3395	0.146
∞	0.9999	-1.12×10^{-4}	0.004259	-0.00426

Reflection due to a series or a parallel fault

In these simulations the reflections are due to point-like impedance discontinuities in the cable, as represented in **Figure 1.7**. Mathematically, the situation is equivalent to that of a cable without faults, but with a mismatched load. Simulated fault impedances are purely resistive, so once again it is possible to perform measurements as described in **Section 1.4.3**. The circuit has been simulated considering a fault placed at $l_{F1} = 30\,\text{m}$ or $l_{F2} = 70\,\text{m}$ from the cable beginning with different values of impedances for each of the two fault types. **Table 1.4**, shows that the fault positions are estimation with very low systematic error in all the considered cases.

Also, the systematic error in the estimation of the reflection coefficient $\bar{\Gamma}$ is very low: the maximum relative error affecting $\hat{\Gamma}$ is 3.67×10^{-5}, while the maximum error affecting $\hat{\varphi}_\Gamma$ is 0.42 degrees.

Table 1.4: Estimated fault positions

	Z_F (Ω)	l_{F1} (m)	$e(l_{F1})$ (%)	l_{F2} (m)	$e(l_{F2})$ (%)
Series fault	20	29.996	-0.0130	69.990	-0.0141
	50	29.995	-0.0151	69.989	-0.0150
	100	29.995	-0.0172	69.989	-0.0159
	200	29.994	-0.0193	69.988	-0.0168
	500	29.994	-0.0213	69.988	-0.0177
Shunt fault	5	30.002	0.00782	69.996	-0.00517
	10	30.002	0.00631	69.996	-0.00582
	20	30.001	0.00432	69.995	-0.00668
	50	30.000	0.00159	69.995	-0.00785
	200	30.000	-0.00108	69.994	-0.00899

1.6 Experimental results

Effectiveness of the proposed algorithm has been demonstrated with tests in real situations too.

1.6.1 Experimental setup

The experimental setup used in tests is depicted in **Figure 1.11**. Both signal generation and acquisition are performed using a GW Instek MSO-2047EA oscilloscope, that is remotely controlled by a common personal computer. The output of the arbitrary waveform generator integrated in the GW Instek MSO-2047EA is connected to the input of the oscilloscope and to the cable under test through a T-connector. RG58-CU coaxial cables, of the same type of those used in simulations, have been used in all experiments.

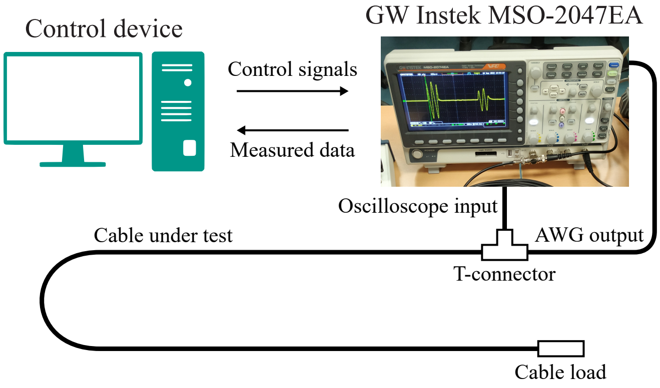

Figure 1.11: Experimental setup.

1.6.2 Characterization of a reference cable

First, the cable has been characterized as described in **Section 1.4.1**, using an open-ended 50 m long reference sample. The parameters of the SFWR signal were $\tau = 200\,\text{ns}$, $T = 2\,\mu\text{s}$, $f_0 = 10\,\text{MHz}$, $N = 51$ frequencies, $\Delta f = 1\,\text{MHz}$, $f_{N-1} = 60\,\text{MHz}$. The propagation function obtained from the estimation procedure is depicted in **Figure 1.12**.

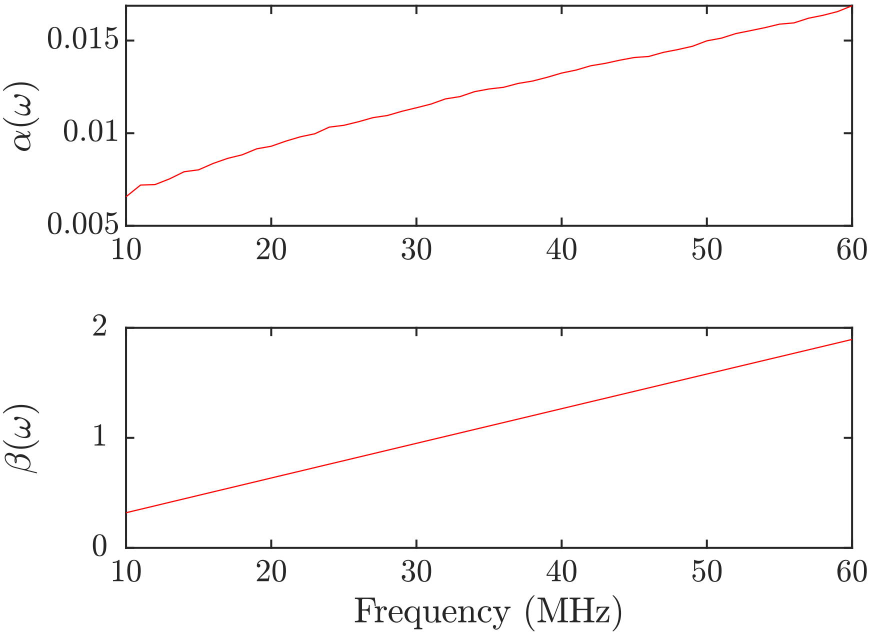

Figure 1.12: Results of the characterization of the reference cable.

1.6.3 Fault location and characterization on a cable under test terminated on a resistive load

Then a 100 m long cable, terminated on different resistive loads, has been analyzed. Some portions of the measured signal when the cable had a short-circuit termination are reported in **Figure 1.13**. The reflection coefficient and the cable length have been estimated as described in **Section 1.4.3**. Even if very cheap instruments have been used to arrange the experimental setup, estimation results reported in **Table 1.5** demonstrate the accuracy of the algorithm.

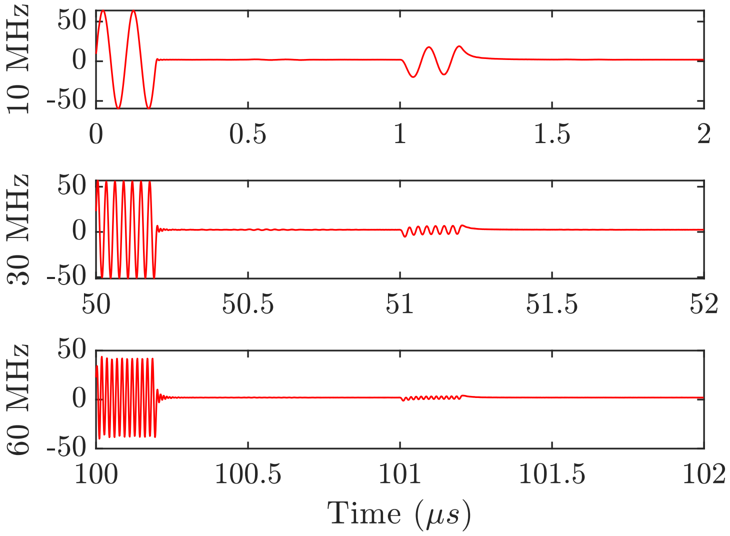

Figure 1.13: Example of measured signal for a 100 m long coaxial cable terminated on a short circuit.

Table 1.5: Estimated length and reflection coefficient

Z_L (Ω) (nominal value)	$\bar{\Gamma}$ (nominal value)	$\hat{\Gamma}$	$\hat{\varphi}_\Gamma$ (°)	l (m)
0	-1	1.04	171.4	100.33
25	-0.333	0.355	174.3	100.05
100	0.333	0.337	-3.182	99.99
∞	1	1.04	-4.841	100.01

1.7 Separation of overlapping reflected signals

When a reflected burst overlaps with a transmitted burst or with another reflected burst, the procedure described in previous sections is not applicable straightforwardly. In this section, a method for separating overlapping reflected sinusoidal burst and hence locate and characterize cable faults in such case is described [34]. This method extends the algorithms for SFWR described in previous sections.

Various techniques have been developed, over the years, to deal with the problem of overlapping signals, mainly in applications related to the analysis of echo signals in ultrasonic microscopy and nondestructive evaluation. In situations where a linear frequency modulated signal is transmitted, the use of the Fractional Fourier Transform is very effective, since reflected signals do not overlap in the time-frequency plane. Therefore, overlapping signals can be transposed to the Fractional Fourier Domain, where single components can be easily separated and transformed back to time-domain [50], [51]. A spectral estimation method for nonstationary signals [52] can also be used to extract instantaneous amplitudes and phases of reflected signals. In SFWR technique, sinusoidal bursts are used, anyway, so reflected signals overlapping in time-domain, overlaps in frequency domain too, making this technique unfitting for the purpose.

Techniques based on the sparse representation theory are also very used for the purpose of overlapping signals separation [53]. Several solutions exploiting advanced sparse representation or decomposition have been recently proposed in the literature to either enhance performance [54] or identify the behavior [55] of different systems; attention must be paid on the influence that possible uncertainty sources can have on the final reconstruction of desired information [55].

In sparse representation techniques, the objective is to find an approximate solution to the underdetermined problem

$$y = D\alpha$$

where $y \in \mathbb{R}^{N\times 1}$ is the signal we want to approximate, $D \in \mathbb{R}^{N\times M}$, with $M \gg N$, is an overcomplete dictionary of elementary signals (called atoms), $\alpha \in \mathbb{R}^{M\times 1}$ is the vector of parameters to be estimated that we want it to be as sparse as possible. The matching pursuit algorithm is able to find the sparsest approximation of the signal

$$\hat{y} = D\hat{\alpha}$$

by adding one atom per iteration to the estimated signal until the residue

$$r = y - \hat{y}$$

gets lower than a given threshold.

Mor et al. proposed a modified version of the matching pursuit algorithm, named Support Matching Pursuit (SMP), in which both the energy and the support (i.e. the number of zero elements of the vector) of r are minimized during each iteration **[56], [57]**. SMP is also used in **[58]**, but the dictionary of elementary signals is here constructed including physical effects due to propagation and reflection of the signal through the medium. In **[59], [60]** a convex version of the minimization problem is defined that can be therefore analyzed with existing solvers, e.g. CVX. In **[60]**, furthermore, singular value decomposition is used to reduce dimensionality of signals and the effect of noise.

Li et al. developed a signal processing method for detecting near-surface defects in metal materials through ultrasonic microscopy **[61]**. The algorithm they proposed, based on a deconvolution technique, can find the position of defects when they are located near the surface of the material under test and the echo they produce overlaps with the echo produced by the surface, having however a much lower amplitude. Other techniques have been proposed to address the problem of overlapping signals separation in reflectometric applications, including forward-backward optimization algorithms **[62]** and ridge path regrouping **[63]**, that works in the time-frequency domain.

Like in other cited works, the sparsest representation of the measured signal is researched. The case of coaxial cables presenting impedance discontinuities is treated in this Section too, for the sake of simplicity and uniformity, but the method can be applied in all classical reflectometry measurements.

1.7.1 Conditions that cause overlapping reflected signals

Overlapping occurs, for example, when two discontinuity points are near enough that the difference of the delays of reflected bursts they produce is:

$$\Delta\tau_d = \frac{2\Delta l}{v_p} < \tau$$

where Δl is the distance between the two discontinuities, v_p is the propagation velocity of signals inside the TL. Likewise, if a discontinuity point is at distance $\Delta l < v_p \cdot \tau/2$ from the beginning of the line, the reflected burst will overlap with the transmitted one. An example of measured signal where a reflected burst is overlapping with the transmitted one is depicted in **Figure 1.14**.

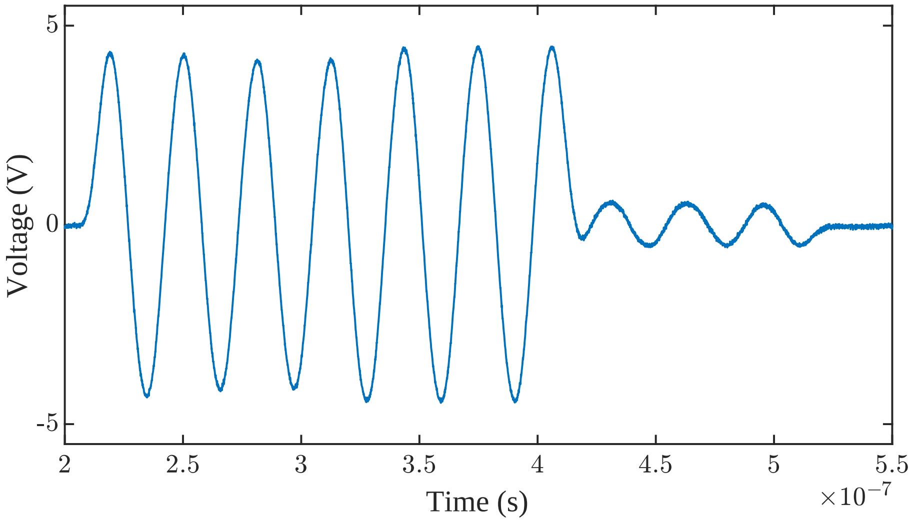

Figure 1.14: Example of two overlapping bursts

A procedure for finding the starting instant of reflected bursts and estimating amplitudes and phases of transmitted and reflected sinusoids is described below. We will assume in the following that the measured signal is divided into segments of duration T or, equivalently, that bursts at each frequency are transmitted singularly to the beginning of the TL. The measured signal at frequency ω_i is denoted by:

$$y_n^{(i)}$$

where $n = 0, 1, ..., N_S - 1$ and N_S is the number of samples of the signal.

1.7.2 Finding regions containing bursts

The first step in the algorithm for bursts separation is finding regions, in the measured signal, that actually contain bursts. Knowledge of the frequency of the transmitted and reflected signal can be exploited for this purpose. Instantaneous amplitude at frequency ω_i is indeed computed through OLS estimation with a sliding-window of duration

$$W = \frac{\tau}{10T_S}$$

where T_S is the sampling period. Instantaneous amplitude $d_n^{(i)}$ is, therefore, calculated with an OLS estimation in the interval $[n - W/2; n + W/2]$. Regions where instantaneous amplitude is over a given threshold are then selected. Finally, neighbouring regions are merged and resulting regions with duration shorter than τ are discarded.

1.7.3 Finding starting instants of bursts

The algorithm for finding the starting instant of each burst in the signal is applied singularly on each of the regions defined above. The measured signal is modeled like the sum of N_B sinusoidal bursts:

$$\hat{y}_n^{(i)} = \sum_{m=1}^{N_B} d_m \cos(\omega_i t_n + \varphi_m) \mathrm{rect}\left(\frac{t_n - \tau_{d,m} - \frac{\tau}{2}}{\tau}\right) \tag{1.27}$$

where $t_n = nT_S$, d_m is the amplitude of the m-th sinusoidal burst, φ_m is its phase, $\tau_{d,m}$ is its starting instant.

The objective of the algorithm is to find the vector of parameters

$$\boldsymbol{\theta} = [N_B, d_1, \varphi_1, \tau_{d,1}, \dots, d_{N_B}, \varphi_{N_B}, \tau_{d,N_B}]$$

that minimizes the energy of the estimation residual:

$$\|r^{(i)}\|_2^2 = \sum_{n=0}^{N_S-1} (y_n^{(i)} - \hat{y}_n^{(i)})^2 \tag{1.28}$$

while keeping $N_B \leq N_{B,max}$.

The number of bursts is set to $N_B = 1$ in the first iteration and it is then increased until (**1.28**) gets lower than a threshold set to

$$r_{th}^{(i)} = \frac{1}{100} \sum_{n=0}^{N_S-1} y_n^{(i)2}$$

or the maximum number of bursts $N_{B,max}$ is reached. Parameters of vector $\boldsymbol{\theta}$ are adjusted during each iteration, in which N_B remains constant, to minimize (**1.28**). The minimization procedure starts by considering N_p linearly spaced points in the region and calculating all possible combinations of starting instants of the N_B bursts in these points. Model (**1.27**) is then fitted considering each of these combinations and the one that produces the lower residual energy (**1.28**) is selected. The procedure is, therefore, repeated considering N_p points between the point preceding and following each of the starting instants previously chosen, until the distance between points gets to one sample.

1.7.4 Alignment and cleaning of starting instants

Starting instants of bursts obtained for the frequencies of the transmitted signal are aligned assuming that the first for each frequency is the starting instant of the transmitted burst. Instants that have not been obtained at every frequency are then discarded. Since starting instants are not exactly equal at every frequency, a tolerance interval must be used to compare them during this operation.

1.7.5 Sinusoid parameters estimation

Amplitude and phase of each sinusoidal burst are finally estimated using model (**1.27**), slightly modified to allow correct phase unwrapping, as described in **Section 1.3**:

$$\hat{y}_n^{(i)} = \sum_{m=1}^{N_B} d_m \cos\left[\omega_i(t_n - \tau_{d,m}) + \varphi'_m\right] \operatorname{rect}\left(\frac{t_n - \tau_{d,m} - \frac{\tau}{2}}{\tau}\right)$$

The phase of each burst is, therefore, unwrapped:

$$\varphi_m = \varphi'_m - \omega_i \tau_{d,m}$$

The algorithm for evaluating the position and reflection coefficient of each discontinuity point, described in **Section 1.3**, can hence be applied.

1.7.6 Experimental results

The burst separation algorithm has been evaluated in experimental tests on coaxial cables, where the overlapping condition has been caused by placing an impedance discontinuity near the beginning and the end of the cable.

Experimental setup

The transmitted signal has been generated with an Agilent 33250A Arbitrary Waveform Generator (AWG). The output of the AWG has been connected through a T-connector to the input of the LeCroy Waverunner-2 LT262 oscilloscope and to the cable under test. Both instruments have been remotely controlled through their GPIB interface. RG58-CU coaxial cables, of various lengths and in different configurations, have been used in all tests. A photograph of the experimental setup is reported in **Figure 1.15**.

The following parameters of the transmitted signal have been chosen for all tests using criterion defined in **[33]**: $N = 4$, $f_0 = 20\,MHz$, $\Delta_f = 4\,MHz$, $\tau = 200\,ns$, $T = 2\,\mu s$.

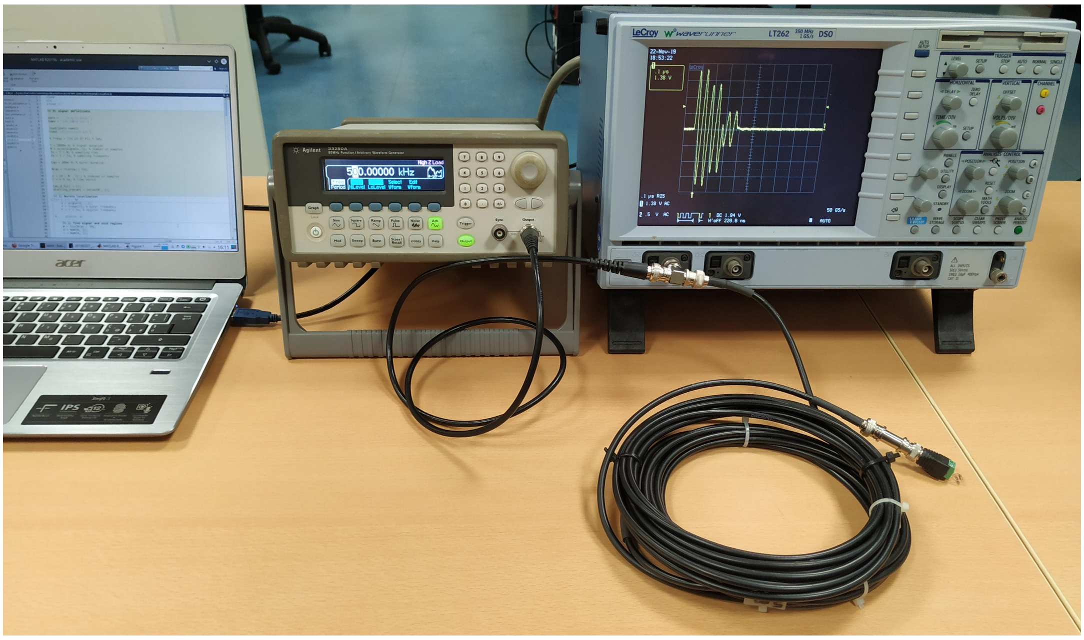

Figure 1.15: Photograph of the experimental setup

Characterization of the cable

The calibration has been performed using a 50 m long cable terminated on a open circuit. This preliminary test is needed to estimate the propagation function $\gamma(\omega_i)$ of the cable which is used in the following calculations, i.e. to write problem (**1.23**). Estimation results are represented in **Figure 1.16** for the four considered frequencies.

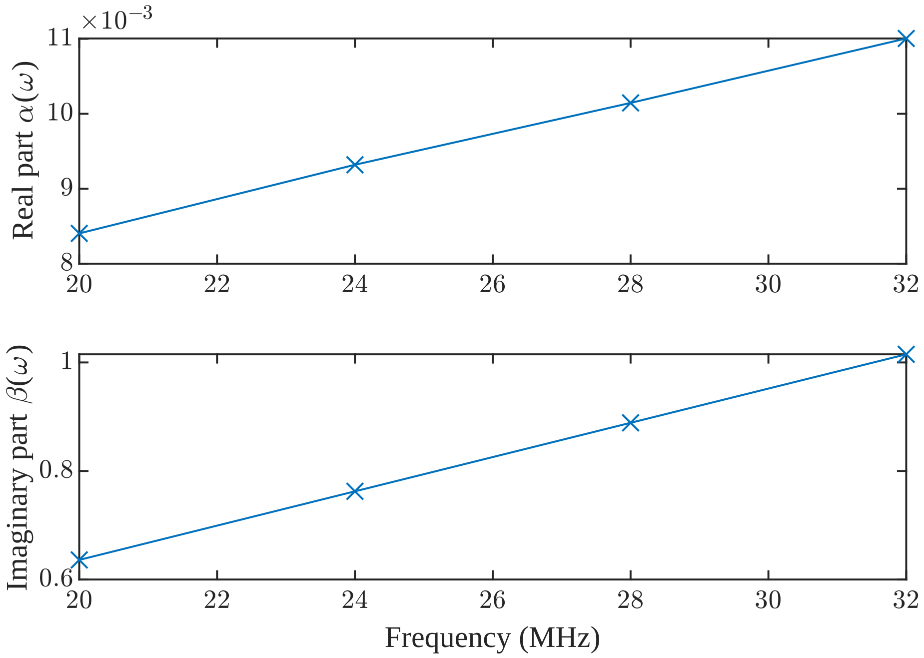

Figure 1.16: Estimate of the propagation function of the cable

Fault near the beginning of the cable

The first evaluation experiment has been performed on a 10 m long cable that has been terminated on different resistive loads. In this case the transmitted burst is overlapping with the burst reflected at the termination of the cable, similarly to the situation of **Figure 1.14**. The algorithm has been able lo locate the starting instant of the two bursts in each load condition, and an estimation of the reflection coefficient has been hence computed. **Table 1.6** contains a comparison between estimation results and nominal values, computed considering $Z_0 = 50\,\Omega$ as the characteristic impedance of the cable. As can be seen, an accurate estimate of the cable length and of the magnitude of the reflection coefficient has been obtained. More relevant errors have been found only estimating the phase of the reflection coefficient when its magnitude was small.

Table 1.6: Termination characterization

Nominal values		**Estimates**		
$Z_L(\Omega)$	$\bar{\Gamma}$	$\hat{\Gamma}$	$\hat{\varphi}_\Gamma$ (deg)	$\hat{l}$ (m)
12	-0.6129	0.6176	176.9	10.18
22	-0.3889	0.3955	175.6	10.20
39	-0.1236	0.1359	147.8	10.05
68	0.1525	0.1554	34.92	10.31
100	0.3333	0.3495	2.436	10.03
270	0.6875	0.6939	7.425	10.17
∞	1	1.057	2.535	10.04

Fault near the end of the cable

In the second evaluation experiment, a shunt fault has been placed 10 m before the termination of a 60 m long open-end coaxial cable and hence overlapping occurs between bursts reflected at the two impedance discontinuities. Estimation results are in **Table 1.7** and **1.8**. The burst reflected at the fault interface has not been detected for $Z_P = 270\ \Omega$ and the amplitude of the reflected burst was very small. Estimation produced very accurate results in other conditions.

Burst reflected at the termination has not been detected, instead, for $Z_P = 12\,\Omega$, since the signal transmitted after the fault is very small. Accurate estimates of the cable length have been obtained in each load condition, while the estimation of the reflection coefficient led to meaningful errors only when amplitudes of the two reflected bursts have been very different each other.

Table 1.7: Fault characterization

Nominal values		**Estimates**		
$Z_P(\Omega)$	$\bar{\Gamma}$	$\hat{\Gamma}$	$\hat{\varphi}_\Gamma$ (deg)	$\hat{l}_F$ (m)
12	-0.6757	0.6833	179.8	50.16
22	-0.5319	0.5636	178.7	50.13
39	-0.3906	0.4228	179.7	50.11
56	-0.3086	0.3346	177.6	50.09
68	-0.2688	0.2937	178.9	50.07
100	-0.2000	0.1998	171.4	49.99
270	-0.0847	-	-	-

Table 1.8: Termination characterization

$Z_F(\Omega)$	$\hat{\Gamma}$	$\hat{\varphi}_\Gamma$ (deg)	$\hat{l}$ (m)
12	-	-	-
22	1.2298	4.084	59.88
39	1.0641	1.440	59.97
56	1.0016	-2.560	59.99
68	1.0296	-2.995	60.01
100	0.9049	-15.43	59.92
270	0.7931	13.18	60.22

1.8 Conclusions

This chapter presents a development of the interesting theory and methods presented in **[41]**, to perform the reflectometry with sinusoidal bursts named SFWR. The main achieved results are the following.

1. Formulae are given to choose the burst duration τ, the separation between bursts T, and the frequency range $[\omega_{min}; \omega_{max}]$ of the bursts.

2. An algorithm is proposed to obtain the FRF $\bar{H}(\omega)$ at any frequency ω_i using a modified sinusoidal OLS fitting. The algorithm takes into account the fact that the response of $\bar{H}(\omega)$ to a sinusoidal burst contains transient terms, and is therefore a valid alternative to the time-frequency analysis employed in **[41]**.

3. Algorithms are presented to extract the fault location l and the fault reflection coefficient $\bar{\Gamma}(\omega)$ from the knowledge of $\bar{H}(\omega_i)$, even at a single frequency. These algorithms add up to those described in **[41]**, which are perfectly valid, but requires some constraints (quadratic model of the propagation function, $\bar{\Gamma}$ independent on the frequency). Besides, the resolution in the measurement of l is not linked to the number of frequencies.

4. Systematic errors associated to the method are determined by a simulation study, with cable and faults of realistic but exactly known characteristics. The errors are demonstrated to be negligible or very low. By considering the results here with that in **[41]**, the feasibility of SFWR as a low-cost but very accurate reflectometric method is fully demonstrated.

Furthermore, some variations to the SFWR technique to address the case of multiple discontinuity points producing overlapping reflected signals are also developed. Starting from a simple modeling of the measured signal, the proposed method is capable, through an iterative procedure, to effectively distinguish more overlapping sinusoidal bursts. Experimental tests have been carried out to evaluate performances of the algorithm in real-world applications. Results of experiments shows that the proposed algorithm is suited for accurately estimate the position of multiple reflecting interfaces in coaxial cables. Reflection coefficient also is estimated with good accuracy when the amplitude of the reflected burst is sufficiently high.

Chapter 2

Detection and characterization of multiple discontinuities with TDR and CNNs[1]

2.1 Introduction

In recent years, artificial neural networks have been used in many data analysis problems, among which is also the processing of reflectometry signals. The increasing adoption of these models is due to their impressive performances in performing operations that are not easily feasible using conventional signal processing techniques. In **[64]**, an approach for fault detection and assessment in instrumentation and control cables has been proposed that makes use of time-frequency domain reflectometry (TFDR) and region-based convolutional neural networks (R-CNNs). A Gaussian envelope with a linear chirp is used as a stimulus signal in TFDR. Reflected signals measured at the cable beginning are represented in the time-frequency domain first, using the Wigner-Ville distribution. The obtained RGB images are then analyzed through the R-CNN to find the location of the reflected signals in the time-frequency domain. Additionally, a model of the reflected signals is derived from a preliminary measurement on a cable with a known length. This model is used for generating the training dataset for the neural

---

[1] This Chapter is based on the paper **[36]**

network and for filtering out the reflected signals due to multiple reflections. The proposed technique is tested in the case of a single resistive fault in a branched network cable or in a cable without branches, while the case of multiple faults (two faults are considered) is only qualitatively analyzed. An enhanced version of TFDR (without using neural networks) is also used in **[65]**, where both the case of localized resistive faults and of localized ohmic-capacitive faults are analyzed.

In **[66]**, a multi-layer perceptron neural network (MLP-NN) is used for the detection of soft faults in wire networks. Since branched networks are considered, the reference signal is injected in multiple points to resolve ambiguities in the identification of branches containing faults. Before sending reflectometry data to the MLP-NN, a pre-processing step is performed. The difference between the measured reflectometry signals and reflectometry signals obtained on a healthy network is computed, and after a thresholding process, the positions and amplitudes of the peaks in the difference signals are found. These data are the input of the MLP-NN, while its outputs are the estimated positions and impedances of the detected soft faults. The usage of genetic algorithms is also explored for the same purpose, leading to accurate estimation results. An MLP-NN with TFDR is also used in **[67]**, for fault detection in multi-core C&I cables. The aim of the method proposed in **[67]** is to detect the presence and position of a fault and also to differentiate the faulty line within the multi-core cable. In fact, when a line is faulty, the other lines are also affected due to crosstalk.

A generalized regression neural network (GRNN) is used in **[68]** for the localization of faults in rail tracks. In this case, FDR is used for diagnosis, considering the rails as the wires of the transmission line under test. The amplitude versus frequency waveform obtained with the FDR is exploited to localize the fault, using the GRNN for non-linear regression. The type of fault (short or open) is deducted by looking at the initial inclination of the amplitude versus frequency waveform. A GRNN is also used in **[69]** for the analysis of features extracted from TFDR signals for shielded cables diagnosis. In particular, the purpose is to detect faults in the cable. Three features are extracted from the TFDR signals: the time delay of the reflected signal, its amplitude, and the time-frequency phase difference between the reference and the reflected signal. The GRNN uses these features as input and produces an estimate of the position and reflection coefficient of the discontinuity point. Experimental results are provided considering a single localized fault, of various entities, in the cable or at its end.

This chapter presents a method based on TDR with convolutional neural networks (CNNs) for the localization and characterization of multiple impedance discontinuity points in cables. TDR is probably the most common reflectometric method, owing to the simplicity of the stimulus signal (a narrow pulse or a short rise time step) and of the measurement process. This implies that devices for TDR are also available at a lower cost. According to the proposed method, TDR signals are analyzed by means of a 1D-CNN that estimates the position and impedance of the discontinuity points in the cable under test. The neural network identifies all the discontinuity points, including the line termination, and hence, classification is also performed: each detected fault is associated with a class (capacitive fault or line termination).

The main advantages of the proposed method over the others found in the literature are the following:

- No pre-processing and extraction of features from the measured signals is required. This implies less computational burden and better exploitation of the deep learning paradigm. When working directly with raw data, deep neural networks can indeed select the optimal features to extract for the given task. Additionally, a more simple and general estimation procedure is obtained;
- Accurate localization and characterization of multiple discontinuity points in the cable;
- The neural network is trained using TDR signals generated with a transmission line simulator. Even though an accurate model of the cable is required to obtain good results, once it has been created, it can be used to generate training datasets to make the neural network work in different conditions;
- The neural network can work with any cable of the same type as those used in the training set, with a variable length.

2.2 Materials and methods

2.2.1 Measurement setup

RG58-CU coaxial cables containing capacitive faults are studied. This setup is used as an example for developing and testing the proposed method since it is strictly controllable. However, the method can also be used for setup containing other types of cables and discontinuities, given that all the operations described in the following are not specific to the considered setup.

The considered situation is depicted in **Figure 2.1**. The cable had total length l and contained N_F localized faults, simulated by means of capacitors connected in parallel to the cable's conductors through T junctions. The capacitors are placed at a distance z_i from the beginning of the cable and had the capacity C_i. The stimulus signal is generated by an Agilent 33250A arbitrary waveform generator (AWG), while the TDR signals are acquired using a LeCroy Waverunner-2 LT262 oscilloscope.

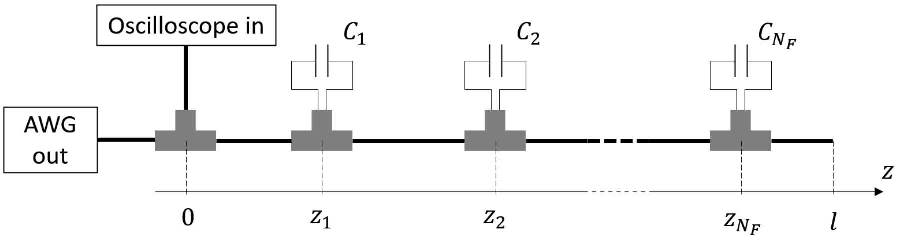

Figure 2.1: Representation of the measurement setup. TDR is applied to a cable containing N_F parallel faults to estimate the N_F pairs of values z_i, C_i.

A Gaussian pulse is used as a stimulus signal since it is concentrated in both time and frequency domains. A time-limited signal is useful to have cleaner reflectometry signals while a frequency-limited signal allows to perform frequency-domain simulations such as those described in **Section 2.2.3**. The stimulus signal is therefore defined as

$$v_G(t) = \mathrm{e}^{\frac{-(t-t_0)^2}{2\sigma^2}} \tag{2.1}$$

where $\sigma = 8.1\,\mathrm{ns}$ (the lowest achievable with the hardware used for experiments) and $t_0 = 100\,\mathrm{ns}$. In experiments, a sampling frequency of 250 MHz is used for the acquisition of reflectometry signals. The number of samples acquired for each TDR signal is $N = 1024$, corresponding to a time duration of ~4 µs. This duration is sufficient to see all the reflected signals, considering that the velocity of EM waves in RG-58CU cables is $\sim 2 \times 10^8$ m/s, and cables no longer than 200 m are considered.

2.2.2 Neural network

The neural network for faults localization and characterization proposed in this chapter is inspired by single-shot CNNs for object detection in images **[70], [71]**. The main component of these neural networks is a sequence of convolutional and pooling layers that have the purpose of extracting features from the images being analyzed. The level of abstraction of the extracted features increases moving toward the final layers. The result produced by this stack of convolutional layers is a set of 2D feature maps that are then further processed by densely connected layers or additional convolutional layers to finally estimate the bounding boxes containing the objects in the image and associate a class to each of them.

Since time-domain signals are the object of our study, we use 1D convolutional layers instead of 2D ones as the base component of the model. The proposed neural network for faults localization and characterization is depicted in **Figure 2.2**. The input of the first layer of the neural network is the measured TDR signal that has a size of 1024×1. The first layer contains eight convolution kernels of length 15, corresponding to a time duration of 60 ns. This value is chosen to match the time duration of the stimulus signal and the reflected signals. The rectified linear unit (ReLU) is used as an activation function. The 1D max-pooling operation is then applied to the output of the convolutional layer, using a pool size of 2. The output of the neural network is therefore downscaled from 1024×8 to 512×8. The same operations (convolution, activation, pooling) are performed in five layers of the neural network, with the only difference in the number and size of convolution kernels. The five layers contain, respectively, the following:

- A total of 16 kernels of size 11×8;
- A total of 32 kernels of size 5×16;

- A total of 64 kernels of size 5×32;
- A total of 128 kernels of size 5×64;
- A total of 256 kernels of size 5×128.

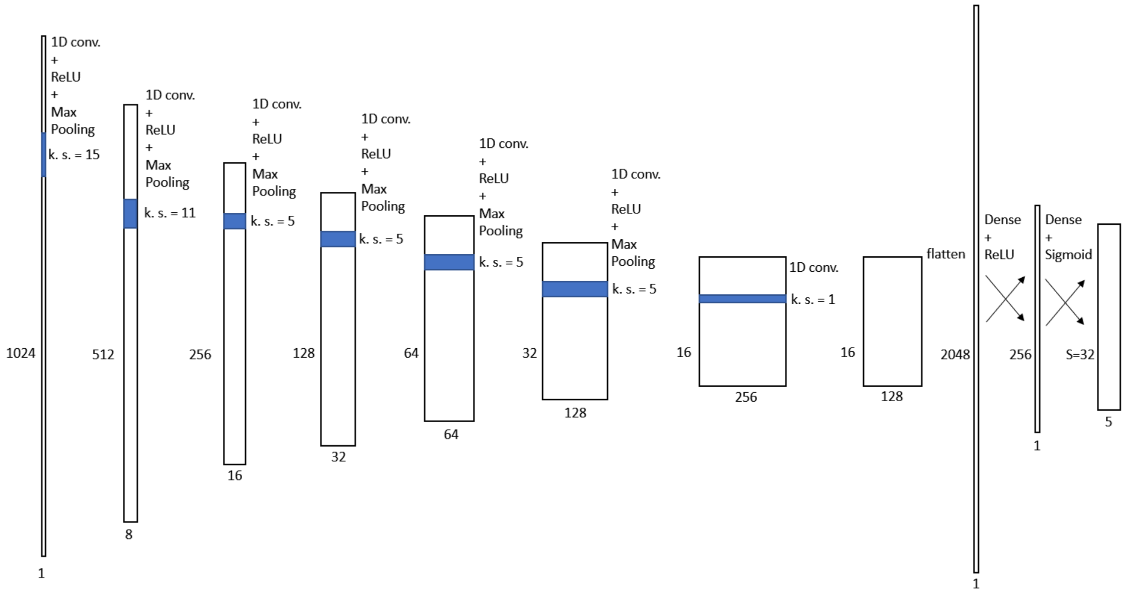

Figure 2.2: Neural network proposed for the localization and characterization of the faults.

The last convolutional layer has the only purpose of dimensionality reduction. Therefore, it contains 128 kernels of size 1×256, and no activation and pooling operations are performed.

This sequence of convolutional layers serves to create an abstract representation of the problem. In this way, the neural network could consider accurately all the information contained in the reflectometry signal, e.g., ignoring reflected signals due to multiple reflections.

The feature maps produced by the last convolutional layer are then flattened to a 2048×1 array that is sent to the last two densely connected layers of the network. The first of them contains 256 artificial neurons and uses the ReLU activation function, while the second contains $5 \cdot S$ artificial neurons and uses the sigmoid activation in order to have outputs in the range (0–1). The output of the last layer is finally reshaped to build an $S \times 5$ matrix, whose rows are the predictions produced by the neural network. The range of length that can contain a discontinuity point is divided into S cells. The i-th prediction represents the estimated discontinuity point in cell i. Each prediction is an array of the following five elements:

- The first element indicates the normalized position of the discontinuity points relative to the range of lengths in the cell;
- The second and third elements indicates the class of the predicted discontinuity point. If the first of these two elements is greater than the second, a capacitive fault is predicted; an open termination of the line is predicted otherwise;
- The fourth element quantifies the capacity value. This is also a normalized value relative to the range of possible capacity values. If a line termination is predicted, this value is neglected;
- The last element indicates the probability score of the prediction.

At inference time, only predictions with a probability score greater than a given threshold are selected, and their characteristics are derived from the other four parameters produced by the neural network for each prediction.

2.2.3 Dataset generation and training procedure

A great quantity of data is required to train neural network models, and this is especially true for deep neural networks. The neural network described in the previous Subsection requires a TDR signal such as those described in **Section 2.2.1** as input data and a list of the impedance discontinuity points in the cable as target data. A TL simulator **[43]** is adopted to produce an adequate number of samples, each of them accompanied by a label containing information about the faults in the cable and the cable length.

Simulation procedure

Using classical microwave theory, the RG58-CU cable is modeled similarly to a TL composed of elementary cells such as that depicted in **Figure 2.3**.

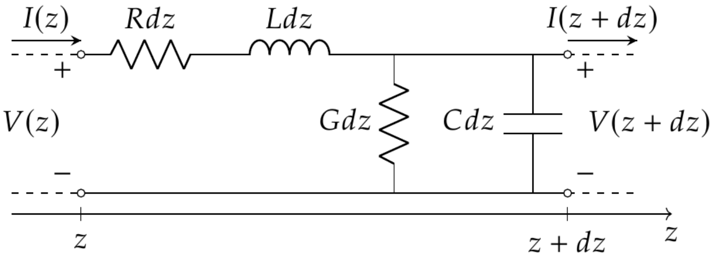

Figure 2.3: Elementary cell of a transmission line.

The theoretical formulation of the primary parameters of the TL is computed considering the dielectric dispersion and the skin effect. The resulting primary parameters are

$$R(\omega) = \frac{1}{\sigma_c \pi r_i^2} + \frac{1}{\sigma_c \pi \left[(r_o + t)^2 - r_o^2\right]} + \frac{1}{2\pi}\left(\frac{1}{r_i} + \frac{1}{r_o}\right)\sqrt{\frac{\omega \mu_0}{2\sigma_c}} \tag{2.2}$$

$$L(\omega) = \frac{\mu_0}{2\pi} \ln \frac{r_o}{r_i} + \frac{1}{2\pi\omega}\left(\frac{1}{r_i} + \frac{1}{r_o}\right)\sqrt{\frac{\omega \mu_0}{2\sigma_c}} \tag{2.3}$$

$$G(\omega) = \omega \tan\delta \frac{2\pi\epsilon_0\epsilon_r}{\ln(r_o/r_i)} \tag{2.4}$$

$$C = \frac{2\pi\epsilon_0\epsilon_r}{\ln(r_o/r_i)} \tag{2.5}$$

where ω is the angular frequency, μ_0 is the vacuum permeability, and ϵ_0 is the vacuum permittivity. The other symbols in the equations are the geometrical and electrical parameters of the coaxial cable defined in the scheme of **Figure 2.4** as follows:

- r_i—Inner conductor ray;
- r_o—Outer conductor ray;
- t—Outer conductor thickness;
- σ_c—Copper conductivity;
- ϵ_r—Insulator relative permittivity;
- $\tan\delta$—Insulator loss tangent.

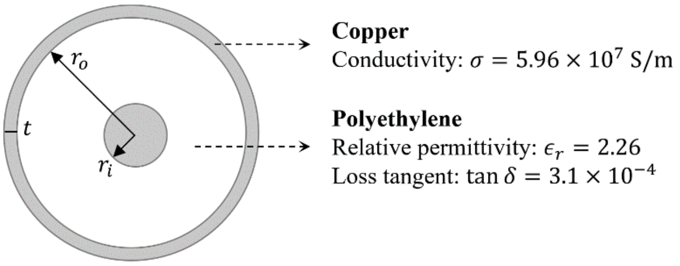

Figure 2.4: Section of the RG58-CU cable.

The effectiveness of the TL model in representing the coaxial cable is evaluated by comparing simulated TDR signals with experimental signals measured in the same configurations. As can be seen in **Figure 2.5**, the theoretical model is not able to accurately represent the cable. In particular, the differences in the shape of the reflected signals indicate poor modeling of the frequency-domain behavior of the coaxial cable.

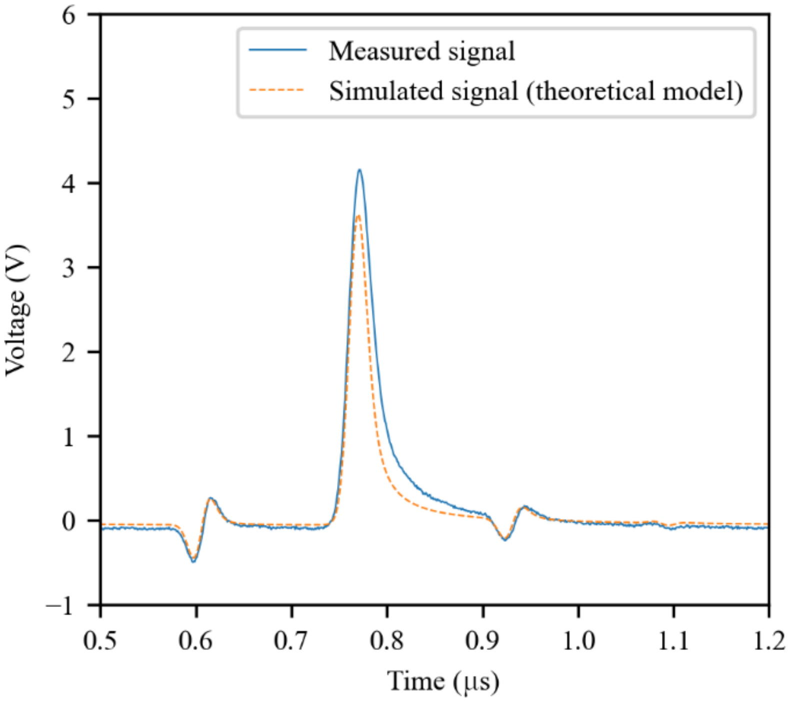

Figure 2.5: An experimental TDR signal compared with a simulated signal obtained using the theoretical model of the coaxial cable. The cable is 66 m long, with a parallel capacitive fault of 47 pF at 50 m. The first reflected signal is due to the fault, while the second is due to the cable's open termination.

Calibration of the RG58-CU cable parameters

A calibration procedure is developed to extract a more accurate model of the primary parameters of the RG58-CU cable. From well-known theory, the propagation function of electromagnetic waves in TLs depends on the primary parameters according to equation (**1.1**). As demonstrated in **[33]**, using the SFWR technique, a measurement of $\alpha(\omega)$ and $\beta(\omega)$ can be obtained for any value of ω. In particular, they can be measured in a range of frequencies of interest and then used to derive an estimate of the primary parameters of the TL in those frequencies.

From (**1.1**), the following equation is derived:

$$\gamma^2 = \alpha^2 - \beta^2 + 2j\alpha\beta = RG - \omega^2 LC + j\omega(RC + LG) \tag{2.6}$$

Starting from Equation (**2.6**), only one pair between R, L and G, C can be estimated using a linear regression technique, e.g., the OLS method. Since the main contribution to the frequency-domain behavior of the TL is derived from the primary parameters R and L, it has been decided to estimate them, maintaining the theoretical formulation for G and C instead. The frequency-domain model of R and L is therefore derived from Equations (**2.2**) and (**2.3**) respectively.

$$R(\omega) = R_0 + R_1\sqrt{\omega} \tag{2.7}$$

$$L(\omega) = L_0 + L_1\frac{1}{\sqrt{\omega}} \tag{2.8}$$

where R_0, R_1, L_0, L_1 are the parameters to be estimated with the fitting procedure.

Hence, using Equation (**2.6**), the following OLS problem is defined:

$$\begin{bmatrix} G(\omega_1) & G(\omega_1)\sqrt{\omega_1} & -\omega_1^2 C(\omega_1) & -\omega_1^2 C(\omega_1)/\sqrt{\omega_1} \\ \vdots & \vdots & \vdots & \vdots \\ G(\omega_N) & G(\omega_N)\sqrt{\omega_N} & -\omega_N^2 C(\omega_N) & -\omega_N^2 C(\omega_N)/\sqrt{\omega_N} \\ \omega_1 C(\omega_1) & \omega_1 C(\omega_1)\sqrt{\omega_1} & \omega_1 G(\omega_1) & \omega_1 G(\omega_1)/\sqrt{\omega_1} \\ \vdots & \vdots & \vdots & \vdots \\ \omega_N C(\omega_N) & \omega_N C(\omega_N)\sqrt{\omega_N} & \omega_N G(\omega_N) & \omega_N G(\omega_N)/\sqrt{\omega_N} \end{bmatrix} \cdot \begin{bmatrix} R_0 \\ R_1 \\ L_0 \\ L_1 \end{bmatrix} = \begin{bmatrix} \alpha^2(\omega_1) - \beta^2(\omega_1) \\ \vdots \\ \alpha^2(\omega_N) - \beta^2(\omega_N) \\ 2\alpha(\omega_1)\beta(\omega_1) \\ \vdots \\ 2\alpha(\omega_N)\beta(\omega_N) \end{bmatrix}$$

where ω_i, $i = 1, \dots, N$ are the angular frequencies of interest, $G(\omega_i)$ and $C(\omega_i)$ are computed with Equations (**2.4**) and (**2.5**) respectively, and $\alpha(\omega_i)$ and $\beta(\omega_i)$ are the real and imaginary part of the propagation function of the transmission line measured using the SFWR technique. The $N = 80$ frequencies are linearly spaced in the interval 1–80 MHz, in order to span the entire bandwidth of the stimulus signal. The parameters estimated through the OLS problem are reported in **Table 2.1**.

Table 2.1: Estimates of the parameters of $R(\omega)$ and $L(\omega)$ models

R_0 ($\Omega\,\mathrm{m}^{-1}$)	R_1 ($\Omega\,\mathrm{m}^{-1}\,\mathrm{Hz}^{-0.5}$)	L_0 ($\mathrm{H\,m}^{-1}$)	R_1 ($\mathrm{H\,m}^{-1}\,\mathrm{Hz}^{0.5}$)
0.022	6.7×10^{-5}	2.3×10^{-7}	7.5×10^{-5}

As can be seen in **Figure 2.6**, the real part of the propagation function is approximated much better by the model that includes the calibrated primary parameters.

As expected, the simulator produces much more accurate results when the calibrated primary parameters are used. As an example, the same configuration of **Figure 2.5** is simulated using the calibrated parameters. The result of the simulation is presented in **Figure 2.7**. As can be seen, there is a much better fitting between the measured signal and the simulated one. The global root-mean-squared error (RMSE) for all the experiments described in **Section 2.3.2** is 0.098 V using

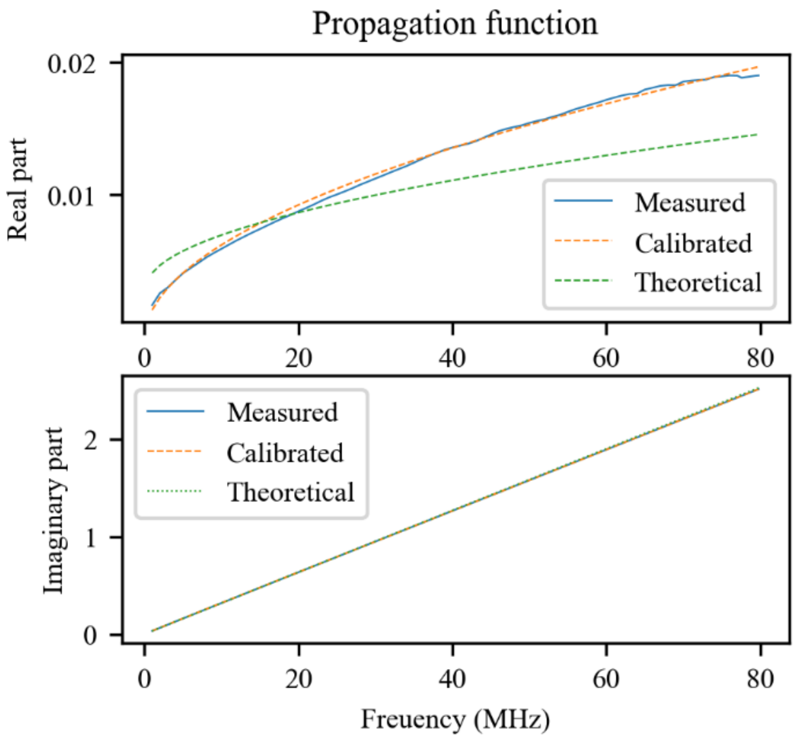

Figure 2.6: Comparison between the measured propagation function of the transmission line, the theoretical one, and that resulting from the calibration process.

the theoretical model, while it is 0.044 V using the calibrated model. Therefore, the RMSE is more than halved owing to the calibration process.

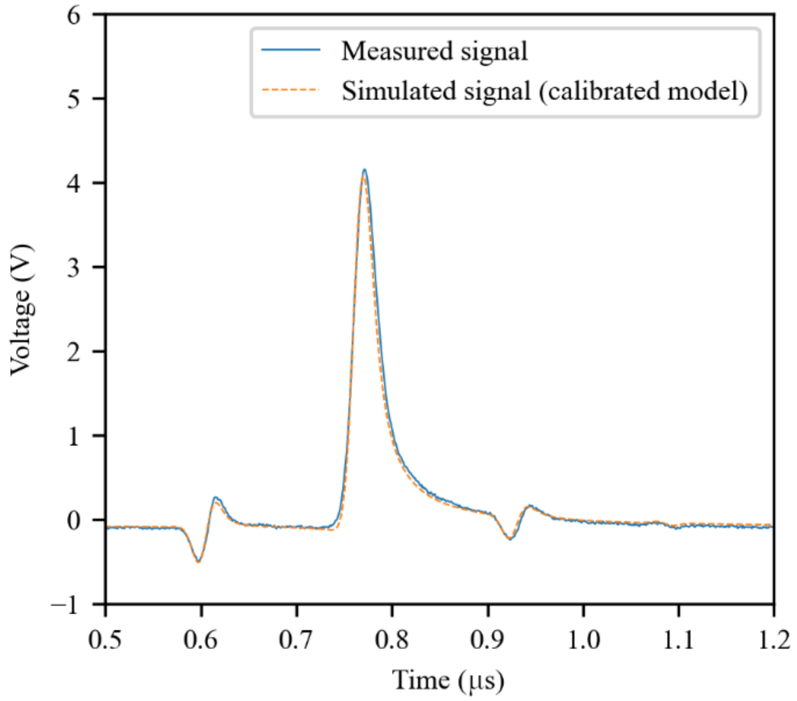

Figure 2.7: Simulation obtained using the calibrated model for the same configuration of **Figure 2.5**.

Dataset generation

The dataset for training the neural network is therefore generated using the calibrated RG58-CU cable model. Simulations are carried out using the setup described in **Section 2.2**, considering the constraints reported in **Table 2.2** to randomly generate the circuital configuration of each sample.

Table 2.2: Parameters of the simulated transmission lines

	Number of faults N_F	Distance between discontinuity points (m)	Total length of the cable (m)	Capacity of the faults (pF)
Min	0	10	10	50
Max	4	–	200	500

A total of 10^6 samples are generated. After simulations, the TDR signals are processed to remove the transmitted pulse, which did not provide any information given that the signals are time aligned, and to add Gaussian noise. Labels for all the samples are defined in compliance with the format of the neural network's output. The range of lengths that contained discontinuity points (faults and line terminations) is divided into $S = 32$ cells, and the positions of the discontinuity points z_i are normalized relative to the range of lengths of the corresponding cells, obtaining values $0 \leq z_i^{'} < 1$. For each sample, an array p of length S is defined whose elements are 1 if the corresponding cell contained a discontinuity point and 0 otherwise. The class of each discontinuity point (fault or line termination) is specified through a $S \times 2$ matrix that had elements $c_{m,n} = 1$ for m corresponding to cells containing a discontinuity point and n corresponding to the class of the discontinuity point (1 for faults, 2 for line termination) and 0 otherwise. Finally, the capacities associated with the faults, C_i, are normalized relative to the range reported in **Table 2.2**, computing the values $C_i^{'}$.

Training of the neural network

The CNN described in **Section 2.2** has been implemented in Python, using the TensorFlow library. In total, 80% of the samples of the dataset are used for neural network training, while the remaining 20% are used for validation. In the training procedure, the following multi-objective loss function is minimized:

$$\begin{aligned}
L =& \alpha_1 \frac{1}{N_f + 1} \sum_{n=1}^{S} p_n (\hat{z}_n^{'} - z_n^{'})^2 + \frac{1}{2(N_f + 1)} \sum_{m=1}^{2} \sum_{n=1}^{S} p_n (\hat{c}_{m,n}^{'} - c_{m,n}^{'})^2 \\
&+ \alpha_2 \frac{1}{N_f} \sum_{n=1}^{S} p_n c_{1,n} (\hat{C}_n^{'} - C_n^{'})^2 + \frac{1}{N_f + 1} \sum_{n=1}^{S} p_n (\hat{p}_n^{'} - p_n^{'})^2 \\
&+ \frac{1}{S - (N_f + 1)} \sum_{n=1}^{S} (1 - p_n)(\hat{p}_n^{'} - p_n^{'})^2
\end{aligned} \tag{2.9}$$

where the estimates produced by the neural network are marked with a hat. The parameters $\alpha_1 = 50$ and $\alpha_2 = 100$ are introduced as a result of a tuning procedure that involved the maximization of the performances of the neural network on the validation dataset.

The neural network model is trained for 300 epochs using the Adam optimizer **[72]**. The learning rate is varied according to exponential decay, updating its value at the end of each epoch so that it halved every 200 epochs.

The weights of the neural network model after the training procedure, as well as the training and validation datasets of simulated signals and the test dataset of experimental signals presented in **Section 2.3.2**, are available in **[73]**.

2.3 Results and discussion

The performances of the CNN are assessed considering both simulated and experimental signals. The threshold for the probability score of predictions is set to half the range (0.5). A discontinuity point prediction is considered correct if a discontinuity point of the same class is present in the label at distance less than the length of a cell. A reflectometry signal is therefore considered correctly analyzed if all the faults are detected without any false positive.

2.3.1 Performance assessment on the validation dataset

The performance of the neural network is first assessed using the validation dataset that is composed of 2×10^5 samples. The outputs produced by the neural network are compared with the corresponding labels. Overall, 99.87% of simulated cables are correctly assessed, meaning that all the faults are correctly identified, and there are no false positives. Estimation errors for the correctly detected discontinuity points are computed and are summarized in **Table 2.3**. The RMSE in the estimation of discontinuity points (both faults and line terminations) is below 10 cm, leading to a mean absolute percentage error (MAPE) lower than 0.1%. The MAPE in the capacity estimation is below 2% instead.

Table 2.3: Estimation errors obtained for the validation dataset

Cable length error		Fault position error		Fault capacity error	
RMSE (m)	MAPE	RMSE (m)	MAPE	RMSE (pF)	MAPE
0.070	0.059%	0.066	0.091%	11	1.2%

2.3.2 Performance assessment on the test dataset (experimental data)

The same kind of assessment is performed considering experimental data. In this case, 100% of the cables are correctly characterized. Estimation results for experiments on cables with one, two, three, and four simulated capacitive faults are reported, respectively, in **Table 2.4**, **2.5**, **2.6**, **2.7**.

Table 2.4: Estimation results for real cables with one capacitive fault

Postion of the fault (m)		Capacity of the fault (pF)		Length of the cable (m)	
Nominal	Estimated	Nominal	Estimated	Nominal	Estimated
50	49.94	107	112	65	65.00
50	49.92	152	158	65	65.01
50	49.97	217	205	65	64.92
50	49.92	309	310	65	64.95
50	49.96	404	434	65	65.01
50	49.99	450	450	65	64.96

Table 2.5: Estimation results for real cables with two capacitive faults

Postion of fault 1 (m)		Capacity of fault 1 (pF)		Postion of fault 2 (m)		Capacity of fault 2 (PF)		Length of the cable (m)	
Nom.	Est.	Nom.	Est.	Nom.	Est.	Nom.	Est.	Nom.	Est.
15	15.04	107	112	65	65.10	152	156	81	81.05
15	15.04	107	113	65	65.21	217	206	81	80.97
15	15.05	107	112	65	65.18	450	451	81	80.80
15	15.13	217	206	65	65.03	309	309	81	80.83
15	15.12	217	206	65	65.02	404	433	81	80.84
15	15.14	450	459	65	65.14	404	430	81	80.69

Table 2.6: Estimation results for real cables with three capacitive fault

	Experiment 1		Experiment 2	
	Nominal	Estimated	Nominal	Estimated
Length of the Cable (m)	131	130.99	131	130.93
Position of Fault 1 (m)	50	49.90	50	49.93
Position of Fault 2 (m)	65	65.06	65	64.99
Position of Fault 3 (m)	115	115.09	115	114.92
Capacity of Fault 1 (pF)	107	115	217	214
Capacity of Fault 2 (pF)	217	210	450	454
Capacity of Fault 3 (pF)	404	431	404	418

Table 2.7: Estimation results for real cables with four capacitive fault

	Experiment 1		Experiment 2	
	Nominal	Estimated	Nominal	Estimated
Length of the Cable (m)	143	142.96	143	142.96
Position of Fault 1 (m)	50	49.87	50	49.88
Position of Fault 2 (m)	65	65.12	65	65.03
Position of Fault 3 (m)	115	114.93	115	114.95
Position of Fault 4 (m)	131	131.40	131	131.32
Capacity of Fault 1 (pF)	107	117	107	115
Capacity of Fault 2 (pF)	217	214	152	165
Capacity of Fault 3 (pF)	404	436	309	323
Capacity of Fault 4 (pF)	450	441	450	439

The results of the statistical analysis of the estimation errors obtained for all the experiments are reported in **Table 2.8**. The errors obtained for experiments are slightly greater than those obtained for the validation simulated samples; however, good accuracy is obtained in both position and capacity estimation.

Table 2.8: Estimation errors obtained for the validation dataset

Cable length error		Fault position error		Fault capacity error	
RMSE (m)	MAPE	RMSE (m)	MAPE	RMSE (pF)	MAPE
0.12	0.10%	0.13	0.22%	14	4.3%

2.4 Conclusions

In this chapter, a method to detect and characterize impedance discontinuity points in cables is presented. The method, based on the use of TDR and CNNs, is characterized for the case of capacitive faults in coaxial cables, but it can be used in any situation where localized impedance discontinuity points are present. In fact, only retraining the neural network with an appropriate synthetic dataset of labeled reflectometry signals would be required for it to work in a different condition, without any time consuming experimental campaign. Typical applications for the proposed method are the localization and characterization of multiple discontinuity points in a distributed sensing element, e.g., faults in cables, leaks in pipelines, damages in concrete structures. The metrological characterization of the method, carried out by analyzing the estimation errors for both simulated and actual experimental signals, proves that it can localize the discontinuity points with great accuracy.

Chapter 3

Accurate detection and localization of water pipe leaks through model-based TDR inversion[1]

3.1 Introduction

Pipelines leakage is a significant problem in public water supply industry. According to EurEau (European Federation of National Associations of Water Services) the mean leakage rate of drinking water distribution networks throughout Europe is about 25% of all water provided **[75]**. This means that approximately $2700\,\mathrm{m}^3$ of water are wasted yearly per km of pipe. Financial losses for suppliers are the most direct consequences of water waste due to leaks, but this problem has environmental and social consequences too. Leaks can indeed exacerbate the water scarcity issue, which is affecting a growing number of people and bigger areas of Europe, also as a result of climate change **[76]**. For these reasons, the problem of water leakages has been addressed by a recent EU Directive **[77]**, which states that water leakage levels should be monitored and reduced. Reliable and accurate methods for locating leaks in pipes are therefore of great interest nowadays.

Many different approaches have been proposed and developed over the years for leak detection in water pipes **[78]**. The most direct method is that based on

---

[1] This Chapter is based on the paper **[74]**

visual inspection which relies on the usage of endoscopes or robots equipped with cameras that are guided inside pipes. This is a very simple method, but it requires a huge human intervention and long times for data analysis. Electromagnetic (EM) inspection methods are also used for status assessment of metallic pipes. These techniques evaluate the metal conditions based on the interaction between transmitted EM signals and the metallic pipes. Acoustic and ultrasonic leak detection techniques are, however, the most used today **[79]**.

Despite the mentioned methods are widely used, their effectiveness depends on the kind of material and geometry of pipes, on the working conditions of the water distribution network (e.g., water pressure) and on the environmental conditions. Furthermore, expert personnel are usually required for measurement operations and for the interpretation of results. In recent years, alternative approaches based on the use of the TDR technique have been proposed **[14], [80], [81]**. These methods exploit EM waves propagating in a distributed sensing element (SE) placed near the pipe to detect and localize water leaks. TDR-based methods have the advantage of not imposing requirements on the characteristics of the pipes, such as their construction material or their operating conditions. This also leads to greater ease of use and more solid results.

In this chapter, a novel method for the analysis of TDR signals for water leak localization in pipes is proposed. TDR measurements are carried out using a bi-wire SE placed along the pipe. The electrical behavior of whole system is then modeled through a circuital representation which produces a simulated TDR signal as output. The parameters of the model are therefore optimized so that the simulated signal fits the measured one. It must be noted that, a “gray-box” model of the whole electromagnetic system is developed, which is composed of the TDR appliance, the mismatched connections, the wires, the surrounding soil and rocks, etc. In this way, a much simpler and computationally tractable problem with respect to an accurate EM modeling is obtained. The proposed model is nevertheless capable to reproduce the measured reflectograms with good accuracy and the final result is an accurate estimation of the position and extension of water leaks.

3.2 Materials and methods

3.2.1 TDR for the detection of leaks in water pipes

The basic conceptual scheme of the on-field measurement setup for TDR-based leak localization in underground water pipes is represented in **Figure 3.1**. A SE is placed along the water pipe. The SE is a TL e.g., a bi-wire cable, whose primary parameters are sensitive to the variations of the dielectric constant of the medium surrounding it. The insulator of the SE is the dielectric medium directly in contact with the conductors of the TL, but the material in which the pipe is buried also affects the properties of the TL in a significant way. The presence of water leaking from the pipe can therefore be detected by using TDR technique, as a local reflection caused by the water leaking into the medium surrounding the SE.

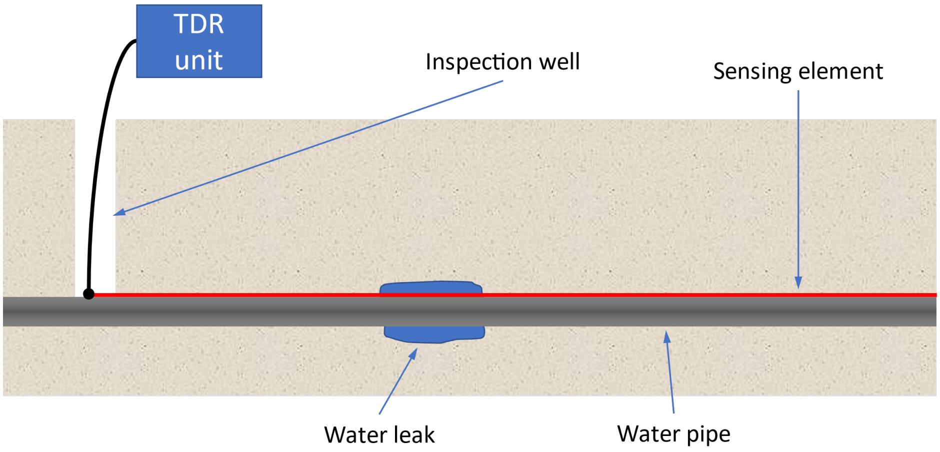

Figure 3.1: Representation of the on-field measurement setup for the TDR-based leak localization in underground pipes. The sensing element SE is placed in the ground near the water pipe and is connected to a TDR unit through a short coaxial cable.

TDR can be implemented using dedicated commercial devices or generic instruments such as waveform generators and oscilloscopes to generate the reference transmitted signal and to acquire the reflectogram, respectively. Measurement devices are usually not directly connected to the SE for practical reasons and hence a coaxial cable can be inserted between the instruments and the SE. A signal obtained in typical situations using the described measurement setup is depicted in

Figure 3.2. In this case, a voltage pulse is transmitted to the SE and is reflected back at different points. The first significant reflection occurs at the interface between the coaxial cable and SE and is due to the different characteristic impedance of the two TLs. Reflection at the water leak is also visible, but its amplitude is comparable to other small reflections due to non-idealities of the TL and the inhomogeneity of the medium around the SE. The reflection at the SE termination is then visible.

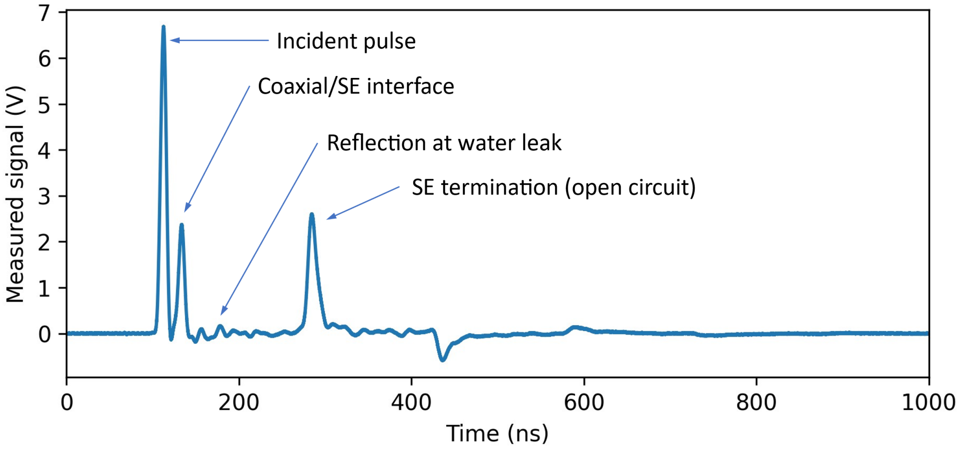

Figure 3.2: Typical reflectogram associated to the on-field measurement setup schematized in **Figure 3.1**.

3.2.2 Laboratory experimental setup

For the purpose of the present work an “ad-hoc” laboratory has been specifically implemented as described in **Figure 3.3**. More specifically, the TDR is performed using an Agilent 33250A AWG for the stimulus signal and a LeCroy Waverunner-2 LT262 oscilloscope for signal acquisition. The AWG and the SE are connected to the oscilloscope through a T-junction and short RG58-CU coaxial cables. The SE is a bi-wire cable having the cross-section depicted in Figure 3. The two conductors of the SE are composed of 24 copper-clad aluminum wires and are coated with PVC. It is worth saying that, in view of the practical on-field application, the afore-described laboratory setup can be equivalently substituted by a more compact and portable equipment.

Water leaks are simulated by placing a water container on the SE or by submerging the SE in water. In the former case, a much weaker discontinuity is obtained because the SE and water are separated by the bottom of the container, which is few millimeters thick.

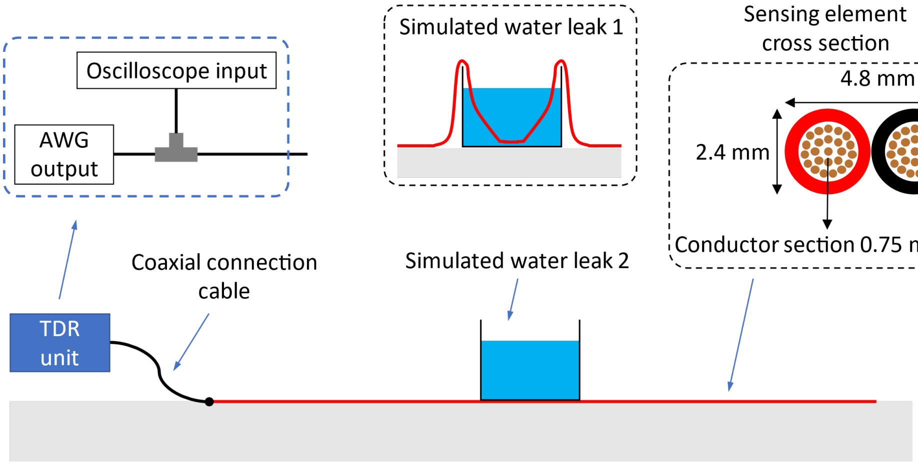

Figure 3.3: Representation of the laboratory measurement setup. The sensing element (SE) is placed on the floor and is connected to the TDR unit through a short coaxial cable.

The measured signals are depicted in **Figure 3.4**. The first signal is acquired in normal conditions, without water leaks. The second signal is acquired while a short portion of the cable is submerged in a water container of length 33.5 cm. In this case, a great reflected pulse is observed in the measured signal (highlighted by a red box in **Figure 3.4**). The third signal is instead acquired with the water container on the cable. Due to the distance between the SE and water, the parameters of the TL are less influenced and hence a smaller reflection is produced. The last signal is also acquired with a water container on the SE but, in this case, the container is 2 m long.

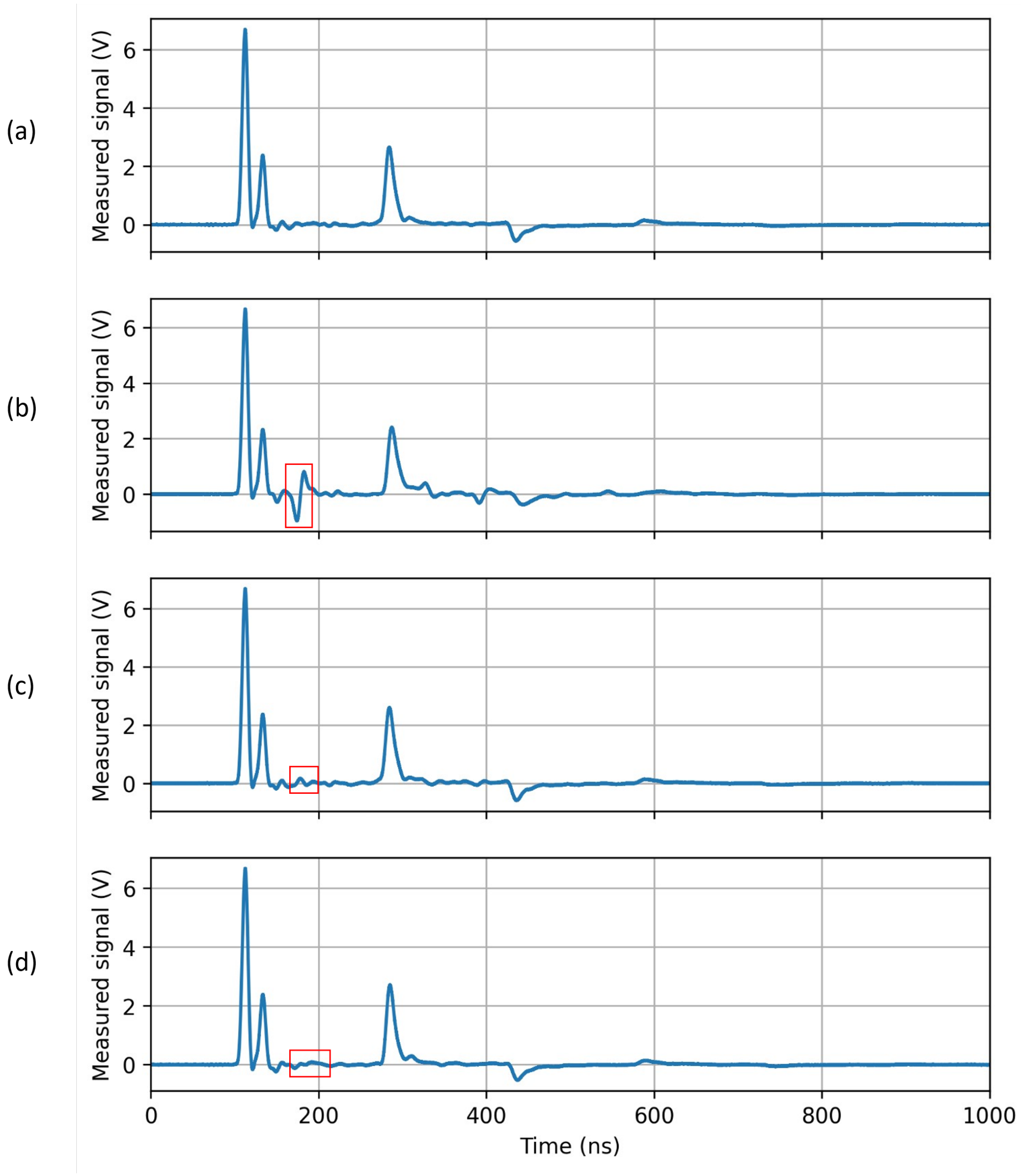

Figure 3.4: Examples of measured signals, SE length: 15 m. The following conditions are considered: (a) SE in the absence of water; (b) high water quantity at 4 m, concentrated in 33.5 cm; (c) moderate water quantity at 4 m, concentrated in 33.5 cm; (d) high water quantity at 4 m, distributed over 2 m. Reflected pulses corresponding to water leak conditions are marked with red boxes.

3.2.3 Problem modeling and simulation

The problem we want to solve is to identify the water leak, in terms of position, extension and magnitude. This is generally a complex task considering that it is not possible to know with enough accuracy the parameters of the SE in on-field measurements. These parameters are indeed very sensitive to the properties of the medium in which the SE is placed, and to geometric deformations of the SE. Therefore, these generally vary with the position along the SE and cause reflections that can hide those generated by water leaks, as shown in **Figure 3.4** (c). Estimating the on-field SE parameters profile along its length is therefore needed to carry out water leak measurements.

A simulation-based optimization approach is here proposed for the estimation of the distributed SE parameters. Contributions from different sources to the profile of these parameters are then identified, and hence water leaks are detected and characterized. The measurement system, composed of the TDR unit, the connection cable, and the SE, is modeled using the well-known TL theory. Simulations are then carried out using a previously developed simulator **[43]** to obtain reflectograms. The parameters involved in the simulation are optimized to minimize an objective function given by the RMSE between the measured reflectogram and the simulated reflectogram. Given the complexity of the problem and the large dimensionality of the parameters vector, a random search method with adaptive step size is effectively used for the optimization **[82]**.

The model of the system used in simulations is represented in **Figure 3.5**. The connection coaxial cable and the SE are modeled as TLs, terminated on the load Z_L. The TLs are composed of N_C and N_{SE} cells of length dz, respectively. The total lengths of the cables are therefore, respectively,

$$l_c = N_c dz \tag{3.1}$$

$$l_{SE} = N_{SE} dz \tag{3.2}$$

The following six-parameter frequency-dependent model is used for the primary parameters of both the TL:

$$R(\omega) = R_0 + R_1\sqrt{\omega} \tag{3.3}$$

$$L(\omega) = L_0 + L_1/\sqrt{\omega} \tag{3.4}$$

$$G(\omega) = G_0\omega \tag{3.5}$$

$$C = C_0 \tag{3.6}$$

where ω is the angular frequency and R_0, R_1, L_0, L_1, G_0, C_0 are adjustable parameters. The frequency-dependance of the model is derived from the dielectric dispersion and the skin effect phenomena. The distributed capacitance of the SE C_{SE}, which is the parameter of interest in the analysis, is modeled as position dependent. This parameter is indeed influenced by the dielectric constant of the medium around the SE. The capacitance of the generic cell n is therefore multiplied by the parameter p_n, as shown in the diagram of **Figure 3.5**.

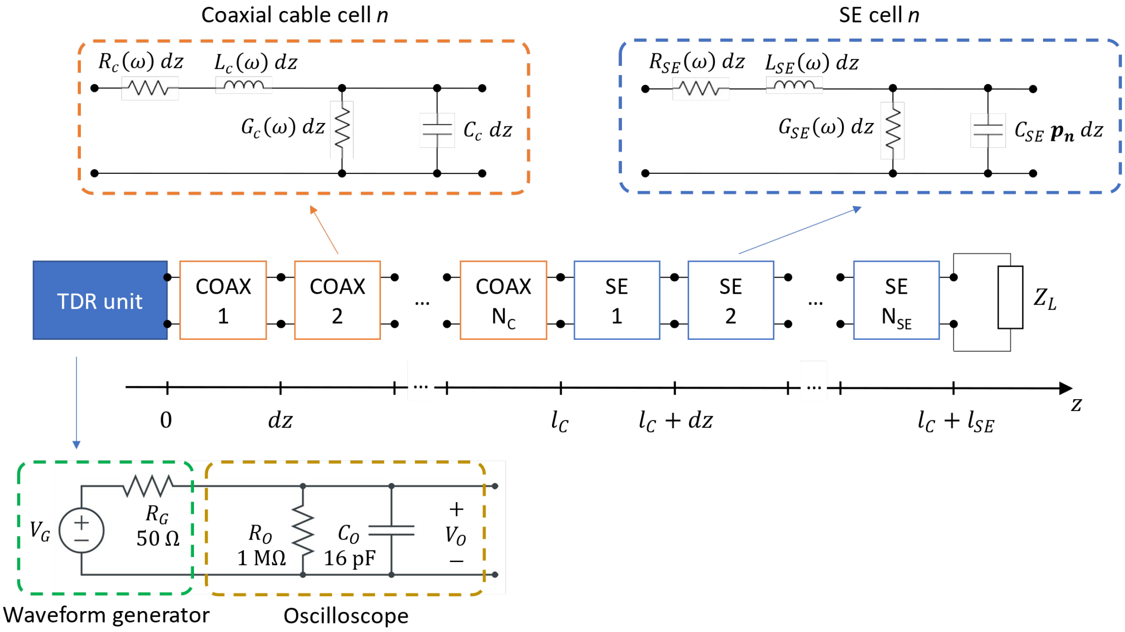

Figure 3.5: Model of the measurement system used in simulations.

Before each simulation, the cell length is chosen so that its value is much smaller than the minimum wavelength propagating in the cables:

$$\begin{aligned} &dz = \lambda_{min}/\alpha, \\ &\lambda_{min} = \min\left\{ \min_{f\in[0,f_{max}]} \frac{1}{f\sqrt{L_C(f)C_C}}, \min_{f\in[0,f_{max}],z} \frac{1}{f\sqrt{L_{SE}(f)C_{SE}(z)}} \right\} \end{aligned} \tag{3.7}$$

where f_{max} is the maximum analyzed frequency and α is a tunable parameter which must be chose meeting the constraint $\alpha >= 10$ **[43]**. The value of α determines the density of the TL model (i.e., the number of cells), and hence the accuracy in the approximation of the actual system. The value $\alpha = 20$ has been used in this work since greater values lead to negligible improvements. The number of cells of both the TLs is therefore recomputed according to equations (**3.7**), (**3.1**) and (**3.2**) at the beginning of the simulation. Finally, the termination impedance is modeled as a capacitance, in order to consider the fringing capacitance at the end of the SE. This model leads to better simulation results with respect to an ideal infinite impedance, which systematically cause the presence of a peak in the final part of p_n.

All the parameters of the model can be involved in the optimization process. Some of them, however, can be fixed since they can be accurately known in advance e.g., the length of the connection coaxial cable and the circuital model of the instruments composing the TDR unit (depicted in **Figure 3.5**). The number of parameters of the position-dependent capacitance profile p_n is instead reduced since the number of cells of the SE in the model is generally very high. The profile can be represented using e.g., a multi-sine signal. The capacitance profile p_n is the quantity of interest in our analysis since it yields information about the presence of water. All the other parameters of the model must be estimated, however, to properly fit the measured reflectograms. Nevertheless, some of them can be measured in preliminary calibration analysis and then kept fixed during the water leaks estimation process.

The proposed circuital model is only an approximation and cannot provide a detailed representation of the electromagnetic behavior of the system as a full-wave simulation could. The model, however, can produce reflectograms that fit on-field measured ones with good accuracy. Moreover, it is much simpler and cost-effective than full-EM models and can therefore be effectively integrated in simulation-based optimization routines.

3.2.4 Water leaks detection

Water leaks can be directly detected by localizing peaks in the estimated capacitance profile p_n. In simulations, the capacitance profile is modeled with a series of evenly spaced Gaussian pulses having standard deviation equal to the distance between the peaks of two consecutive pulses. The parameters of the model are therefore the amplitudes of the pulses. This model is more effective than e.g., a multi-sine signal, for the optimization process because each parameter influences a limited region of the signal. The complete of adjustable parameters is listed in the following.

- Primary parameters of the coaxial cable: $R_{0,c}$, $R_{1,c}$, $L_{0,c}$, $L_{1,c}$, $G_{0,c}$, $C_{0,c}$
- Primary parameters of the SE: $R_{0,SE}$, $R_{1,SE}$, $L_{0,SE}$, $L_{1,SE}$, $G_{0,SE}$, $C_{0,SE}$ Length of the SE: l_{SE}
- Amplitude of the Gaussian pulses composing the capacitance profile p_n (a vector of 100 parameters)
- Termination capacitance C_L

When reflections due to the presence of water are weak, like in the situations showed in **Figure 3.4** (c) and in **Figure 3.4** (d), the estimated profile does not provide a solid identification of leaks. In these cases, a signal measured with the same setup but without water (**Figure 3.4** (a)) can be exploited to improve the estimation results. A first optimization is performed on the signal measured in the absence of water. This is a calibration step for the system and all the estimated parameters of the model in **Figure 3.5** are assumed as a constant base for the following analysis, in which only the parameters of an additional capacitance profile are optimized. In particular, the additional profile associated to a water leak is modeled as a function of the form:

$$p_{leak}(z) = k \cdot \beta\left(\frac{z - z_0}{w}, \alpha, \alpha\right) \tag{3.8}$$

where $\beta(x, a, b)$ is the beta probability density function computed in x with form parameters a and b. In this way, p_{leak} is non-zero in the interval $[z_0, z_0{+}w]$ (it begins at z_0 and has a width w), k is a magnitude factor, and α is a form factor. Depending on the value of α, model (**3.8**) assumes different shapes, from a rectangular pulse to a bell-shaped pulse, as depicted in **Figure 3.6**. The total multiplicative profile of the model in **Figure 3.5** is therefore given by

$$p(z) = p_{cal}(z) + p_{leak}(z) \tag{3.9}$$

where $p_{cal}(z)$ is the profile estimated in the calibration phase. In the water leak detection phase, instead, only the four parameters of the additional profile are estimated.

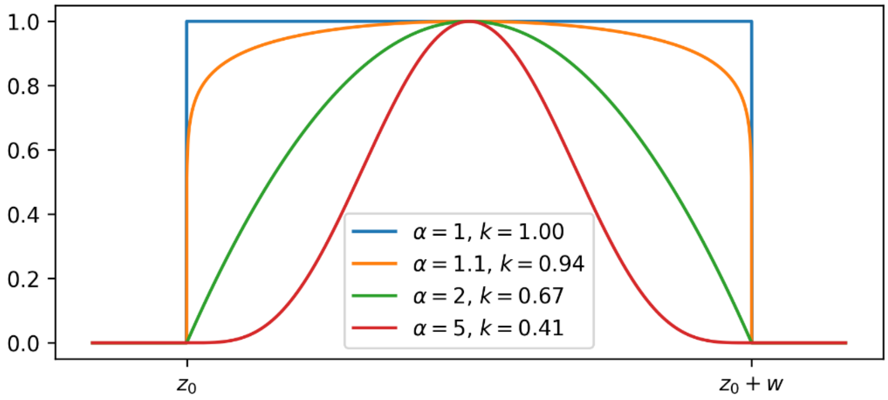

Figure 3.6: Examples of profiles p_{leak} obtained using model (**3.8**).

3.3 Results

This Section reports the results obtained with the proposed water leak estimation technique applied to signals measured with the experimental setup described in **Section 3.2.2**. Furthermore, some preliminary results about a more general TDR inversion are also reported. These results are instead obtained with simulated signals.

3.3.1 Direct water leaks detection

The optimization procedure is first used to directly estimate the capacitance profile. When the signal reflected at the water leak is high the region of the SE submerged in water is accurately identified, as shown in **Figure 3.7**.

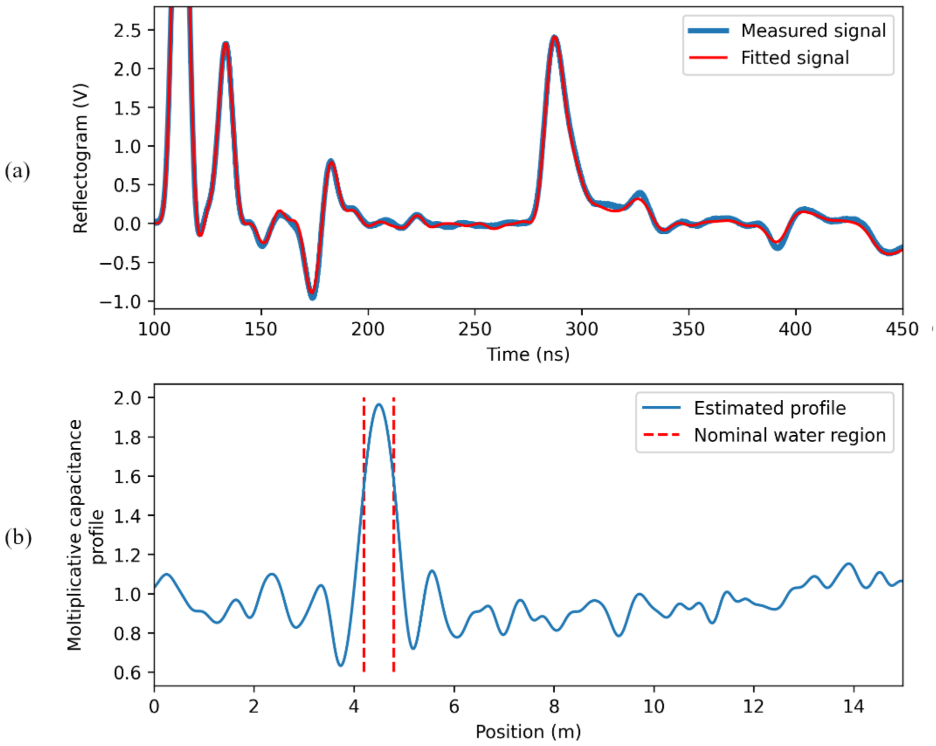

Figure 3.7: Results of the direct water leak estimation in the case of a strong reflected pulse: (a) measured and fitting signal; (b) estimated capacitance profile.

In **Figure 3.8**, the capacitance profile estimation results for the case of a weak reflection are depicted. As can be seen, the water region is still correctly detectable since it corresponds to the highest peak of the estimated profile. However, its magnitude is comparable to that of the fluctuations in the profile due to the non-idealities of the SE. In this case, a calibration phase, preceding the water leaks detection, improves the estimation results, as shown in next section.

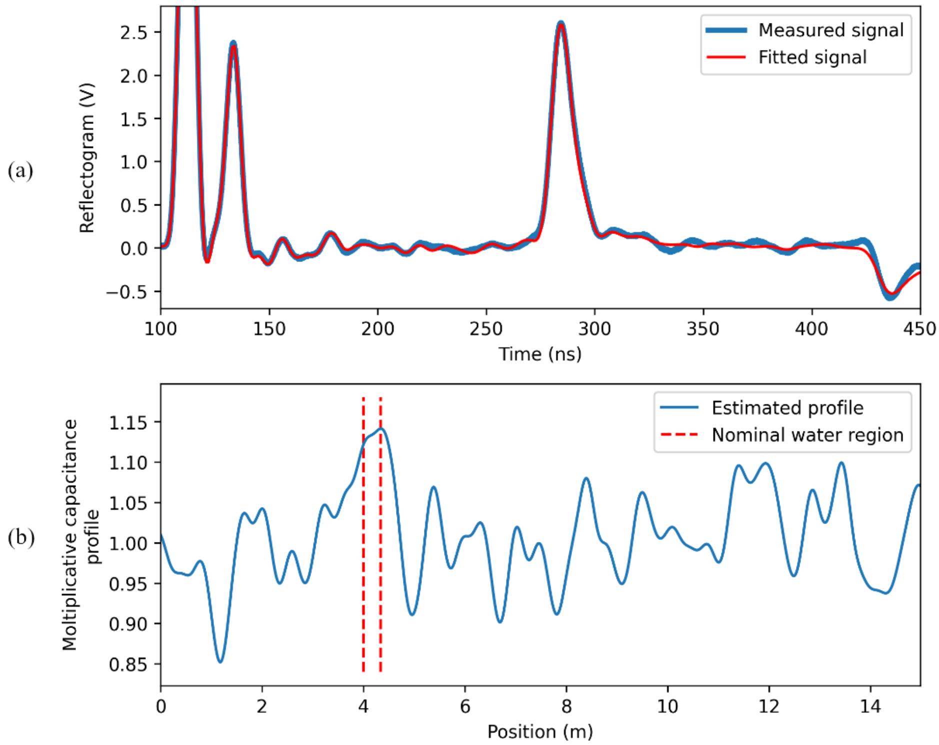

Figure 3.8: Results of the direct water leak estimation in the case of a weak reflected pulse: (a) measured and fitting signal; (b) estimated capacitance profile.

3.3.2 Water leaks detection after calibration

A second approach for water leaks detection is based on the use of a calibrated model as a base for simulations carried out to fit the signals measured in the presence of water. The calibration consists in estimating all the parameters of the model in **Figure 3.5** from a TDR signal measured in the absence of water. In **Figure 3.9** (a), the result of the fitting procedure is depicted, while in **Figure 3.9** (b) the estimated multiplicative capacitance profile is showed. As can be seen, a very good fitting is obtained. The estimated profile, however, does not represent the actual capacitance profile along the SE, but it is one of the profiles that well reproduces the input/output behavior of the system, and this is sufficient for the correct water leak estimation. To accurately estimate the capacitance profile of the cable using the same method, a greater spatial resolution is needed, and hence a shortest transmitted pulse must be used. This has been successfully achieved in preliminary tests, but for the proposed water leak detection application a longer pulse is sufficient, which implies that cost-effective measurement devices can be used.

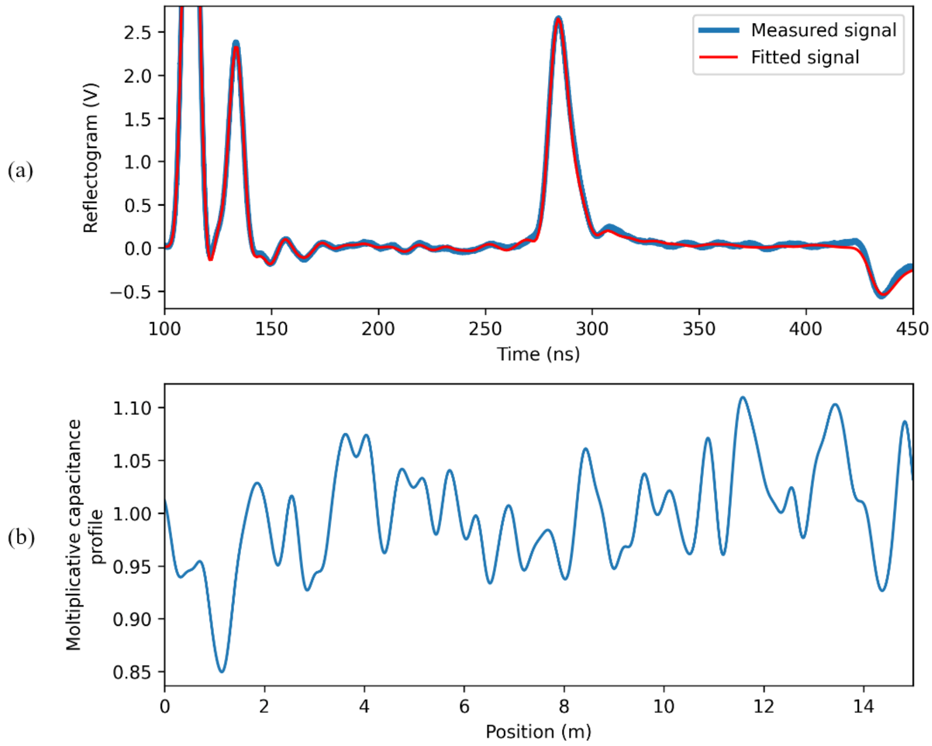

Figure 3.9: Fitting of the measured signal in the absence of water leaks.

High water quantity concentrated in a small region

The same measured signal of **Figure 3.7** is analyzed using the calibration-based water leak identification technique and estimation results are reported in **Figure 3.10**. The estimated center and length of the water region are 4.50 m and 51 cm respectively, while the actual ones are respectively 4.52 m and 46 cm.

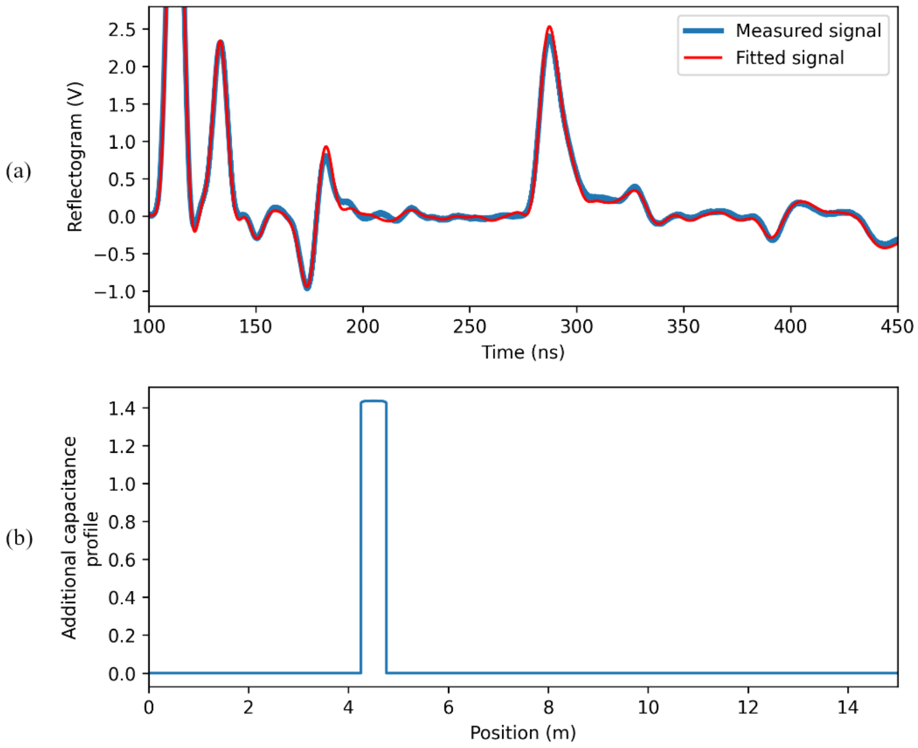

Figure 3.10: Results of the water leak estimation after calibration in the case of a strong reflected pulse: (a) measured and fitting signal; (b) estimated additional capacitance profile.

Moderate water quantity concentrated in a small region

The calibration-based water leak identification is then applied to the signal measured with the 33.5 cm long water container on the SE (the same of **Figure 3.8**). The estimation results are depicted in **Figure 3.11**. In this case, the water region is correctly and accurately identified.

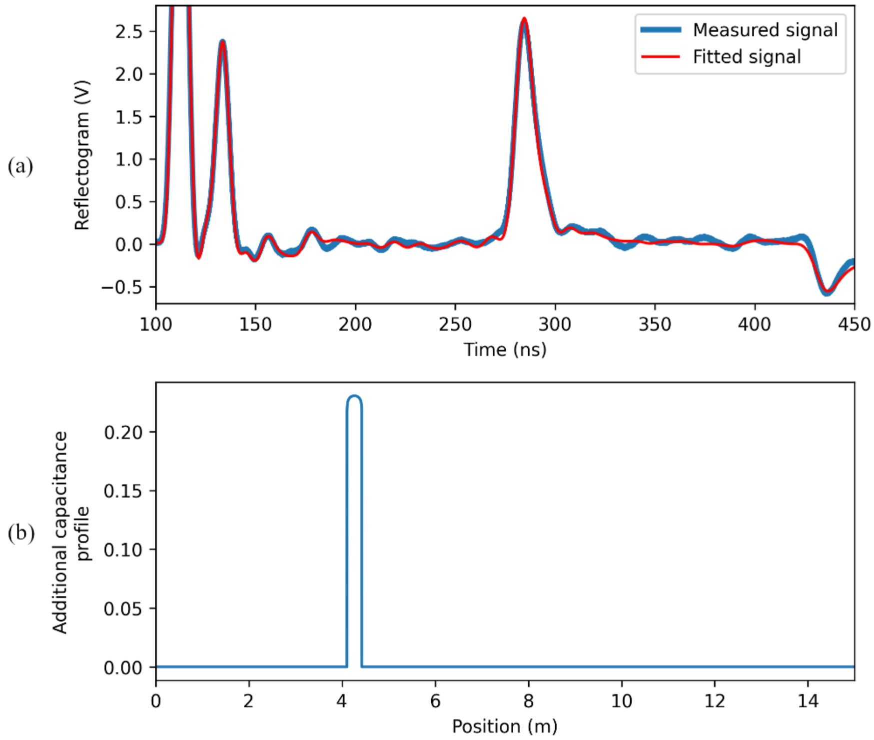

Figure 3.11: Results of the water leak estimation after calibration in the case of a weak reflected pulse: (a) measured and fitting signal; (b) estimated additional capacitance profile.

The same test is also repeated by placing the water leak in other positions, and results are reported in **Table 3.1**. The water leak is correctly localized in each measurement, in the sense that the estimated water region always intersects the actual water region. The standard deviation of the error in the leak center estimation, and in the leak length estimation, are both 13 cm. The total estimated capacitance of the leak, i.e. the area below the estimated additional capacitance profile, is also reported in **Table 3.1**.

Table 3.1: Estimation results for the water leak position and entity estimation in the case of leak length 33.5 cm

Nominal center of water leak (m)	Measured center of water leak (m)	Measured length of water leak (m)	Measured total capacity (% of first measurement)
2	1.97	33.2	-
4	4.11	21.6	64.40
6	6.02	30.4	109.63
8	8.14	19.8	77.54
10	10.41	62.2	136.93
12	12.25	22.0	109.95
14	14.14	37.5	117.07

Distributed high water quantity

Water leak detection is then carried out for 2 m long simulated leaks, and estimation results are reported in **Table 3.2**. In this case, too, water leaks are correctly localized in each measurement (estimated and actual water regions always intersect). The standard deviations of the error in the leak center estimation and in the leak length estimation are equal to 33 cm and 43 cm respectively.

Table 3.2: Estimation results for the water leak position and entity estimation in the case of leak length 2 m

Nominal center of water leak (m)	Measured center of water leak (m)	Measured length of water leak (m)	Measured total capacity (% of first measurement)
2	1.64	132.20	-
4	3.59	114.56	86.85
6	6.22	183.06	211.06
8	7.90	241.84	187.61
10	10.60	118.45	121.66
12	12.22	124.75	182.85
14	14.18	147.00	115.07

3.3.3 Direct profile estimation (TDR inversion) on a simulated TL

In this last Section, some preliminary results about a more general TDR inversion problem are reported. The procedure used here for TDR inversion is the same used in **Section 3.3.1**. In this case, however, a simulated TL is considered so that the "true profile" is known. The capacitance profile of the TL used in simulations is indeed that depicted in **Figure 3.12**. This arbitrary profile has been obtained as a multi-sine signal composed of 30 harmonics with random magnitude and phase.

Using a short transmitted pulse as reference signal in TDR measurements, a good fitting of the TL's profile can be achieved using the proposed optimization procedure, as shown in **Figure 3.13** and **3.14**. As can be seen, the estimated profile does not perfectly follow the true profile, especially in the final part, but the obtained result is very promising and, with further refinements, an effective method for TDR inversion can be developed, with applications in both water leak detection systems and other fields.

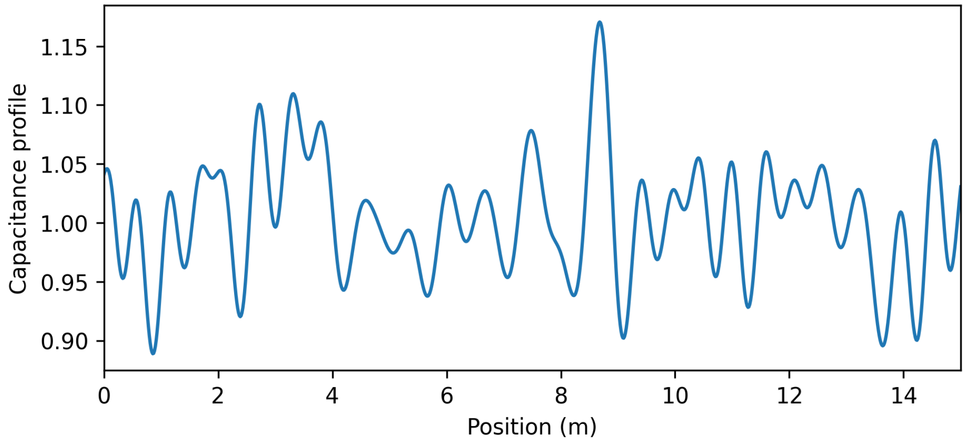

Figure 3.12: Arbitrary capacitance profile used in the simulation. The profile is obtained as a multi-sine signal composed of 30 harmonics with random magnitude and phase.

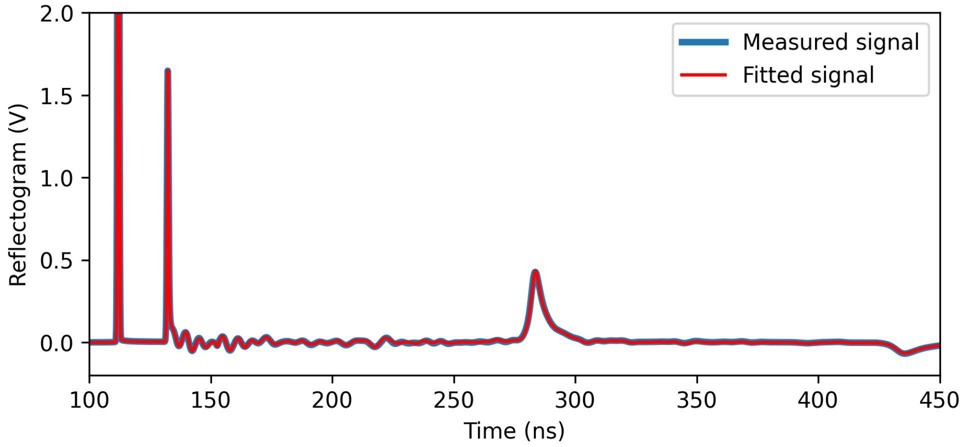

Figure 3.13: Result of the optimization procedure: fitting reflectogram.

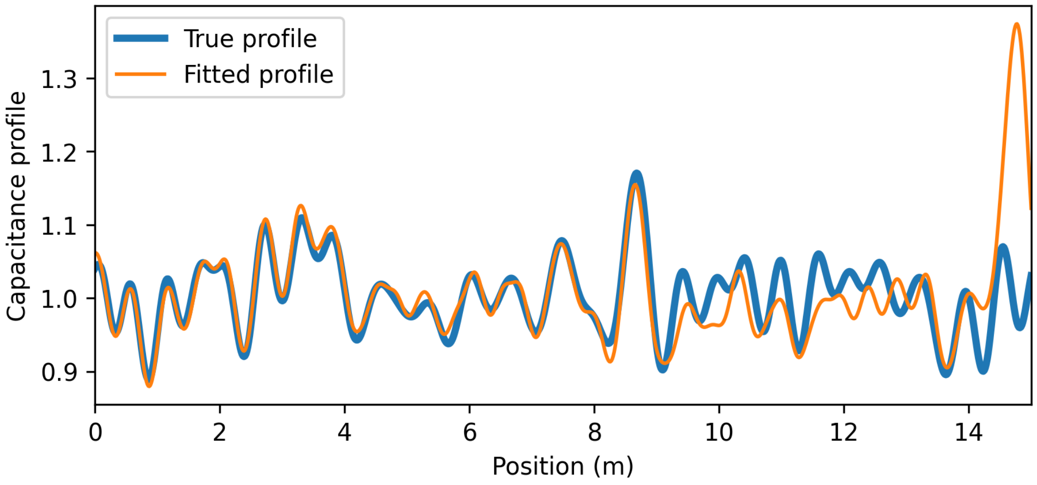

Figure 3.14: Result of the optimization procedure: estimated profile.

3.4 Conclusions

In this Chapter, an enhanced water leak TDR detection system has been described. The system is based on time domain reflectometry performed on a simple bi-wire sensing element. The measured signals are processed using a novel simulation-based optimization algorithm, which can work directly on a single signal in case of strong leaks or exploiting an initial calibration carried out in the absence of water in case of weaker leaks. Experimental results carried out in different conditions show that the method estimates accurately the position and extension of water leaks. The proposed method can therefore be used successfully for monitoring water pipe, and has the potential of being easily employed for other water and moisture monitoring applications, e.g. in precision agriculture.

Chapter 4

Conclusions and future work

In this thesis, innovative signal processing methods for reflectometry measurements have been proposed. The first presented technique is a development of the recently proposed SFWR, which employs sinusoidal bursts as reference signal. Thanks to an accurate theoretical analysis developed in **Chapter 1**, which lays the foundation also for the other successive findings throughout the thesis, the technique is extended to be more general and better exploit the information contained in SFWR signals. Also, an algorithm to effectively analyze overlapping reflected signals is presented.

In **Chapter 2**, deep learning is used for the localization and characterization of multiple faults in cables. A CNN is proposed for this task and very good results are obtained. An important aspect of this work is the development and usage of a synthetic dataset for neural network training. The dataset, publicly available online **[73]**, is composed of a great number of labeled samples which have been created using a TL simulator, avoiding the laborious and time-consuming task of manually collecting and labelling the samples. The neural network trained using the synthetic dataset has then been able to process both simulated and actual measured TDR signals, proving the effectiveness of the proposed methodology. This is a promising result that can lead to future developments of deep learning-based reflectometry techniques and more in general of training strategies for deep learning models.

Finally, the model-based optimization method proposed in **Chapter 3** has been proved to provide accurate estimation results also when the measured signal contains very weak reflected pulses. This situation is typical of water leak detection measurements i.e., the application considered in the Chapter, but it is also often present in any TDR measurement. The result is achieved through the identification of an approximate model of the whole electromagnetic system, composed of the sensing element, the connection cables and the instruments. Although such model is not an accurate representation of the physical model, it is still able to provide accurate estimation results when it comes to water leak detection and characterization. Furthermore, if a short pulse is used as reference signal, a distributed measurement along the whole SE i.e., TDR inversion, can be obtained.

Appendix A

Other applications of signal processing and machine learning techniques in measurement problems

The signal processing and machine learning techniques developed as part of this thesis have also been object of other researches carried out during the Ph.D. program. This Chapter provides a brief overview of these studies, which mainly deal with the processing of information acquired through a great variety of sensors and the metrological characterization of these systems. In **Section A.1**, an algorithm based on traditional signal processing techniques is proposed for the measurement of heartbeat and respiratory intervals from data acquired by a common smartphone's commodity accelerometer. In **Section A.2**, an innovative needle-shape sensor with nanostructured platinum for ion-detection is proposed. In this case, a careful characterization of the sensor production process is carried out with the aim of finding the parameters which optimize the electrochemical performances of the sensor. This work has been performed during a stay at École Polytechnique Fédérale de Lausanne (EPFL) in the period January-April 2022. In **Section A.3**, a deep learning-based computer vision technique for real time intravenous drip infusion monitoring is presented. Finally, **Section A.4** and **A.5** deal with the analysis of satellite images with deep learning models, respectively, for seagrass meadows monitoring and for coastline monitoring.

A.1 Accurate simultaneous measurement of heartbeat and respiratory intervals using a smartphone[1]

In this Section, a method based on the usage of a smartphone for measuring simultaneously both heartbeat intervals and respiratory intervals is presented **[83], [84]**. In particular, the commodity accelerometer of a smartphone is used for measuring the seismocardiographic signal generated by heart activity and the acceleration due to breathing movements. The measurement is performed with the subject laying down, placing the smartphone on his/her xiphoid process. Signal processing algorithms are presented that can accurately estimate heartbeat and respiratory intervals from the measured acceleration signals. A metrological validation of the heartbeat and respiratory intervals estimates obtained with the proposed method is carried out by comparison with measurements obtained using an electrocardiograph and a spirometer.

A.1.1 Measurement setup

The measurements involved in this study are based on recording the mechanical activity of heart and lungs. The two main techniques for monitoring the mechanical activity of heart are Ballistocardiography (BCG) and seismocardiography (SCG) **[85]**, both implementable using an accelerometer. In this work, SCG signal are measured using the accelerometer of a smartphone. The acceleration signal recorded in this way has also been exploited to estimate the respiratory intervals (inhalation and exhalation). The smartphone has been placed on the xiphoid process, with the subject laying down, as depicted in **Figure A.1**. This placement is the most common and convenient, since it guarantees that vibrations due to heart movements can be reliably detected (acceleration along the z axis is used). Besides, this positioning is useful to detect the respiration activity exploiting the variation of the smartphone's inclination in the yz-plane, which follows the inhalation/exhalation cycle (acceleration along the y axis is used).

---

[1] This Section is based on the paper **[83]**

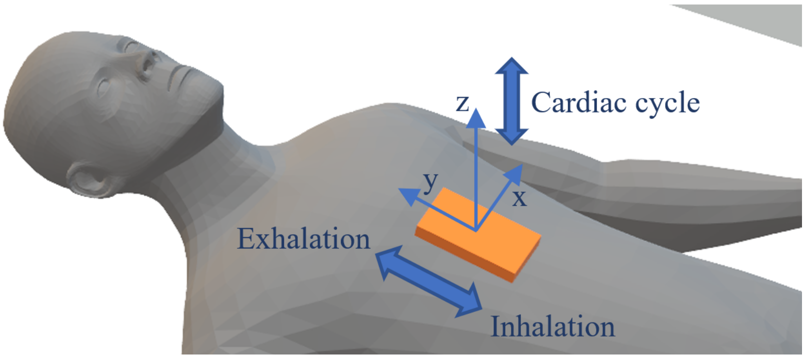

Figure A.1: Representation of the measurement setup. The subject is supine with the smartphone placed on his/her xiphoid process; the orientation of the accelerometer axes is represented.

A.1.2 Signal processing

An algorithm has been developed to automatically find the position of aortic valve opening (AO) peaks in the SCG signal and hence estimate the heartbeat intervals. AO peaks are, indeed, the highest and sharpest peaks in the SCG waveform and AO-AO intervals have been shown to be usable as substitutes of R-R intervals in any practical application. The first operation performed by the algorithm is a high pass filtering of the acceleration signal a_z in which harmonics due to gravity acceleration (DC component) and low frequency noise, including that due to breathing movements, are canceled. A matched filter is then created using heartbeat waveforms selected from the SCG signal and used for filtering the whole signal. In this way, AO peaks are exalted by the filtering operation and can be be easily and accurately detected, as shown in **Figure A.2** (a).

The respiratory intervals are extracted from the y-component of the acceleration signal. In this case, a low pass filtering operation to remove frequency components due to noise and cardiac activity is performed (the opposite of the one performed for the SCG signal). Finally, the first derivative of the filtered signal is computed and inhalation and exhalation phases are discerned using the sign of the derivative. The different stages of the respiratory signal processing are depicted in **Figure A.2** (b).

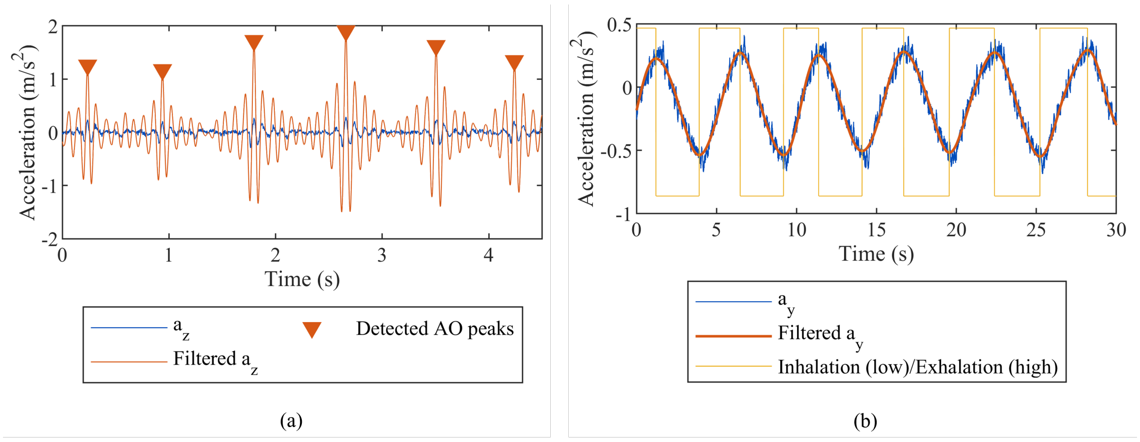

(a)

(b)

Figure A.2: (a) Results of heartbeat signal filtering and peak detection. (b) Respiratory signal filtering and detection of inhalation and exhalation regions.

A.1.3 Results and discussion

The signal processing algorithms presented in the previous Section have been tested on acceleration signals acquired using the measurement setup described in **Section A.1.1** on eight male healthy volunteers (age in range 26-55). During measurement, signals have been acquired also from an ECG device and a spirometer for validation. R-R intervals are computed for each ECG track and compared with the corresponding AO-AO intervals estimated analyzing the SCG signal with the proposed technique. The standard deviation of the error obtained for the heartbeat intervals is 1.9 ms, while the mean error is 0.80 ms. The respiratory intervals measured using the proposed method are instead compared with those obtained from the flow spirometer.Errors in the duration of the respiratory intervals are computed, and the mean and standard deviation of this errors are, respectively, -2.8 ms and 91 ms.

In conclusion, the method is based on the usage of common smartphones, and given its non-invasiveness and simplicity, can be used for self-monitoring applications in everyday life. The results obtained in validation tests proves that the proposed method can be effectively used for the simultaneous measurement of heartbeat and respiratory intervals.

A.2 Platinum nanostructured needle-shaped sensors for ion-detection in biomedical applications[2]

In this Section, an innovative needle-shaped sensor in sub-mm sizes with nanostructured platinum for ion-detection aims is presented **[86]**. Ion-selective electrodes (ISEs) represent one of the main technologies for developing sensors to measure ions concentration in human tissues and all-solid-state ISEs are of key-importance for sensor miniaturization. The developed sensor has been tested for potassium detection, which is very important in cells functions assessment. For the first time in literature, the effects on the morphology of electrodeposition voltage and time are investigated. In past, similar nanofabrications have been successfully tried on usual planar geometries. Here, instead, Pt nanostructures growth is successfully shown on a thin Pt wire with diameter of 0.1 mm only. Both granular and petal-like nanostructures are obtained depending on the applied deposition voltage. The electrochemical measurements performed on the Pt nanostructured K^+ ISEs show enhanced stability over time with respect to non-nanostructured ISEs, and a Nernstian response with best sensitivity of 59.2 ± 2.4 mV/decade in the linear range from 10^{-4} to 10^{-1} M.

A.2.1 Materials and methods

Pt-nanostructures (Pt-NSs) are grown on Pt wires using a one-step template-free electrodeposition procedure. Samples are produced using different configurations, defined by the parameters: applied electrodeposition potential and electrodepotion duration. The obtained samples are then characterized and compared both by morphological point of view and by an electrochemical point of view. The morphology of the obtained Pt-NSs is analyzed using scanning electron microscopy (SEM) images. The type of Pt-NS is first identified (nanopetals and nanospheres are obtained with the considered configurations) and then their sizes are measured using image analysis softwares. The electrochemical characterization is instead carried out by evaluating the performances of the ISEs obtained by

---

[2] This Section is based on the paper **[86]**

coating the nanostructured Pt wires with a K^+ ion selective membrane. The main evaluated parameters are sensitivity, limit of detection (LOD) and stability over time.

A.2.2 Results and discussion

SEM images of the Pt-NSs obtained with some of the considered configurations are reported in **Figure A.3**. The main results deriving from this analysis are the following: *(i)* a granular morphology is obtained when a -0.6 V potential is applied, independently of deposition time; *(ii)* a petal-like morphology is obtained when a -1 V potential is applied, independently of deposition time; *(iii)* when -1 V is applied the Pt surface is fully covered with NPs after at least 400 s electrodeposition time, while when -0.6 V is applied it is fully covered after just 50 s.

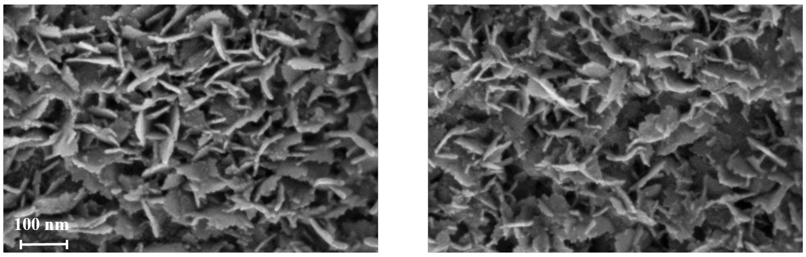

(400 s, -1 V) petal length: 96 ± 24 (600 s, -1 V) petal length: 90 ± 24

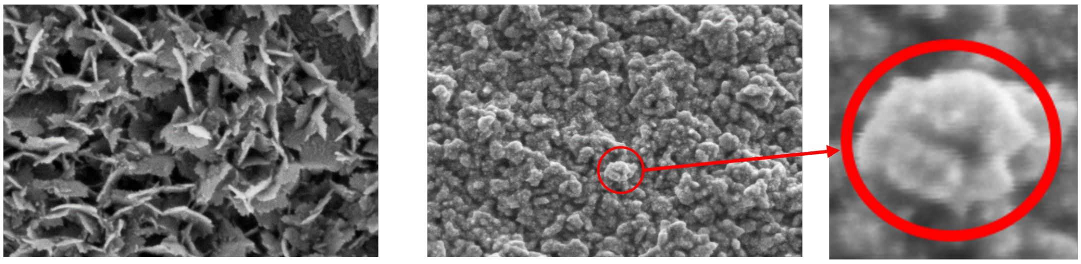

(800 s, -1 V) petal length: 102 ± 28 (200 s, -0.6 V) 43 ± 13 (large spheres) 6.9 ± 1.2 (small spheres) Zoom of a sample large sphere

Figure A.3: High magnification (350k) SEM images of the 400 s, 600 s, and 800 s samples at -1 V deposition voltage, and for the (200 s, -0.6 V) sample. On the bottom right, a zoom of a big sphere of (200 s, -0.6 V) SEM image: several smaller spheres are visible on the surface of the larger one. Nanostructure size is in nm, expressed as mean ± SD.

Results of the electrochemical performances assessment are reported in **Table A.1**. The Pt-NSs ISEs obtained in different configurations are compared with bare Pt ISEs. Sensitivity of nanostructured ISEs is always near the theoretical value of 59 mV/dec and their LOD is at least one decade below the physiological concentration K^+ range, despite the different Pt substrate geometry. Also, Pt-NSs ISEs show better stability over time than bare Pt ISEs.

Table A.1: Statistics of performance parameters of the nanostructured samples for different deposition configurations. Results expressed in mean ± SD.

Configuration	Sensitivity (mV/dec)	LOD ($\log[K^+]$)	Drift after 1 h (mV)	Drift after 14 h (mV)
Bare platinum	36.8 ± 2.0	-4.27 ± 1.15	25.72 ± 0.68	68.7 ± 7.3
-0.6 V, 200 s	59.2 ± 2.4	-4.22 ± 0.33	12.9 ± 9.8	7.9 ± 6.3
-0.6 V, 600 s	55.5 ± 8.6	-4.50 ± 0.53	5.7 ± 5.2	20.4 ± 15.8
-1 V, 400 s	60.7 ± 6.3	-4.31 ± 0.48	12.2 ± 13.3	22 ± 26.3
-1 V, 800 s	54.7 ± 3.1	-4.07 ± 0.05	10.4 ± 10.2	24.4 ± 15.6

Worth to note here also that the distinctive characteristics of the fabricated K^+ sensors are the ease to fabricate and the very small sizes, so they could be easily and effectively integrated into surgical instruments to furnish diagnostics during surgical procedures, or into portable devices for real-time monitoring at the patient's bed.

A.3 Deep learning-based computer vision for real time intravenous drip infusion monitoring[3]

This Section presents an application of deep learning-based computer vision for real-time monitoring of the flow in intravenous (IV) infusions **[37], [38]**. IV infusions are among the most common therapies in hospitalized patients and, given that both over-infusion and under-infusion can cause severe damages, monitoring the flow rate of the fluid being administered to patients is very important for their safety. The proposed system uses a camera to film the IV drip infusion kit and a deep learning-based algorithm to classify acquired frames into two different

---

[3] This Section is based on the paper **[38]**

states: frames with a drop that has just begun to take shape and frames with a well-formed drop. The alternation of these two states is used to count drops and derive a measurement of the flow rate of the drip. The usage of a camera as sensing element makes the proposed system safe in medical environments and easier to be integrated into current health facilities.

A.3.1 Flow rate estimation method

An IV drip infusion kit is composed of a bottle containing the infusion fluid, a drip chamber, and a tube connected to the venous catheter. The proposed system uses a camera to film the drip chamber, as shown schematically in **Figure A.4** (a). The video acquired by the camera is sent to the convolutional neural network depicted in **Figure A.4** (b). The proposed neural network is able to locate the position of the drop and, more importantly, its state, i.e. whether the drop has just begun to take shape, or is instead well-formed. The alternation of these two states can be easily exploited to count drops and, hence, measure a flow rate. It has been decided to use deep learning-based computer vision techniques to process the video acquired by the camera because these videos can have very different features due to e.g. variability of the background texture, of the illumination conditions, of the focus of the camera. This variability make it difficult to use classical image processing techniques because any specific condition must be considered during the development of the processing algorithms to obtain a sufficiently general method. On the other hand, the same neural network can be trained on a larger dataset to make it work in more general conditions.

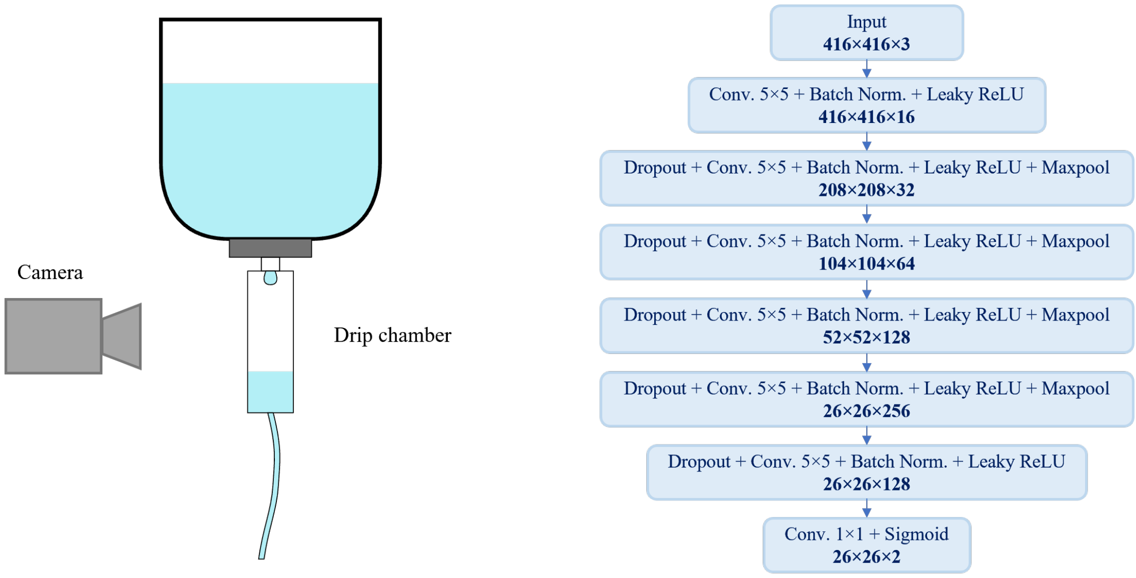

(a) (b)

Figure A.4: (a) Representation of the proposed IV drip infusion monitoring system. (b) Architecture of the neural network used for drops detection and counting.

A.3.2 Results and discussion

The results of the drop state detection are reported in **Figure A.5** (a) for the first 20 s of the five test videos, together with the drop counting results and the true values that were obtained by manually labeling the videos. As can be seen in the figure, the measured position of time instants in which the drop detaches from the dripper are very accurate. The only visible defects are some fast transitions between the two states in the second video: however, given that they last only for one frame, they were easy to filter out, resulting in a correct drop count. The final output of the proposed method is the estimate of the flow rate of the IV drip infusion kit reported in **Figure A.5** (b). The results show that the system is able to produce a very accurate estimate of the flow rate. In conclusion, the advantages of the proposed method are the following: *(i)* it does not interfere with the normal operations required for traditional IV infusion (simple installation process, no risk of contaminating the IV fluid, few interferences with the work of medical staff); *(ii)* it counts the drops virtually without error; *(iii)* it is easily usable to monitor automatically and simultaneously several different IV infusions, in different locations, provided an internet connection is available; *(iv)*it is, finally, useful to avoid unnecessary risks while monitoring contagious patients in isolations.

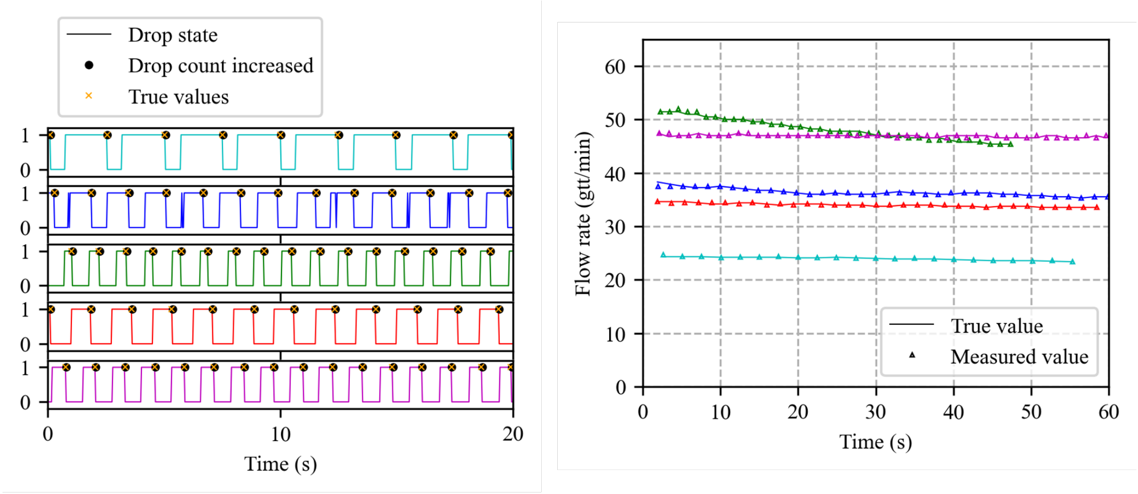

(a) (b)

Figure A.5: (a) Detected drop state versus time, and instants in which the drop count is increased, for portions of five different test videos. “True values” are the instants in which the drop detaches from the dripper, determined by human inspection of the processed videos. (b) Estimation of the flow rate of the IV drip infusion kit in the five test videos. The “true value” of the flow rate is computed by human drop counting.

A.4 Monitoring of seagrass meadows using satellite images and U-Net convolutional neural network[4]

In this Section, a deep learning-based image segmentation model for monitoring of marine seagrass meadows through satellite images is presented **[39]**. Seagrass meadows are a very important component of coastal ecosystems, but they are constantly threatened due to anthropic activities. An effective and frequent monitoring of seagrass meadows is therefore widely recognized as an urgent need for their conservation as well as to have an indicator of excessive anthropic pressure on marine ecosystems. The proposed model can perform a pixel-wise classification of the satellite image, recognizing land, seawater, and seagrass meadows. A dataset of high-resolution satellite images of regions along the Apulian coast-

---

[4] This Section is based on the paper **[39]**

line has been created and used as training dataset for the deep learning model. The classification performances of the model are then assessed using a set of test images and very promising results are obtained.

A.4.1 Composition of the satellite imagery dataset

A dataset of satellite images of limited regions along the Apulian coastline is created. The images are collected using the ArcGIS Pro software. In particular, the images are extracted from the "World Imagery" layer, that provides true-color images within 3–5 years of occurrent, typically, for most of the world. The images constituting the dataset are relative to a total of eight locations. The satellite images are manually labeled by partitioning all their pixels into segments and assigning one of the following classes to each of them: land, seawater, seagrass meadows. As an example, one satellite image (of "Penisola della Strea") and the corresponding label are presented in **Figure A.6** (a). The eight images are then fragmented into squared tiles of size 256 × 256. This is the size that the neural network for image segmentation accepts as input. A total of 152 tiles are obtained after fragmentation. Thirty-four of them are reserved for testing. The remaining 118 tiles are used for training, instead. The dataset of images reserved for training is augmented in order to increase the number of different samples used for training and hence improve the generalization properties of the neural network. The operations performed to generate the augmented dataset are the same for both the images and the labels. The following operations were performed for each image: random rotation, random horizontal and vertical shifts, random zoom, random horizontal and vertical flip. Some examples of images after the augmentation process are presented in **Figure A.6** (b).

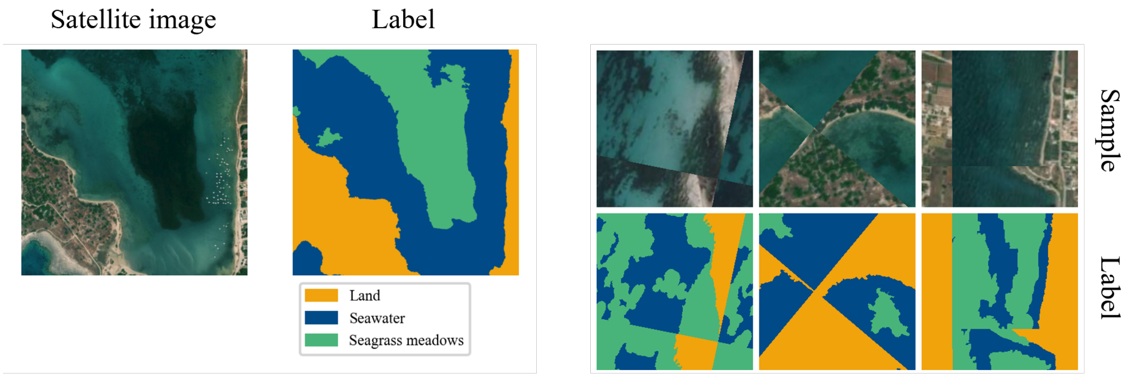

(a) (b)

Figure A.6: (a) Satellite image of "Penisola della Strea" and its segmented version. (b) Examples of augmented images and their corresponding labels.

A.4.2 Results and discussion

A modified U-Net **[87]** convolutional neural network model is trained using the dataset described in previous Section. A fraction of the augmented training dataset, corresponding to 20% of the samples, is used for validation during the training process. Intersection over Union (IoU) is the metric selected to assess the performances of the model in the segmentation task. The training process is summarized in the diagrams of **Figure A.7** (a), where the loss function and the IoU metric are plotted versus epochs, for both the training and validation datasets. As can be seen, the mean IoU is plateauing above 0.9 at the end of the training, and no significant overfitting is detectable. After the training process, the model's performances are assessed using the test dataset. In **Figure A.7** (b), one example of segmented test image is depicted. The overall classification accuracy is 92%, while the mean IoU is 0.98 for land, 0.80 for seawater, 0.83 for seagrass meadows. These results shows that the model is able to classify satellite images with good accuracy and the proposed technique can therefore be effectively used for spatiotemporal monitoring of seagrass meadows.

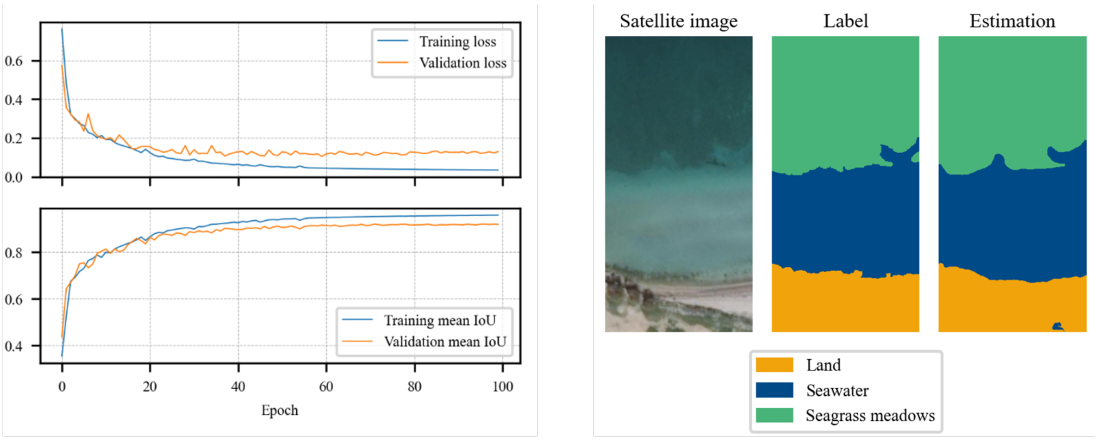

(a) (b)

Figure A.7: (a) Loss function and mean IOU variation during the training process. (b) Segmentation result obtained for the test tiles of one satellite image.

A.5 A dataset of satellite images for deep learning-based coastline measurement[5]

In this Section, a method for the automatic generation of a dataset of labelled satellite images, containing both sea and land regions, is presented **[40]**. Coastline monitoring over time is crucial to promptly detect and address environmental problems such as coastal erosion. Satellite imaging offers a great opportunity for this kind of tasks, but proper analysis tools are required to identify sea and land regions. In recent years, research has been focused on the usage of deep learning techniques for sea-land segmentation and coastline detection. For these methods, a large dataset of labelled samples is required but often not available. The automatic labelling method proposed here is based on the combination of information retrieved from publicly available coastline data and from satellite images themselves and can be used to generate a large number of sea-land segmented samples.

---

[5] This Section is based on the paper **[40]**

A.5.1 Dataset generation procedure

Sentinel-2 Level-1C images are considered for the dataset. The Sentinel-2 mission provides high-resolution satellite images with 13 spectral bands. Four bands have spatial resolution of 10 m, six bands have resolution of 20 m, and three bands have resolution of 60 m. All continental land and coastal waters up to 20 km from the shore are covered by the mission, with a revisit time of 5 days. Different data sources are taken into consideration for labelling data, with the aim of finding a dataset with high spatial resolution data and containing segments of coastline with an associated date, so that satellite images in the same date can be selected. The chose data is finally the Continually Updated Shoreline Product (CUSP) by NOAA **[88]**. This dataset contains the coastline of the USA and is continually updated. The coastline is split in short segments annotated with additional information such as the date and type (e.g., satellite or aerial) of data used for the coastline extraction and the type of coast.

Seantinel-2 images and NOAA CUSP data are therefore combined to obtain the labelled dataset, as shown in **Figure A.8**. Coastline segments are first selected from the NOAA CUSP dataset, filtering out those for which a Sentinel image is not available (e.g. they are too old). Smaller squared tiles are therefore extracted from Sentinel-2 following the coastline, as shown in **Figure A.8** (a). The two regions defined by the coastline in each tile are then labelled using also data of Sentinel-2 water bodies detection. In this step, only tiles with a good accordance between the water bodies detection and the NOAA CUSP coastline are kept, as shown in **Figure A.8** (b).

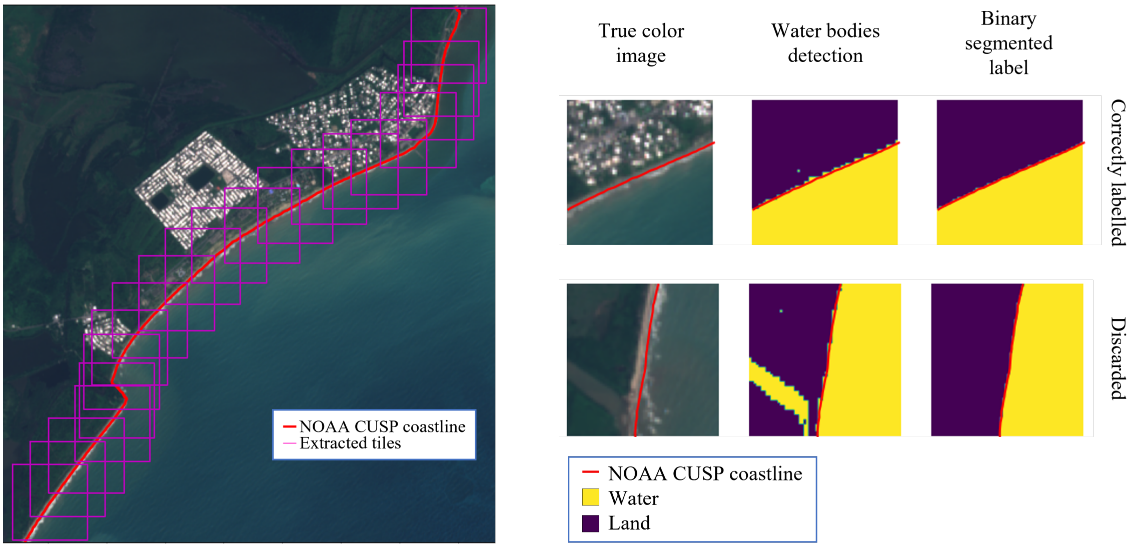

Figure A.8: (a) Extraction of tiles following the coastline. (b) Example of correctly labelled tile and discarded tile. A river or canal not included in the NOAA CUSP coastline was correctly identified by the water bodies detection.

A.5.2 Results and discussion

The dataset generation procedure described above generated 894 labelled tiles. The tiles contain all the 13 spectral bands provided by Sentinel 2 with uniformized resolution of 10 m. Even if the obtained dataset is not very large, the method proves to be effectively usable for the generation of datasets for this kind of tasks. The clear advantage of the method is that it allows reusing high-quality coastline data created by experts to label satellite images of different types (multispectral images, SAR images) and acquired from different sources. The effectiveness of the method has been here successfully demonstrated using NOAA CUSP coastline data and Sentinel-2 multispectral images, but the procedure can be replicated using other coastline data and satellite images.

Bibliography

[1] J. Rohrig, "Location of faulty places by measuring with cathode ray oscillographs," *Elektrotech z*, vol. 8, no. 2, pp. 241–242, 1931.

[2] R. F. Stevens and T. W. Stringfield, "A Transmission Line Fault Locator Using Fault-Generated Surges," *Transactions of the American Institute of Electrical Engineers*, vol. 67, no. 2, pp. 1168–1179, Jan. 1948. DOI: `10.1109/T-AIEE.1948.5059797`.

[3] F. N. Dalton, W. N. Herkelrath, D. S. Rawlins, and J. D. Rhoades, "Time-Domain Reflectometry: Simultaneous Measurement of Soil Water Content and Electrical Conductivity with a Single Probe," *Science*, vol. 224, no. 4652, pp. 989–990, Jun. 1984. DOI: `10.1126/science.224.4652.989`.

[4] C. Scientific, *TDR 100 Instruction Manual*, 2015. [Online]. Available: `https://s.campbellsci.com/%20documents/us/manuals/tdr100.pdf`.

[5] A. Cataldo, E. De Benedetto, G. Cannazza, E. Piuzzi, and N. Giaquinto, "Embedded TDR wire-like sensing elements for monitoring applications," *Measurement*, vol. 68, pp. 236–245, May 2015. DOI: `10.1016/j.measurement.2015.02.050`.

[6] C. H. Dowding and F.-C. Huang, "Early detection of rock movement with time domain reflectometry," *Journal of Geotechnical Engineering*, vol. 120, no. 8, pp. 1413–1427, 1994.

[7] S.-C. Ho, I.-H. Chen, Y.-S. Lin, J.-Y. Chen, and M.-B. Su, "Slope deformation monitoring in the Jiufenershan landslide using time domain reflectometry technology," *Landslides*, vol. 16, no. 6, pp. 1141–1151, Jun. 2019. DOI: `10.1007/s10346-019-01139-1`.

[8] Huibin Zhu, A. R. Hefner, and J. Lai, "Characterization of power electronics system interconnect parasitics using time domain reflectometry," *IEEE Transactions on Power Electronics*, vol. 14, no. 4, pp. 622–628, Jul. 1999. DOI: `10.1109/63.774198`.

[9] E. D. F. A. S. D. R. Committee, *Microelectronics failure analysis: desk reference*. 2004.

[10] C. P. Nemarich, "Time domain reflectometry liquid level sensors," *IEEE Instrumentation Measurement Magazine*, vol. 4, no. 4, pp. 40–44, Dec. 2001. DOI: `10.1109/5289.975464`.

[11] A. Cataldo, L. Tarricone, F. Attivissimo, and A. Trotta, "A TDR Method for Real-Time Monitoring of Liquids," *IEEE Transactions on Instrumentation and Measurement*, vol. 56, no. 5, pp. 1616–1625, Oct. 2007. DOI: `10.1109/TIM.2007.903596`.

[12] A. Cataldo, G. Cannazza, N. Giaquinto, A. Trotta, and G. Andria, "Microwave TDR for Real-Time Control of Intravenous Drip Infusions," *IEEE Transactions on Instrumentation and Measurement*, vol. 61, no. 7, pp. 1866–1873, Jul. 2012. DOI: `10.1109/TIM.2012.2192346`.

[13] A. Cataldo, G. Cannazza, E. D. Benedetto, and N. Giaquinto, "A New Method for Detecting Leaks in Underground Water Pipelines," *IEEE Sensors Journal*, vol. 12, no. 6, pp. 1660–1667, Jun. 2012. DOI: `10.1109/JSEN.2011.2176484`.

[14] A. Cataldo, E. De Benedetto, G. Cannazza, A. Masciullo, N. Giaquinto, G. M. D'Aucelli, N. Costantino, A. De Leo, and M. Miraglia, "Recent advances in the TDR-based leak detection system for pipeline inspection," *Measurement*, vol. 98, pp. 347–354, Feb. 2017. DOI: `10.1016/j.measurement.2016.09.017`.

[15] K. Wang, C.-P. Lin, and W.-H. Jheng, "A New TDR-Based Sensing Cable for Improving Performance of Bridge Scour Monitoring," *Sensors*, vol. 20, no. 22, p. 6665, Nov. 2020. DOI: `10.3390/s20226665`.

[16] A. Cataldo, R. Schiavoni, A. Masciullo, G. Cannazza, F. Micelli, and E. De Benedetto, “Combined Punctual and Diffused Monitoring of Concrete Structures Based on Dielectric Measurements,” *Sensors*, vol. 21, no. 14, p. 4872, Jan. 2021. DOI: `10.3390/s21144872`.

[17] Z. Zhou, T. Jiao, P. Zhao, J. Liu, and H. Xiao, “Development of a Distributed Crack Sensor Using Coaxial Cable,” *Sensors*, vol. 16, no. 8, p. 1198, Jul. 2016. DOI: `10.3390/s16081198`.

[18] J.-D. Yu, S. Y. Kim, and J.-S. Lee, “Variations in Velocity and Sensitivity of Electromagnetic Waves in Transmission Lines Configured in Model Piles with Necking Defects Containing Soils,” *Sensors*, vol. 20, no. 22, p. 6541, Nov. 2020. DOI: `10.3390/s20226541`.

[19] C. Furse, Y. C. Chung, C. Lo, and P. Pendayala, “A critical comparison of reflectometry methods for location of wiring faults,” *Smart Structures and Systems*, vol. 2, no. 1, pp. 25–46, 2006.

[20] M. B. Shreshthi, H. R. D. V, and S. S. Ahamed, “Comparison on Reflectometry Methods for Wire Fault Location,” SAE International, SAE Technical Paper 2011-01-2703, Oct. 2011. DOI: `10.4271/2011-01-2703`.

[21] Q. Shi and O. Kanoun, “Wire Fault Diagnosis in the Frequency Domain by Impedance Spectroscopy,” *IEEE Transactions on Instrumentation and Measurement*, vol. 64, no. 8, pp. 2179–2187, Aug. 2015. DOI: `10.1109/TIM.2014.2386918`.

[22] Y.-J. Shin, E. Powers, T.-S. Choe, C.-Y. Hong, E.-S. Song, J.-G. Yook, and J. Park, “Application of Time-Frequency Domain Reflectometry for Detection and Localization of a Fault on a Coaxial Cable,” *IEEE Transactions on Instrumentation and Measurement*, vol. 54, no. 6, pp. 2493–2500, Dec. 2005. DOI: `10.1109/TIM.2005.858115`.

[23] V. Taylor and M. Faulkner, “Line monitoring and fault location using spread spectrum on power line carrier,” *Transmission and Distribution IEE Proceedings - Generation*, vol. 143, no. 5, pp. 427–434, Sep. 1996. DOI: `10.1049/ip-gtd:19960189`.

[24] J. Reis, A. L. S. Castro, J. C. W. A. Costa, J. R. I. Riu, and K. Ericson, "Sequence and spread spectrum time domain reflectometry for transmission line analysis," in *Broadband Access Communication Technologies II*, vol. 6776, Sep. 2007, p. 67760L. DOI: `10.1117/12.735873`.

[25] P. Smith, C. Furse, and J. Gunther, "Analysis of spread spectrum time domain reflectometry for wire fault location," *IEEE Sensors Journal*, vol. 5, no. 6, pp. 1469–1478, Dec. 2005. DOI: `10.1109/JSEN.2005.858964`.

[26] J. Lundstedt and S. He, "A time-domain optimization technique for the simultaneous reconstruction of the characteristic impedance, resistance and conductance of a transmission line," *Journal of Electromagnetic Waves and Applications*, vol. 10, no. 4, pp. 581–601, Jan. 1996. DOI: `10.1163/156939396X01143`.

[27] M. Norgren and S. He, "An optimization approach to the frequency-domain inverse problem for a nonuniform LCRG transmission line," *IEEE Transactions on Microwave Theory and Techniques*, vol. 44, no. 8, pp. 1503–1507, Aug. 1996. DOI: `10.1109/22.536038`.

[28] S. Schlaeger, "A fast TDR-inversion technique for the reconstruction of spatial soil moisture content," *Hydrology and Earth System Sciences*, p. 12, 2005.

[29] A. Scheuermann, C. Huebner, S. Schlaeger, N. Wagner, R. Becker, and A. Bieberstein, "Spatial time domain reflectometry and its application for the measurement of water content distributions along flat ribbon cables in a full-scale levee model: SPATIAL TIME DOMAIN REFLECTOMETRY," *Water Resources Research*, vol. 45, no. 4, Apr. 2009. DOI: `10.1029/2008WR007073`.

[30] R. Greco, "Soil water content inverse profiling from single TDR waveforms," *Journal of Hydrology*, vol. 317, no. 3-4, pp. 325–339, Feb. 2006. DOI: `10.1016/j.jhydrol.2005.05.024`.

[31] A. Scheuermann, L. Yermán, T. Bittner, M. L. Serna, S. Zárate, M. Bajodek, and T. Bore, "Design of Two Large Coaxial Cells for Studying Physical Process Using Spatial TDR," in *2018 12th International Conference on Electromagnetic Wave Interaction with Water and Moist Substances (ISEMA)*, Jun. 2018, pp. 1–3. DOI: `10.1109/ISEMA.2018.8442318`.

[32] G. Yan, T. Bore, Z. Li, S. Schlaeger, A. Scheuermann, and L. Li, "Application of Spatial Time Domain Reflectometry for Investigating Moisture Content Dynamics in Unsaturated Loamy Sand for Gravitational Drainage," *Applied Sciences*, vol. 11, no. 7, p. 2994, Mar. 2021. DOI: `10.3390/app11072994`.

[33] N. Giaquinto, **M. Scarpetta**, and M. Spadavecchia, "Algorithms for Locating and Characterizing Cable Faults via Stepped-Frequency Waveform Reflectometry," *IEEE Transactions on Instrumentation and Measurement*, vol. 69, no. 9, pp. 7271–7280, Sep. 2020. DOI: `10.1109/TIM.2020.2974110`.

[34] N. Giaquinto, **M. Scarpetta**, and M. Spadavecchia, "Separation of Overlapping Reflected Signals in Stepped-Frequency Waveform Reflectometry," in *2020 IEEE International Instrumentation and Measurement Technology Conference (I2MTC)*, May 2020, pp. 1–6. DOI: `10.1109/I2MTC43012.2020.9128537`.

[35] **M. Scarpetta**, M. Spadavecchia, G. Andria, M. A. Ragolia, and N. Giaquinto, "Analysis of TDR Signals with Convolutional Neural Networks," in *2021 IEEE International Instrumentation and Measurement Technology Conference (I2MTC)*, May 2021, pp. 1–6. DOI: `10.1109/I2MTC50364.2021.9460009`.

[36] **M. Scarpetta**, M. Spadavecchia, F. Adamo, M. A. Ragolia, and N. Giaquinto, "Detection and Characterization of Multiple Discontinuities in Cables with Time-Domain Reflectometry and Convolutional Neural Networks," *Sensors*, vol. 21, no. 23, p. 8032, Jan. 2021. DOI: `10.3390/s21238032`.

[37] N. Giaquinto, **M. Scarpetta**, M. A. Ragolia, and P. Pappalardi, "Real-time drip infusion monitoring through a computer vision system," in *2020 IEEE International Symposium on Medical Measurements and Applications (MeMeA)*, Jun. 2020, pp. 1–5. DOI: `10.1109/MeMeA49120.2020.9137359`.

[38] N. Giaquinto, **M. Scarpetta**, M. Spadavecchia, and G. Andria, "Deep Learning-Based Computer Vision for Real-Time Intravenous Drip Infusion Monitoring," *IEEE Sensors Journal*, vol. 21, no. 13, pp. 14 148–14 154, Jul. 2021. DOI: `10.1109/JSEN.2020.3039009`.

[39] **M. Scarpetta**, P. Affuso, M. De Virgilio, M. Spadavecchia, G. Andria, and N. Giaquinto, "Monitoring of Seagrass Meadows Using Satellite Images and

U-Net Convolutional Neural Network," in *2022 IEEE International Instrumentation and Measurement Technology Conference (I2MTC)*, May 2022, pp. 1–6. DOI: `10.1109/I2MTC48687.2022.9806535`.

[40] **M. Scarpetta**, M. Spadavecchia, V. I. D'Alessandro, L. De Palma, and N. Giaquinto, "A new dataset of satellite images for deep learning-based coastline measurement," in *2022 IEEE International Conference on Metrology for eXtended Reality, Artificial Intelligence, and Neural Engineering*, Oct. 2022, pp. 1–6.

[41] C. Lee, G. Kwon, and Y. Shin, "Condition Assessment of I&C Cables in Nuclear Power Plants via Stepped-Frequency Waveform Reflectometry," *IEEE Transactions on Instrumentation and Measurement*, vol. 68, no. 1, pp. 215–224, Jan. 2019. DOI: `10.1109/TIM.2018.2834179`.

[42] R. Pintelon and L. Van Biesen, "Identification of transfer functions with time delay and its application to cable fault location," *IEEE Transactions on Instrumentation and Measurement*, vol. 39, no. 3, pp. 479–484, Jun. 1990. DOI: `10.1109/19.106276`.

[43] G. M. D'Aucelli, N. Giaquinto, and G. Andria, "LineLab-A Transmission Line Simulator for Distributed Sensing Systems: Open-Source MATLAB Code for Simulating Real-World Transmission Lines," *IEEE Antennas and Propagation Magazine*, vol. 60, no. 4, pp. 22–30, Aug. 2018. DOI: `10.1109/MAP.2018.2839908`.

[44] N. Giaquinto, A. Cataldo, G. M. D'Aucelli, E. De Benedetto, and G. Cannazza, "Water Detection Using Bi-Wires as Sensing Elements: Comparison Between Capacimetry-Based and Time-of-Flight-Based Techniques," *IEEE Sensors Journal*, vol. 16, no. 11, pp. 4309–4317, Jun. 2016. DOI: `10.1109/JSEN.2016.2540299`.

[45] A. Cataldo, E. De Benedetto, G. Cannazza, E. Piuzzi, and E. Pittella, "TDR-Based Measurements of Water Content in Construction Materials for In-the-Field Use and Calibration," *IEEE Transactions on Instrumentation and Measurement*, vol. 67, no. 5, pp. 1230–1237, May 2018. DOI: `10.1109/TIM.2017.2770778`.

[46] N. Giaquinto, G. M. D'Aucelli, E. De Benedetto, G. Cannazza, A. Cataldo, E. Piuzzi, and A. Masciullo, "Criteria for Automated Estimation of Time of Flight in TDR Analysis," *IEEE Transactions on Instrumentation and Measurement*, vol. 65, no. 5, pp. 1215–1224, May 2016. DOI: `10.1109/TIM.2015.2495721`.

[47] G. Andria, F. Attivissimo, A. Di Nisio, A. Trotta, S. M. Camporeale, and P. Pappalardi, "Design of a microwave sensor for measurement of water in fuel contamination," *Measurement*, vol. 136, pp. 74–81, Mar. 2019. DOI: `10.1016/j.measurement.2018.12.076`.

[48] A. Cataldo, E. De Benedetto, G. Cannazza, G. Monti, and E. Piuzzi, "TDR-based monitoring of rising damp through the embedding of wire-like sensing elements in building structures," *Measurement*, vol. 98, pp. 355–360, Feb. 2017. DOI: `10.1016/j.measurement.2016.10.044`.

[49] F. M. Tesche, "A Simple Model for the Line Parameters of a Lossy Coaxial Cable Filled With a Nondispersive Dielectric," *IEEE Transactions on Electromagnetic Compatibility*, vol. 49, no. 1, pp. 12–17, Feb. 2007. DOI: `10.1109/TEMC.2006.888185`.

[50] D. M. J. Cowell and S. Freear, "Separation of overlapping linear frequency modulated (LFM) signals using the fractional fourier transform," *IEEE Transactions on Ultrasonics, Ferroelectrics, and Frequency Control*, vol. 57, no. 10, pp. 2324–2333, Oct. 2010. DOI: `10.1109/TUFFC.2010.1693`.

[51] A. Akhavan, A. Mahloojifar, and S. Hashemi-Berenjabad, "Detection and separation of chirp echoes in coded excitation ultrasound imaging using fractional Fourier transform," in *2011 18th Iranian Conference of Biomedical Engineering (ICBME)*, Dec. 2011, pp. 185–190. DOI: `10.1109/ICBME.2011.6168552`.

[52] F. Adamo, F. Attivissimo, A. Di Nisio, M. Savino, and M. Spadavecchia, "A spectral estimation method for nonstationary signals analysis with application to power systems," *Measurement*, vol. 73, pp. 247–261, Sep. 2015. DOI: `10.1016/j.measurement.2015.04.023`.

[53] G.-M. Zhang, C.-Z. Zhang, and D. M. Harvey, "Sparse signal representation and its applications in ultrasonic NDE," *Ultrasonics*, vol. 52, no. 3, pp. 351–363, Mar. 2012. DOI: `10.1016/j.ultras.2011.10.001`.

[54] L. Angrisani, F. Bonavolontà, G. Cavallo, A. Liccardo, and R. Schiano Lo Moriello, "On the measurement uncertainties of THz imaging systems based on compressive sampling," *Measurement*, vol. 116, pp. 83–95, Feb. 2018. DOI: `10.1016/j.measurement.2017.10.030`.

[55] L. Angrisani, F. Bonavolontà, A. Liccardo, and R. Schiano Lo Moriello, "Identification and classification of transformers current transients through Huang Hilbert Transform," *Measurement*, vol. 125, pp. 123–132, Sep. 2018. DOI: `10.1016/j.measurement.2018.04.080`.

[56] E. Mor, A. Azoulay, and M. Aladjem, "A matching pursuit method for approximating overlapping ultrasonic echoes," *IEEE Transactions on Ultrasonics, Ferroelectrics, and Frequency Control*, vol. 57, no. 9, pp. 1996–2004, Sep. 2010. DOI: `10.1109/TUFFC.2010.1647`.

[57] E. Mor, M. Aladjem, and A. Azoulay, "Cluster-enhanced sparse approximation of overlapping ultrasonic echoes," *IEEE Transactions on Ultrasonics, Ferroelectrics, and Frequency Control*, vol. 62, no. 2, pp. 373–386, Feb. 2015. DOI: `10.1109/TUFFC.2014.006769`.

[58] J. P. Fortineau, F. Vander Meulen, J. Fortineau, and G. Feuillard, "Efficient algorithm for discrimination of overlapping ultrasonic echoes," *Ultrasonics*, vol. 73, pp. 253–261, Jan. 2017. DOI: `10.1016/j.ultras.2016.09.010`.

[59] J. E. Carlson, A. K. Ovacikli, and P. Pääjärvi, "Material impulse response estimation from overlapping ultrasound echoes using a compressed sensing technique," in *2017 IEEE International Ultrasonics Symposium (IUS)*, Sep. 2017, pp. 1–4. DOI: `10.1109/ULTSYM.2017.8091788`.

[60] G. Shi, C. Chen, J. Lin, X. Xie, and X. Chen, "Narrowband Ultrasonic Detection with High Range Resolution: Separating Echoes via Compressed Sensing and Singular Value Decomposition," *IEEE Transactions on Ultrason-*

ics, Ferroelectrics, and Frequency Control, vol. 59, no. 10, pp. 2237–2253, Oct. 2012. DOI: `10.1109/TUFFC.2012.2449`.

[61] M. Li, X. Li, C. Gao, and Y. Song, "Acoustic microscopy signal processing method for detecting near-surface defects in metal materials," *NDT & E International*, vol. 103, pp. 130–144, Apr. 2019. DOI: `10.1016/j.ndteint.2019.02.005`.

[62] J. Bustillo, H. Achdjian, A. Arciniegas, and L. Blanc, "Simultaneous determination of wave velocity and thickness on overlapped signals using Forward Backward algorithm," *NDT & E International*, vol. 86, pp. 100–105, Mar. 2017. DOI: `10.1016/j.ndteint.2016.12.001`.

[63] S. Chen, X. Dong, G. Xing, Z. Peng, W. Zhang, and G. Meng, "Separation of Overlapped Non-Stationary Signals by Ridge Path Regrouping and Intrinsic Chirp Component Decomposition," *IEEE Sensors Journal*, vol. 17, no. 18, pp. 5994–6005, Sep. 2017. DOI: `10.1109/JSEN.2017.2737467`.

[64] C.-K. Lee and Y.-J. Shin, "Detection and Assessment of I&C Cable Faults Using Time–Frequency R-CNN-Based Reflectometry," *IEEE Transactions on Industrial Electronics*, vol. 68, no. 2, pp. 1581–1590, Feb. 2021. DOI: `10.1109/TIE.2020.2970677`.

[65] H. Lim, G.-Y. Kwon, and Y.-J. Shin, "Fault Detection and Localization of Shielded Cable via Optimal Detection of Time–Frequency Domain Reflectometry," *IEEE Transactions on Instrumentation and Measurement*, pp. 1–1, 2021. DOI: `10.1109/TIM.2021.3092514`.

[66] O. Osman, S. Sallem, L. Sommervogel, M. O. Carrion, P. Bonnet, and F. Paladian, "Distributed Reflectometry for Soft Fault Identification in Wired Networks Using Neural Network and Genetic Algorithm," *IEEE Sensors Journal*, vol. 20, no. 9, pp. 4850–4858, May 2020. DOI: `10.1109/JSEN.2020.2965287`.

[67] C.-K. Lee and S. J. Chang, "Fault Detection in Multi-Core C&I Cable via Machine Learning Based Time-Frequency Domain Reflectometry," *Applied Sciences*, vol. 10, no. 1, p. 158, Jan. 2020. DOI: `10.3390/app10010158`.

[68] T. A. Alvarenga, A. S. Cerqueira, L. M. A. Filho, R. A. Nobrega, L. M. Honorio, and H. Veloso, “Identification and Localization of Track Circuit False Occupancy Failures Based on Frequency Domain Reflectometry,” *Sensors*, vol. 20, no. 24, p. 7259, Jan. 2020. DOI: `10.3390/s20247259`.

[69] G.-Y. Kwon, C.-K. Lee, and Y.-J. Shin, “Diagnosis of Shielded Cable Faults via Regression-Based Reflectometry,” *IEEE Transactions on Industrial Electronics*, vol. 66, no. 3, pp. 2122–2131, Mar. 2019. DOI: `10.1109/TIE.2018.2840529`.

[70] W. Liu, D. Anguelov, D. Erhan, C. Szegedy, S. Reed, C.-Y. Fu, and A. C. Berg, “SSD: Single Shot MultiBox Detector,” in *Computer Vision – ECCV 2016*, B. Leibe, J. Matas, N. Sebe, and M. Welling, Eds., ser. Lecture Notes in Computer Science, 2016, pp. 21–37. DOI: `10.1007/978-3-319-46448-0_2`.

[71] J. Redmon, S. Divvala, R. Girshick, and A. Farhadi, “You Only Look Once: Unified, Real-Time Object Detection,” in *2016 IEEE Conference on Computer Vision and Pattern Recognition (CVPR)*, Jun. 2016, pp. 779–788. DOI: `10.1109/CVPR.2016.91`.

[72] D. P. Kingma and J. Ba, “Adam: A Method for Stochastic Optimization,” *arXiv:1412.6980 [cs]*, Dec. 2014.

[73] **M. Scarpetta**, M. Spadavecchia, F. Adamo, M. A. Ragolia, N. Giaquinto, and 2021., *Supplementary Material for the Paper "Detection and Characterization of Multiple Discontinuities in Cables with Time Domain Reflectometry and Convolutional Neural Networks"; DOI: 10.5281/zenodo.5720438;* 2021. [Online]. Available: `https://zenodo.org/record/5720438`.

[74] **M. Scarpetta**, A. Cataldo, M. Spadavecchia, E. Piuzzi, A. Masciullo, and N. Giaquinto, “Accurate Detection and Localization of Water Pipe Leaks Through Model-Based TDR Inversion,” *Sensors, under review*, 2022.

[75] EurEau, *Europe’s Water in Figures – An overview of the European drinking water and waste water sectors*, 2021.

[76] European Environment Agency, “Water resources across Europe – confronting water stress: An updated assessment,” *EEA Report*, vol. 12, 2021.

[77] EU, *Directive (EU) 2020/2184 of the European Parliament and of the Council of 16 December 2020 on the quality of water intended for human consumption*, 2020. [Online]. Available: `https://eur-lex.europa.eu/eli/dir/2020/2184/oj`.

[78] Z. Liu and Y. Kleiner, "State of the art review of inspection technologies for condition assessment of water pipes," *Measurement*, vol. 46, no. 1, pp. 1–15, Jan. 2013. DOI: `10.1016/j.measurement.2012.05.032`.

[79] Y. Yu, A. Safari, X. Niu, B. Drinkwater, and K. V. Horoshenkov, "Acoustic and ultrasonic techniques for defect detection and condition monitoring in water and sewerage pipes: A review," *Applied Acoustics*, vol. 183, p. 108 282, Dec. 2021. DOI: `10.1016/j.apacoust.2021.108282`.

[80] A. Cataldo, G. Cannazza, E. D. Benedetto, and N. Giaquinto, "A TDR-based system for the localization of leaks in newly installed, underground pipes made of any material," *Measurement Science and Technology*, vol. 23, no. 10, p. 105 010, Sep. 2012. DOI: `10.1088/0957-0233/23/10/105010`.

[81] A. Cataldo, G. Cannazza, E. D. Benedetto, and a. N. Giaquinto, "Experimental Validation of a TDR-Based System for Measuring Leak Distances in Buried Metal Pipes," *Progress In Electromagnetics Research*, vol. 132, pp. 71–90, 2012. DOI: `10.2528/PIER12081402`.

[82] M. Schumer and K. Steiglitz, "Adaptive step size random search," *IEEE Transactions on Automatic Control*, vol. 13, no. 3, pp. 270–276, Jun. 1968. DOI: `10.1109/TAC.1968.1098903`.

[83] **M. Scarpetta**, M. Spadavecchia, G. Andria, M. A. Ragolia, and N. Giaquinto, "Accurate simultaneous measurement of heartbeat and respiratory intervals using a smartphone," *Journal of Instrumentation*, vol. 17, no. 07, P07020, Jul. 2022. DOI: `10.1088/1748-0221/17/07/P07020`.

[84] **M. Scarpetta**, M. Spadavecchia, G. Andria, M. A. Ragolia, and N. Giaquinto, "Simultaneous Measurement of Heartbeat Intervals and Respiratory Signal using a Smartphone," in *2021 IEEE International Symposium on Medical*

Measurements and Applications (MeMeA), Jun. 2021, pp. 1–5. DOI: `10.1109/MeMeA52024.2021.9478711`.

[85] O. T. Inan, P. Migeotte, K. Park, M. Etemadi, K. Tavakolian, R. Casanella, J. Zanetti, J. Tank, I. Funtova, G. K. Prisk, and M. D. Rienzo, "Ballistocardiography and Seismocardiography: A Review of Recent Advances," *IEEE Journal of Biomedical and Health Informatics*, vol. 19, no. 4, pp. 1414–1427, Jul. 2015. DOI: `10.1109/JBHI.2014.2361732`.

[86] A. Di Nisio, N. Giaquinto, A. M. L. Lanzolla, M. A. Ragolia, **M. Scarpetta**, and S. Carrara, "Platinum Nanostructured Needle-Shaped Sensors for Ion-Detection in Biomedical Applications," *IEEE Sensors Journal*, 2022. DOI: `10.1109/JSEN.2022.3216682`.

[87] O. Ronneberger, P. Fischer, and T. Brox, "U-Net: Convolutional Networks for Biomedical Image Segmentation," in *Medical Image Computing and Computer-Assisted Intervention – MICCAI 2015*, N. Navab, J. Hornegger, W. M. Wells, and A. F. Frangi, Eds., ser. Lecture Notes in Computer Science, 2015, pp. 234–241. DOI: `10.1007/978-3-319-24574-4_28`.

[88] *NOAA Shoreline Website*. [Online]. Available: `https://shoreline.noaa.gov/data/datasheets/cusp.html` (visited on 06/29/2022).